Design and Development of Higher Temperature Membranes for PEM Fuel Cells

By
TONY M. THAMPAN

A Dissertation
Submitted to the Faculty
Of the
WORCESTER POLYTECHNIC INSTITUTE
In partial fulfillment of the requirements for the
Degree of Doctor of Philosophy
Chemical Engineering
By

MAY 2003

APPROVED:

PROF. RAVINDRA DATTA, MAJOR ADVISOR
HEAD OF DEPARTMENT

PROF. SATYA S. SHIVKUMAR, COMMITTEE MEMBER

PROF. ROBERT W. THOMPSON, COMMITTEE MEMBER

Abstract

Proton-Exchange Membrane (PEM) fuel cells are extremely attractive for replacing internal combustion engines in the next generation of automobiles. However, two major technical challenges remain to be resolved before PEM fuel cells become commercially successful. The first issue is that CO, produced in trace amounts in fuel reformer, severely limits the performance of the conventional platinum-based PEM fuel cell. A possible solution to the CO poisoning is higher temperature operation, as the CO adsorption and oxidation overpotential decrease considerably with increasing temperature. However, the process temperature is limited in atmospheric fuel cells because water is critical for high conductivity in the standard PEM. An increase in operating pressure allows higher temperature operation, although at the expense of parasitic power for the compressor. Further the conventional PEM, Nafion®, is limited to 120°C due to it's low glass transition temperature.

Thus, the design of higher temperature PEMs with stable performance under low relative humidity (RH) conditions is considered based on a proton transport model for the PEM and a fuel cell model that have been developed. These predictive models capture the significant aspects of the experimental results with a minimum number of fitted parameters and provides insight into the design of higher temperature PEMs operating at low RH.

The design of an efficacious high temperature, low RH, PEM was based on enhancing the acidity and water sorption properties of a conventional PEM by impregnating it with a solid superacid. A systematic investigation of the composite Nafion®/inorganic PEMs comprising experiments involving water uptake, ion-exchange capacity (IEC), conductivity and fuel cell polarization is presented in the work. The most promising composite is the nano-structured ZrO_2/Nafion® PEM which exhibits an increase in the IEC, a 40% increase in water sorbed and a resulting 24% conductivity enhancement vs. unmodified Nafion® 112 at 120°C and at RH < 40%.

Acknowledgements

I would like to thank Professor Ravindra Datta for the opportunity to attain a Ph.D. under his guidance. His personal contribution towards my professional development cannot be overstated. His eagerness to publish and present our work and the associated investment in my career has been marvelous. The most impressive parts of my thesis are a direct result of his unfailing support and encouragement.

I would also like to thank my committee for their time and suggestions in developing my thesis. Their insightful suggestions have significantly improved the quality of this work.

I would also like to thank the dedicated staff of the WPI Chemical Engineering department including Jack Ferraro, Douglas White, Joe Kaupu and Sandra Natale, who have helped make my stay in the department a thoroughly enjoyable experience. I would also to express my thanks towards the entire staff at WPI, who have make WPI the wonderful place it is.

I would also like to express my sincere thanks to the many friends I have made during my stay at WPI, including co-workers and other students. Their good humor in pushing towards the PhD has made the experience all the more enjoyable.

I would also like to thank my friends and family. I will simply say that words cannot express my appreciation for the understanding and sacrifice that you have all made that has helped me come this far. I must thank the entire Worcester County Church of Christ who have been my home away from home. I must especially thank my fiancé, Rachel Terpsma for her patience, understanding and support. I would also like to my parents who have financially, emotionally and unconditionally supported my education and me. I hope I can do as much for my children as they have done for us. Also thank you to my brother, Ronnie, and sister, Sarah, who have always provided a kind ear for me to vent. I have finally finished!

Finally, I must thank Him for allowing me the chance of a lifetime and enabling me to do the little that I was able to do.

TABLE OF CONTENTS

III PEM FUEL CELL AS A MEMBRANE REACTOR

IV RATIONAL DESIGN OF HIGHER TEMPERATURE COMPOSITE PROTON EXCHANGE MEMBRANES

V CONCLUSIONS AND RECOMMENDATIONS

LIST OF FIGURES

FIGURE **PAGE**

LIST OF TABLES

LIST OF SYMBOLS

a_i	activity of species i
a_w	activity, or relative humidity RH, of water, = p_w / p_w^o
a_α	mean pore radius of porous layer α, nm
A	geometric area of PEM in fuel cell
A_2	surface area occupied by adsorbate molecule, nm^2
A_ρ	pre-exponential factor of reaction ρ
$A_i^{z_i}$	species i with charge z_i
$B_{0\alpha}$	d'Arcy permeability of layer α, cm^2
C	BET constant
$c_{\mathrm{HA},0}$	concentration of membrane acid groups, = $1 / \lambda \bar{V}_2$, mol/cm^3 pore solution
c	total concentration of mixture, = $\Sigma_i c_i$, mol/cm^3, total concentration of liquid mixture, mol/cm^3 pore solution
c_i	concentration of species i, mol/cm^3 pore solution
$c_{i\alpha}$	concentration of species i in layer α, mol/cm^3
c_{iS}	concentration of species i in region S
c_{iT}	concentration of species i in region T
d_M	catalyst metal microcrystallite diameter, nm
$D_{i\alpha}^e$	effective diffusion coefficient of species i in layer α, cm^2/s
D_{iL}	liquid-phase diffusion coefficient of species i, cm^2/s

D_{ij}	mutual diffusion coefficient for species *i* and *j*, cm^2/s
D_{ij}^{e}	effective mutual diffusion coefficient of species *i* and *j*, $=K_1 D_{ij}$, cm^2/s
D_{iG}^{e}	effective gas-phase diffusion coefficient of species *i* in the gas-diffusion backing, cm^2/s
D_{ij}^{eo}	pressure independent effective binary diffusion coefficient of species *i* and *j*, = pD_{ij}^{e}, bar-cm^2/s
D_{iK}^{e}	effective Knudsen diffusion coefficient of species *i*, cm^2/s
D_{iM}^{e}	effective diffusion coefficient for interaction of species *i* and matrix *M*, $=K_0 D_{iM}$, cm^2/s
EW	membrane equivalent weight, g dry polymer/mol –SO$_3$H groups
E_{A,Φ_0}	effective activation energy of $i_{A,0}$ or $\vec{k}^{*}_{A,\Phi_0}$
E_{μ}	activation energy for viscosity, kJ/mol
F	Faraday's constant, 96,487 C/eq
F_T	volumetric flow rate in anode
$[H^e]$	matrix with elements H_{ij}^{e}
H_{ij}^{e}	effective frictional coefficient defined by Eq. (15), s/cm^2
HA	acid group (e.g., –SO$_3$H) in membrane
$\boldsymbol{i}$	fuel cell current density, A/cm^2 of geometric electrode area
i, j	species i, j
i_A	anodic current density, A/cm^2 of geometric electrode area
$i_{A,L}$	anodic limiting current density, A/cm^2 of geometric electrode area

i_C	cathodic current density, A/cm^2 of geometric electrode area
$i_{C,L}$	cathodic limiting current density, A/cm^2 of geometric electrode area
i_0	exchange current density, A/cm^2 of geometric electrode area
$i_{A,0}$	anodic exchange current density, A/cm^2 of geometric electrode area
$i_{C,0}$	cathodic exchange current density, A/cm^2 of geometric electrode area
i^*	current density, A/cm^2 of metal catalyst surface
i^*_0	exchange current density, A/cm^2 of metal catalyst surface
$i^*_{A,0}$	anodic exchange current density, A/cm^2 of metal catalyst surface
$i^*_{C,0}$	cathodic exchange current density, A/cm^2 of metal catalyst surface
K_0	dusty-fluid model structural constant for matrix diffusion coefficient
K_1	dusty-fluid model structural constant for mutual diffusion coefficient
K_{HA}	equilibrium constant for acid dissociation
$K_{\mathrm{BH}_2^+}$	equilibrium constant for solvent protonation
K_{A}	equilibrium constant for proton solvation, $= K_{\mathrm{HA}} / K_{\mathrm{BH}_2^+}$
k_B	Boltzmann constant
$\vec{k}^*_\rho$	rate constant of forward elementary reaction ρ, s^{-1}
$\overleftarrow{k}^*_\rho$	rate constant of reverse elementary reaction ρ, s^{-1}
$\vec{k}^*_{\rho,\Phi_0}$	rate constant of forward elementary reaction ρ at equilibrium electrode potential Φ_0, s^{-1}
k^*_A	effective rate constant of overall anode reaction

$\vec{k}^{*}_{A,\Phi_0}$	rate constant of anode reaction at equilibrium electrode potential Φ_0
k^{*}_{C}	effective rate constant of overall cathode reaction
$\vec{k}^{*}_{C,\Phi_0}$	rate constant of anode reaction at equilibrium electrode potential Φ_0
$K_{\mathrm{A},C}$	equilibrium constant for proton solvation in terms of concentrations
K_{ρ}	equilibrium constant of reaction ρ
K_{ρ,Φ_0}	equilibrium constant of reaction ρ at equilibrium electrode potential Φ_0
$K_{0\alpha}$	dusty-gas constant of layer α for effective Knudsen diffusion coefficient, cm
$K_{1\alpha}$	dusty-gas constant of layer α for effective binary diffusion coefficient
L_{α}	thickness of layer α
m_I	ionomer loading in catalyst layer, g metal/cm^2 geometric electrode area
m_M	catalyst loading, g metal/cm^2 geometric electrode area
n	total number of species
n_w	total number of water layers sorbed on the pore surface
n_{ρ}	number of electrons participating in reaction ρ
N_A	Avogadro’s number, 6.02205 x 10^{23} molecules/mol
N_i	flux of species i, mol/cm^2 geometric electrode area
p	total pressure, bar
p_i	partial pressure of species i, bar
p_S	total pressure in cathode chamber, bar
p_T	total pressure in anode chamber, bar

p	pressure, N/cm^2
p_i	partial pressure of species i, N/cm^2
p_i^o	vapor pressure of water, bar
P	power density, W/cm^2 geometric electrode area
P_{ia}	permeability of layer α for species i, $= D_{i\alpha}\kappa_{i\alpha}/L_\alpha$, cm/s
Q_1	heat of adsorption of first layer, J/mol
Q_L	heat of adsorption of subsequent layers, J/mol
q	Bruggeman or critical exponent = 1.5
q_α	liquid loading of layer α, cm^3 liquid/cm^3 void volume
q_I	ionomer loading in catalyst layer, cm^3 ionomer/cm^3 void volume
r_i	net rate of reversible reaction i, $=\vec{r}_i - \overleftarrow{r}_i$, mol/$cm^3$ catalyst particles.s
$\vec{r}_{i0}$	rate of forward reaction under open circuit conditions, mol/cm^3 catalyst particles.s
r_i^*	net rate of reversible reaction i, $=\vec{r}_i^{\,*} - \overleftarrow{r}_i^{\,*}$, mol/cm^2 metal catalyst area.s
r_A^*	net rate of anodic reaction, mol/cm^2 metal catalyst area.s
r_C^*	net rate of cathodic reaction, mol/cm^2 metal catalyst area.s
$r_{\rho 0}$	reaction rate at open circuit
R	universal gas constant, 8.3143 J/mol.K
R_I	interfacial resistance, $\Omega\ cm^2$
s	surface coordination number
S	catalyst site, specific pore surface area, m^2/cm^3

S_M	specific surface area of metal crystallites, cm^2/g metal
S_S	specific surface area of carbon support particles, cm^2/g carbon
T	temperature, K
T_0	reference temperature, K
$\boldsymbol{v}$	mass-average convective velocity of fluid, cm/s
$\boldsymbol{v}_\mathrm{i}$	absolute velocity of species *i*, cm/s
$\boldsymbol{v}_i^D$	diffusional velocity of species *i* with respect to the mixture mass-average velocity
V	fuel cell potential, = $\phi_{MC} - \phi_{MA}$, V
V_0	open circuit potential, = $\Phi_{0,C} - \Phi_{0,A}$, V
$\overline{V}_i$	partial molar volume of species *i*, cm^3/mol
W	expression given by Eq. 6, dimensionless
x_i	mole fraction of species *i*
z	coordinate
z_i	charge number of species *i*

Greek letters

α	degree of acid group dissociation
$\vec{\alpha}_A$	effective transfer coefficient of overall anode reaction = 1/2
$\vec{\alpha}_C$	effective transfer coefficient of overall cathode reaction = 1
β_ρ	symmetry factor of elementary reaction $\rho = 1/2$
ΔH^o	enthalpy change for proton solvation, kJ/mol

$\Delta\vec{H}^{\pm o}_{iT,\Phi=0}$	standard enthalpy change of activation for forward elementary reaction ρ
κ^{e}_{ij}	elements of inverse matrix $[H^e]^{-1}$, effective Onsager diffusion coefficients, cm^2/s
γ_i	activity coefficient of species *i*
Γ	ratio of the diffusion coefficient to that at infinite dilution, $= D_{12} / D^0_{12}$
δ	ratio of mutual to matrix effective diffusion coefficients, $= D^e_{12} / D^e_{1M}$
δ_{ij}	Kronecker delta function
ε	volume fraction of water in hydrated membrane, or wet porosity
ε_0	percolation threshold volume fraction of water in hydrated membrane
ζ_{ij}	friction coefficient for interaction between species *i* and *j*, $(\text{J.s/cm}^5)(\text{cm}^3/\text{mol})^2$
ζ_{iM}	friction coefficient for interaction between species *i* and matrix *M*, $(\text{J.s/cm}^5)(\text{cm}^3/\text{mol})^2$
λ_0	water loading at percolation threshold, number of water molecules per $–SO_3H$ group
$\lambda^{\text{liq}}_{\text{sat}}$	water loading at saturation in equilibrium with liquid water, number of water molecules per $–SO_3H$ group
$\lambda^{\text{vap}}_{\text{sat}}$	water loading at saturation in equilibrium with saturated water vapor, number of water molecules per $–SO_3H$ group
ν	flux ratio, $= -\boldsymbol{N}_2/\boldsymbol{N}_1$
ρ	density, g/cm^3
ρ_0	density of dry membrane, g/cm^3

$\sigma_{\max}$	maximum effective conductivity of membrane in liquid equilibrated membrane, S/cm
$\Delta\vec{S}^{\pm o}_{iT,\Phi=0}$	standard entropy change of activation for forward elementary reaction ρ
$\nu_{\rho i}$	stoichiometiric coefficient of species i in reaction ρ
$\nu_{\rho e^-}$	stoichiometiric coefficient of electrons in reaction ρ
η	overpotential, $=\Phi - \Phi_0$, V
η_A	anodic overpotential, V
η_C	cathodic overpotential, V
κ	transmission coefficient
$\kappa_{i\alpha}$	partition coefficient of species i in layer α, $= (c_{i\alpha}/c_{iG})_{\mathrm{eq}}$
λ	water loading, number of water molecules per $-SO_3H$ group
λ_m	water loading at monolayer coverage, number of water molecules per $-SO_3H$ group
λ_i^0	equivalent conductance for ionic species i at infinite dilution, $\mathrm{S.cm^2/equiv.}$
μ	fluid mixture viscosity, g/cm.s
μ_i	chemical potential of species i, J/mol
μ_i^e	electrochemical potential of species i, J/mol
δ	ratio of mutual to matrix effective diffusion coefficients, $D^e_{\mathrm{H^+}w} / D^e_{\mathrm{H^+}M}$
ΔH^{o}	enthalpy change for proton solvation, kJ/mol
φ_I	fraction of accessible catalyst surface participating in electrocatalysis
φ_M	fraction of metal crystallite surface that is accessible

Φ	electrode potential, V
Φ_0	equilibrium electrode potential, V
Φ_0^o	standard equilibrium electrode potential for unit activities, V
ϕ	inner potential, V
ϕ_C	thiele modulus
γ_M	roughness factor, cm^2 Pt/cm^2 geometric electrode area
$\gamma^{\pm}$	activity coefficient of transition-state complex
θ_i	fraction of surface sites occupied by species *i*
ρ_I	ionomer density, g/cm^3
σ	effective conductivity of proton-exchange membrane (layer B), S/cm
τ_α	tortuosity factor for porous layer α
ε	volume fraction of water in hydrated membrane, or wet porosity
ε_0	percolation threshold volume fraction of water in hydrated membrane
ε_α	porosity for porous layer α
ω_M	metal catalyst mass fraction, g metal/g catalyst particles

Subscripts and Superscripts

0	open circuit conditions, dry membrane, reference, percolation threshold, infinite dilution
T	at constant temperature *T*
298	at reference temperature, 298 K

A	layer A (anode electrocatalyst)
B	layer B (proton-exchange membrane)
C	layer C (cathode electrocatalyst)
d	diluent gas
D	layer D (anode gas-diffusion backing)
E	layer E (cathode gas-diffusion backing)
G	gas phase
H^+	H_3O^+
i, j	species i, j
I	ionomer
1	H_3O^+
2	H_2O
M	membrane
ρ	reaction ρ
sat	saturated
M	metal, membrane matrix
T	layer T (anode chamber)
S	layer S (cathode chamber)
w	water
α	generic layer
Φ_0	at equilibrium electrode potential
*	per cm^2 metal area

e	effective, electrochemical
liq	equilibrated with liquid
o	standard state
vap	equilibrated with vapor

Abbreviations

BET	Brunauer-Emmett-Teller
DFM	dusty-fluid model
EW	equivalent weight, g dry polymer/mol acid groups
GSM	generalized Stefan-Maxwell equations
PEM	proton-exchange membrane
PEMFC	proton-exchange membrane fuel cell
PFSA	polyperfluorosulfonic acid
RH	relative humidity

I. BACKGROUND

Introduction

Proton-Exchange Membrane (PEM) fuel cells are an extremely attractive option for the replacement of the internal combustion engine in the next generation of fuel-efficient vehicles[1] and stationary power sources. They offer the significant benefit of zero/low local emissions and potentially higher efficiencies[2] vs. modern combustion engines. In comparison to alternate fuel cells, PEM fuel cells (PEMFCs) offer high power densities at low temperatures and low H_2 and air pressures[3]. Recent developments have led to the major advancements of improved PEM durability, lower precious metal catalyst loading, and improved Membrane Electrode Assembly (MEA) designs[3]. As a result, PEMFCs are poised to become a competitive option for power generation.

A major technical challenge that remains is the integration of PEMFCs with the presently available fuel infrastructure. This infrastructure has been developed for the internal combustion engine and based upon the end application, inexpensive natural gas for stationary applications, e.g., Combined Heat and Power (CHP), and high energy density liquid fuels such as gasoline and alcohol for automobiles. Although H_2 is the fuel of choice for PEMFCs systems and there are a number of ways to produce hydrogen as shown in Figure I-1, the inadequate production and distribution network available presently cannot replace gasoline with H_2 for the motive power market without substantial capital investment[4]. As shown in figure I-1, hydrogen containing fuels can be processed and water can be electrolyzed to produce H_2, however due to the low demand of H_2 vs. gasoline, the necessary infrastructure to exploit the abundance of H_2 has not been developed.

Thus, it seems unlikely that a national H_2 distribution grid will be available for PEMFCs in the near future and the commercial deployment of PEMFCs must either be coupled with a novel H_2 storage and re-supply system[5] to overcome hydrogen's low energy density, e.g., use of carbon nanotubes and metal hydrides, or integrated with an on-board reformer to produce H_2 from conventional fuels. The latter approach is an immediate interim solution to an eventual hydrogen economy and is discussed below in a little more detail.

Fuel Reforming

There are a number of fuels available that maybe reformed to produce H_2 including ammonia, natural gas, methanol and gasoline. Since infrastructure is presently available for the widespread production and distribution of liquid fuels such as gasoline and methanol, an integrated gasoline or methanol reformer–PEMFCs offers a promising route for successful deployment of PEMFC powered automotives.

The main chemical processes considered for the production of H_2 from gasoline are Partial Oxidation (POX), Catalytic Steam Reforming (CSR) and Autothermal Reforming (ATR)[2]. As can be seen in Figure I-2, fuel reforming and the necessary CO clean up for low temperature PEMFCs is a complex process. Figure I-2 shows the production of H_2 from natural gas by partial oxidation. The fuel is partially combusted in an exothermic reaction which produces heat for other reactions in the reforming process[2]. A water gas shift reaction is also employed to transform CO to CO_2 in a higher temperature stage (>350°C) and a low temperature stage (~200°C), finally a CO clean up section. In the present generation of processors, there exists a gas clean-up unit in the reformer system prior the PEMFC anode, such as a Preferential CO Oxidation (PROX) reactor, that is necessary to remove trace amounts of CO in the feed. Although this stage adds to processor weight and expense, it is critical as even trace amounts of CO poison conventional PEMFCs.

Although H_2 production has been an important industrial process for the production of ammonia and has been extensively developed it is still a major challenge to miniaturize the technology to develop the compact, quick responding reformer units necessary. For instance, a PEMFC demonstration utilizing the Johnson Matthey 'Hot Spot' reformer produced an overall system efficiency of ~ 30%, which is below that of modern diesel engines[6].

It is hoped that the development of new technologies such as novel microchannel fuel processors[7], selective permeable H_2 thin film Pd alloy membranes[8] that reduce processor complexity will aid in increasing the system efficiency and hastening successful commercialization.

CO Poisoning

The conventional H_2 oxidation catalyst, Pt/C, is extremely intolerant to CO at the standard PEMFC operating temperature of 80°C, as ultra low amounts of CO (>25 ppm) cause significant anode overpotential[9] by inhibiting H_2 oxidation by adsorbing onto the Pt active sites[10]. The change in Gibb's free energy for CO adsorption on Pt. is –130 kJ/mol while that of H_2 adsorption is only –34 kJ/mol[11] demonstrating the preferential adsorption of CO over H_2 on Pt.

As shown in the cell polarization plot in Figure I-3, the introduction of a 100 ppm CO in H_2 feed lowers current dramatically. However, this poisoning is reversible. Full performance is recovered when pure H_2 is restored.

The dramatic decline in performance due to trace amounts of CO is a major constraint to PEMFC operation and there has been a concerted worldwide search to overcoming this issue. Among the possible solutions are:

1. The introduction of an O_2 bleed into the anode chamber either by injection of an air/O_2 stream[12] or by the addition of oxygen evolving compounds[13];
2. CO tolerant alloy catalyst such as PtRu/C[14] and PtMo/C[15], that oxidize CO at lower potentials than Pt;
3. The operation of PEMFCs at higher temperature where CO can be oxidized at lower potentials resulting in high performance PEMFCs[16].

The above 3 approaches are discussed with respect to the implementation and potential utility in addressing CO poisoning in the following sections.

1. O_2 Bleeding

The controlled injection of O_2 into the anode can correct for the deleterious effects of CO. The mechanism for the mitigation of CO poisoning by oxygen bleeding is as follows[17]:

$$\text{Pt} + \text{CO} \rightarrow \text{CO-Pt} \tag{1}$$

$$\text{Pt} + \text{O}_2 \rightarrow \text{O}_2\text{-Pt} \tag{2}$$

$$\text{CO-Pt} + \text{O}_2\text{-Pt} \rightarrow \text{CO}_2 + 2\text{Pt} \tag{3}$$

$$\frac{1}{2}\text{O}_2 + \text{H}_2 \rightarrow \text{H}_2\text{O} \tag{4}$$

The cleansing of the catalyst sites occurs by the catalytic oxidation of adsorbed CO, however, this occurs as indicated in Eq. (4), at the expense of the remaining O_2 oxidizing H_2 fuel. The associated fuel loss and the potential explosion hazards of mixing O_2 in H_2 over a Pt. catalyst, adds to an efficiency loss and design complexity. Thus there has only been limited application of this technology.

2. CO Tolerant Catalysts

There has been an unremitting search for a CO tolerant H_2 Oxidation Reaction (HOR) electro-catalyst. The recent development has focused on Pt alloys that contain a more oxidizable element than Pt, with the ability to activate oxygenated species at lower potentials and thus initiate CO oxidation at lower potentials[15,18]. The continuous oxidation of CO aids in the formation of bare Pt sites that allow the dissociative adsorption of H_2[15,18]. This promoter effect is evident in highly dispersed Ru in PtRu/C alloy catalyst[10] which allows an almost fourfold enhancement as compared to Pt/C electro-catalyst in a CO stream. This bifunctional mechanism is shown below[10]:

$$\text{Ru} + \text{H}_2\text{O} \rightarrow \text{Ru-OH} + \text{H}^+ + \text{e}^- \tag{6}$$

$$\text{Ru-OH} + \text{Pt-CO} \rightarrow \text{CO}_2 + \text{H}^+ + \text{e}^- \tag{7}$$

The development of a PtMo/C catalyst that demonstrates even higher CO tolerance over state-of-the-art PtRu/C[15] indicates that practical CO tolerant stable electro-catalysts will eventually be developed.

3. Higher Temperature Operation

As shown in Figure I-4[16], the higher temperature operation lowers CO induced anode overpotential over Pt and Pt alloyelectro-catalysts. At 115°C the overpotential has reduced to only 0.1V, which is similar to the overpotential for HOR. The decrease of CO overpotential with increasing cell temperature in a CO feed stream is due to the exothermic chemisorption of CO on Pt sites[16]. At higher temperatures, the binding energy of CO to the active sites decreases, reducing surface coverage and allowing H_2 to be oxidized. Furthermore, CO is removed at higher temperatures via the electrocatalytic water-gas shift reaction (EWGSR)[19]. High temperature CO tolerance is demonstrated in Phosphoric Acid Fuel Cells (PAFC) that can operate with up to a 5% CO/H_2 feed with only a 0.1V loss in overpotential at 200°C[20].Thus it appears that the first generation of commercial gasoline fueled PEMFCs systems will probably achieve the CO tolerance with a combination of elevated temperature operation and Pt alloy CO tolerant electro-catalyst.

Motivation for Development of Higher Temperature and Low RH PEMs

In addition to the increase in CO tolerance obtained with high temperature operation, improved thermal management is facilitated and design constraints of other balance-of-plant (BOP) units are relaxed, e.g. the required duty of the radiator and compressor are dramatically reduced if the PEMFC stack requires less water[21].

However, higher temperature operation is limited in that the operating temperature must be below the normal boiling point of water in atmospheric fuel cells. As can be seen from Figure I-5[22], operation at 110°C dramatically reduces performance in atmospheric fuel cells. At 110°C, the measured performance is only a tenth of the 80°C performance when the anode and cathode saturators are operated at 95°C and 90°C respectively. Consequently the present generation of PEMFCs is shackled with elaborate water management issues as hydrated PEMs[23] are critical for high performance, and any alleviation of this hydration requirement would be highly attractive.

The major reason for this decline in performance is presented in Figure I-6[24], It is observed that water is required for high proton conduction in the standard fluorocarbon polymers presently used as PEMs, such as Nafion®. The conductivity of Nafion® rises dramatically with water content of the membrane, attaining the highest conductivity when the membrane is completely impregnated in liquid water[25]. Figure I-7 (a) shows the chemical structure of Nafion® with a hydrophobic PTFE backbone and the sulfonic acid clusters. The presence of the hydrophobic backbone and the hydrophilic ionic clusters results in the structure depicted in Figure I-7 (b)[26]. It is in the hydrophilic region that water is sorbed and swells the PEM, while the hydrophobic region constrains this swelling to maintain membrane integrity.

Thus, at higher temperatures (> 100°C) and under ambient pressure, the PEM loses conductivity due to membrane dehydration. At high temperature, increasing the partial pressure of water in a pressurized feed can hydrate the PEM. However the addition of a compressor increases the parasitic costs resulting in a substantial decline in the overall efficiency.[20]

There is thus ample incentive for the development of PEMs that can operate at temperatures at or above 100°C under atmospheric pressure, i.e., without the necessity of substantial humidification (under low RH). Engineering PEMs to maintain high conductivity under these conditions, would address the twin challenges of CO poisoning and hydration requirements. Further benefits include accelerating the development of *insitu* reforming fuel cells, such as Direct Methanol Fuel Cells (DMFC)[27,28,29], which perform substantially better at higher temperatures. The methanol oxidation involves CO as a intermediate that poisons the catalyst. This would be mitigated at higher temperatures.

As a result of the significant benefits accruing from superior performing higher temperature, low RH PEM fuel cell, the development of higher temperature PEMs is an important goal.

Thesis Objectives

The overall objective of the thesis is a PEM that demonstrates higher performance than the present generation of commercially available PEMs at high temperature (>100°C) and low RH (< 50%).

To develop these PEMs, the objective must include an understanding of the phenomena that control conductivity of PEMs at high temperature/low RH. Additionally a comprehension of the issues that impact overall fuel cell performance is necessary as promising PEMs must demonstrate improved fuel cell performance. Utilizing the insight gained as a result of modeling PEM conductivity and overall fuel cell performance, the design and development of high temperature/low RH PEMs can be successfully undertaken.

The objectives of the thesis are thus:

(1) A model that predicts the conductivity of the PEM as a function of RH and temperature.

(2) A model that is able to capture the significant characteristics of PEM fuel cell performance based on the microstructure of the membrane-electrode assembly (MEA).

(3) Analysis of the potential of novel composite PEMs designed and developed for higher temperature/lower RH operation.

Summary of Thesis

Chapter II[30] is a description of a transport model that describes the conductivity through the PEM in the liquid phase and the vapor phase at different temperatures. The model is based on the Dusty Fluid Model and captures all the significant aspects of the experimental results. The model provides understanding of the effects of temperature and relative humidity on PEM conductivity, and provides a useful beginning for the rational design of higher temperature PEMs.

Chapter III[31] is a membrane reactor model of the entire PEMFC. This model includes the PEM transport model to account for the ohmic loss of the membrane, the DFM formalism to treat diffusion in the electrode, and the Butler-Volmer kinetic equation to treat kinetics of the catalyst layer. Simulation results are presented and the model is used to understand the various aspects of higher temperature and low relative humidity, PEM conductivity, low catalyst layer conductivity and reactant pressure.

Chapter IV details the previous work on higher temperature PEMs and the various approaches used so far. The design and the characteristics of a higher temperature composite PEM are described. The experimental work on the combination of Nafion® and superacidic additives to fabricate PEMs is also provided, as well as water uptake, conductivity and fuel cell test results. This chapter demonstrates the promising potential of these composites as higher temperature PEMs.

Chapter V provides a conclusion of the work and the future potential research directions. This section also includes preliminary new experimental results and the subsequent research necessary for the development of superior performance, low RH, high temperature PEMs.

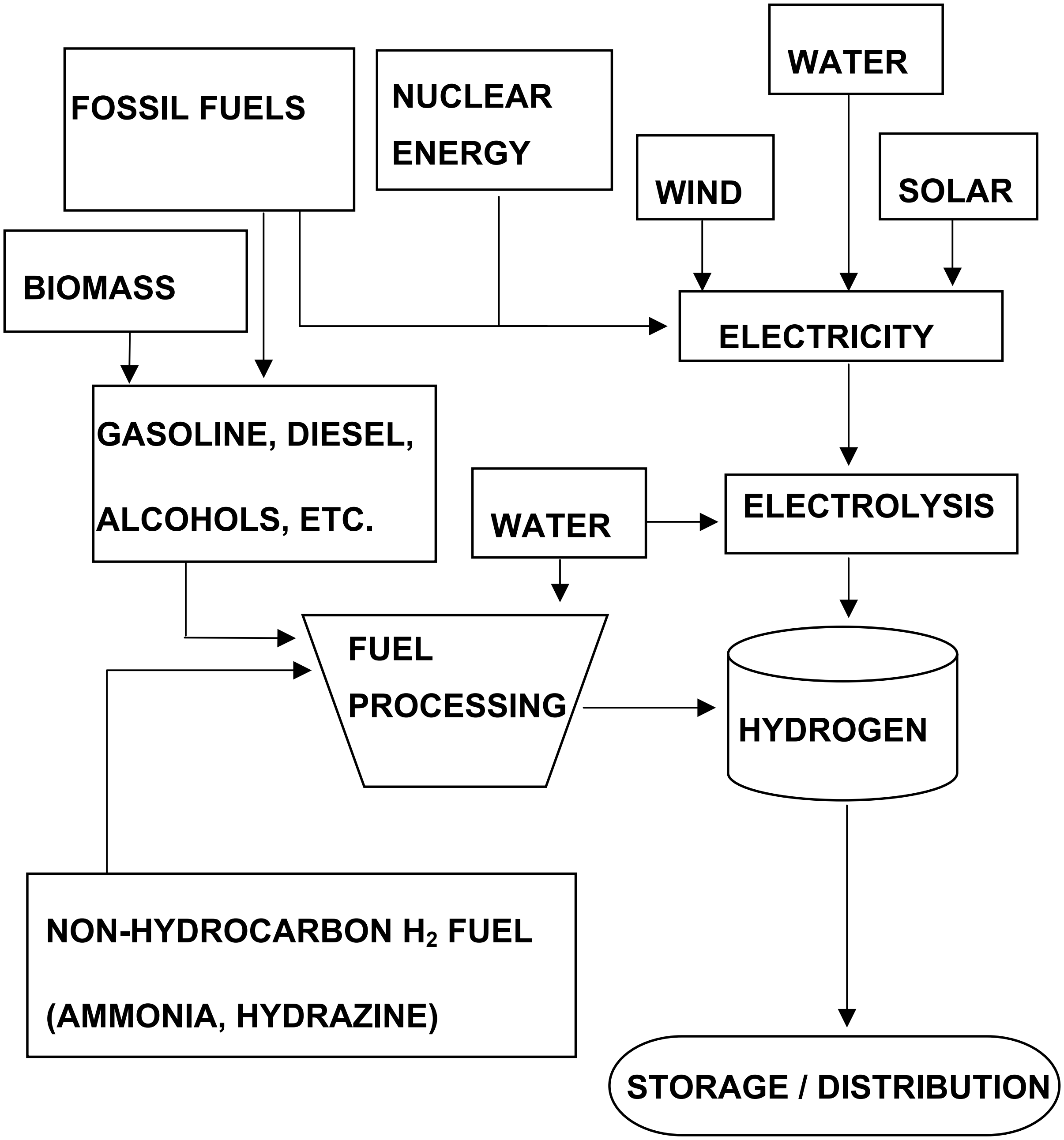

Figure I-1: Block diagram showing possible production routes for H_2[2]. Although there are numerous sources of H_2, the lack of demand has resulted in insignificant H2 production and no national distribution system.

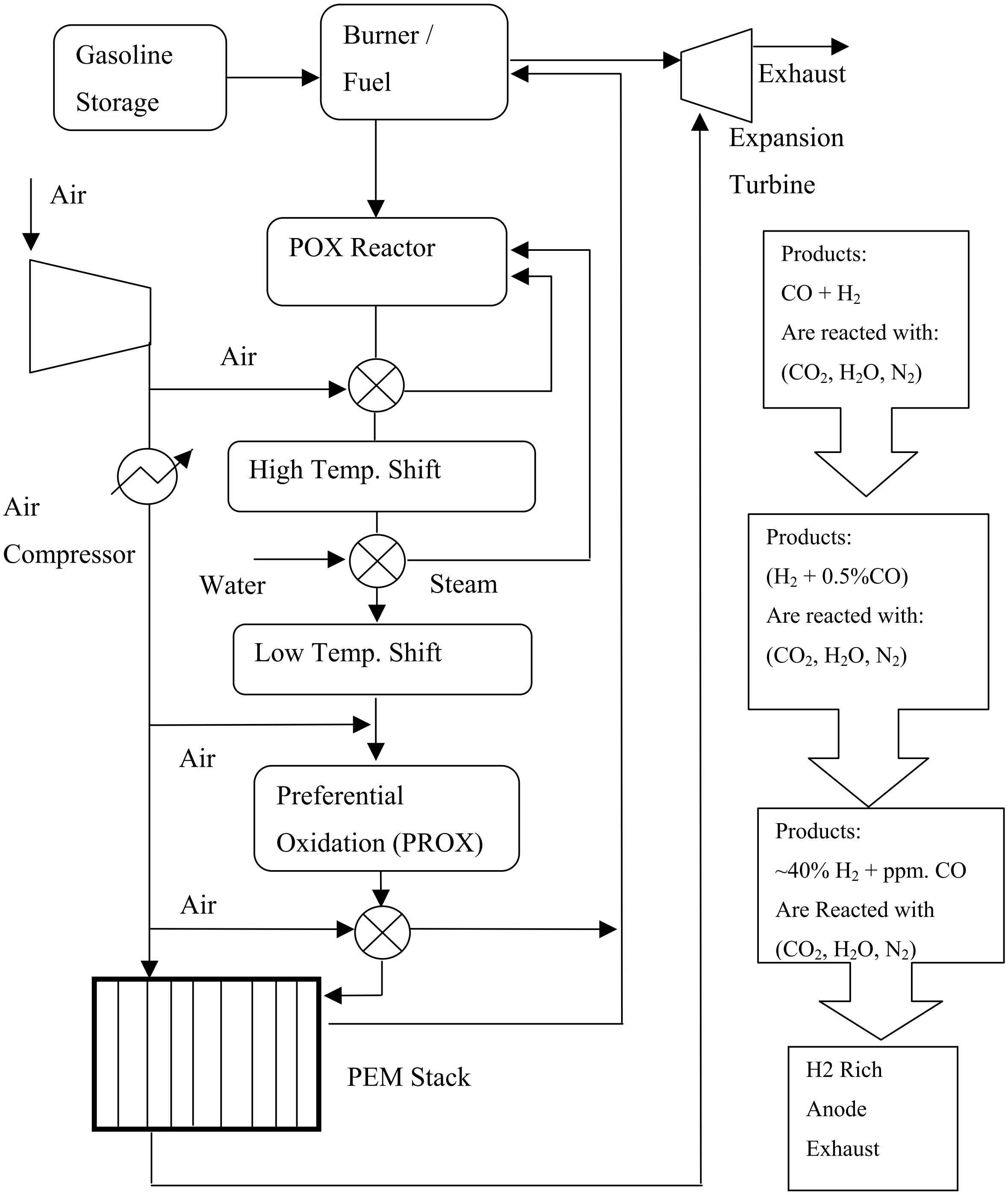

Figure I-2: Block diagram showing various stages in a PEMFC fuel processor[2].

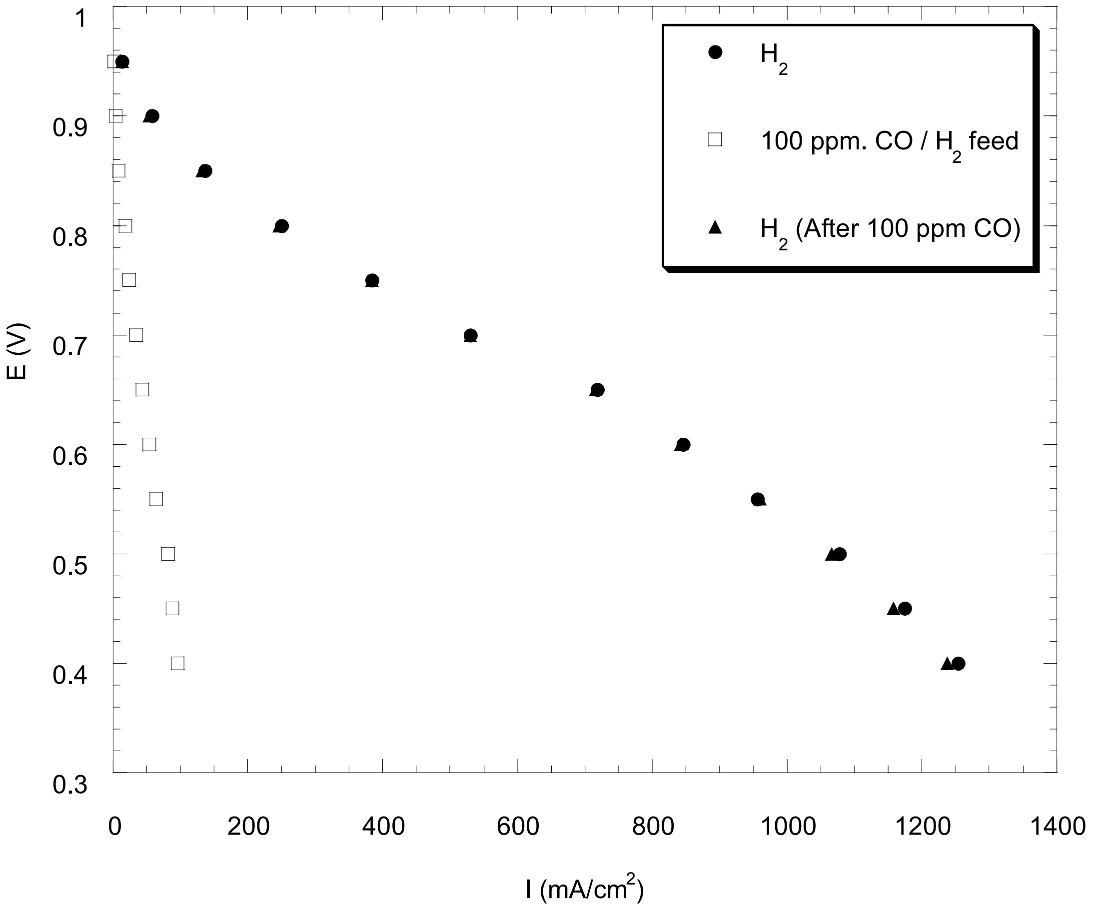

Figure I-3: CO poisoning of Pt electro-catalyst in a PEMFC operated at 3 atm. (O_2/H_2) at 80°C with Nafion® 117 MEA. Anode setpoint 90°C, Cathode setpoint 90°C. S.S. ELAT® electrode with 0.34 mg/cm^2 Pt. loading and 0.7 mg/cm^2 Nafion® loading. Polarization measurements are made before, during and after CO poisoning.

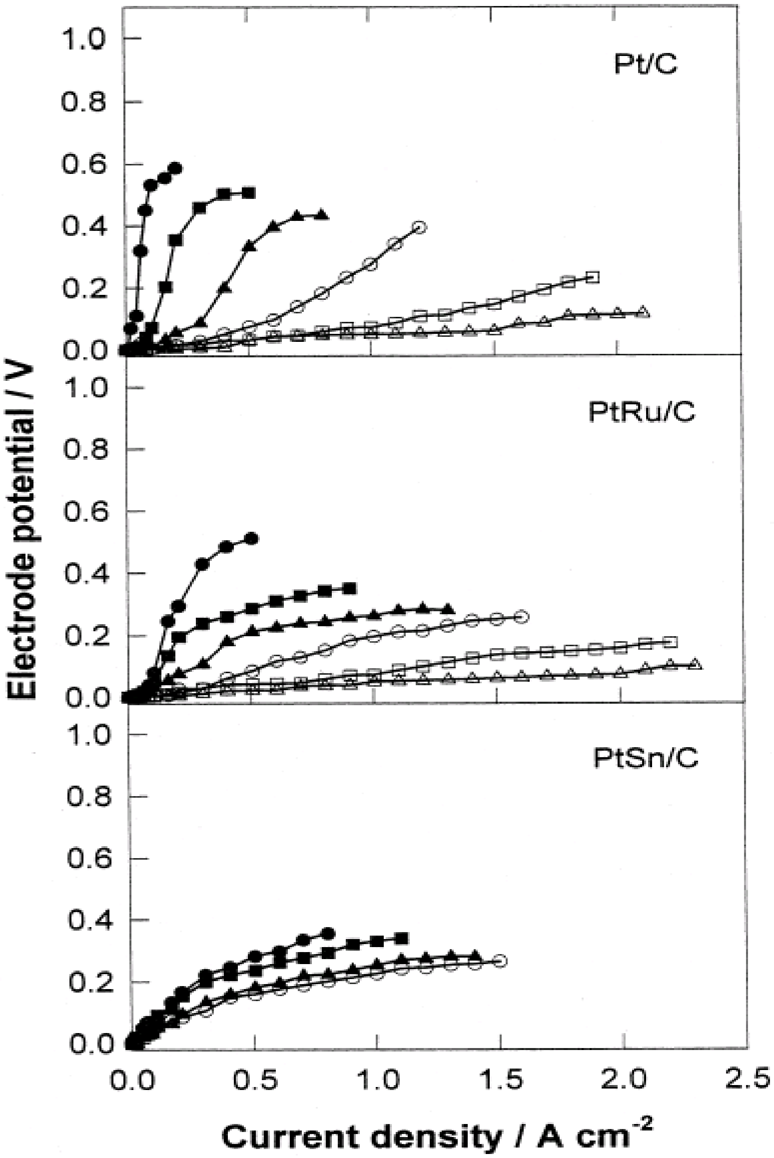

Figure I-4: The effect of temperature on anode polarization with 20 ppm CO / H_2 for Pt/C, PtRu/C and PtSn/C at several different temperatures: ● 40°C, ■ 55°C, ▲70°C, ○ 85°C, □ 100°C, Δ 115°C [16].

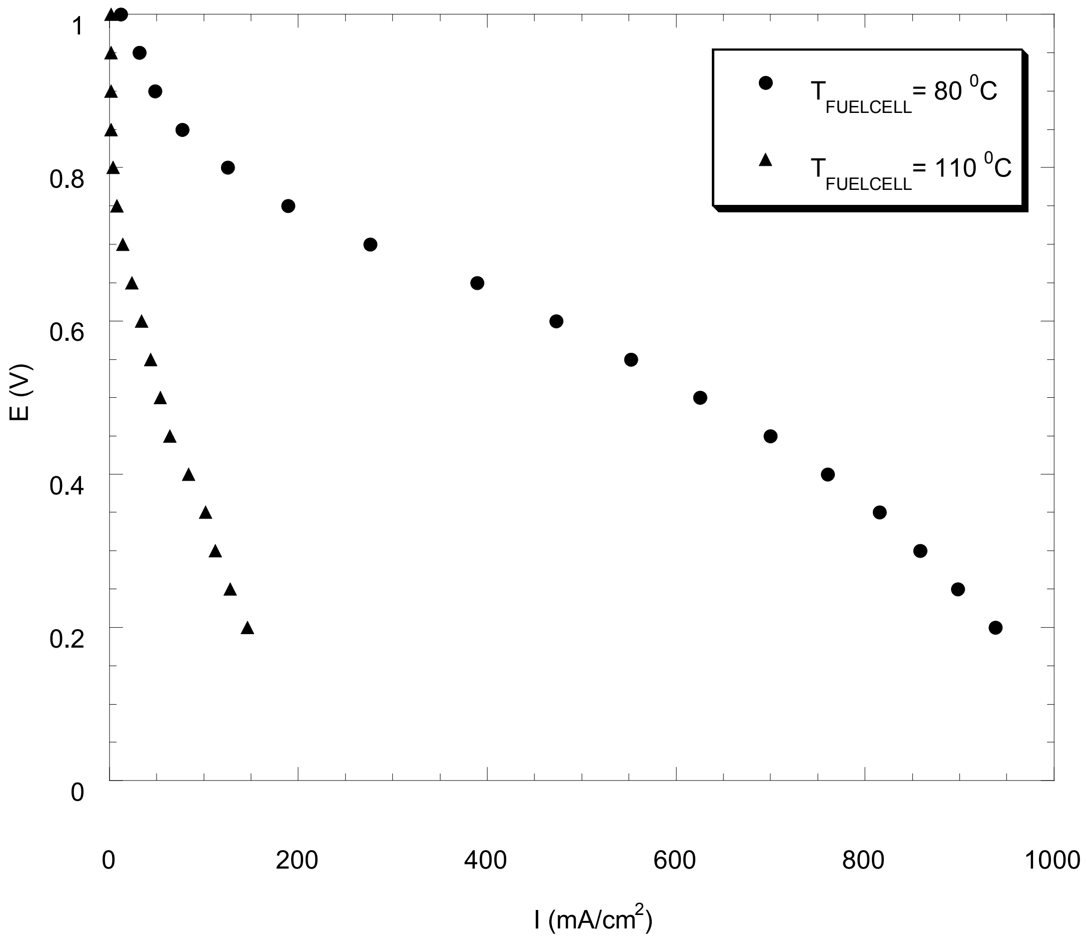

Figure I-5: Loss of performance at higher temperature. Operation in PEMFC at 2 atm H_2 / O_2. Humidifiers maintained at 90°C (cathode) and 95°C (anode)[22] S.S. ELAT® electrode with 0.34 mg/cm^2 Pt. loading.

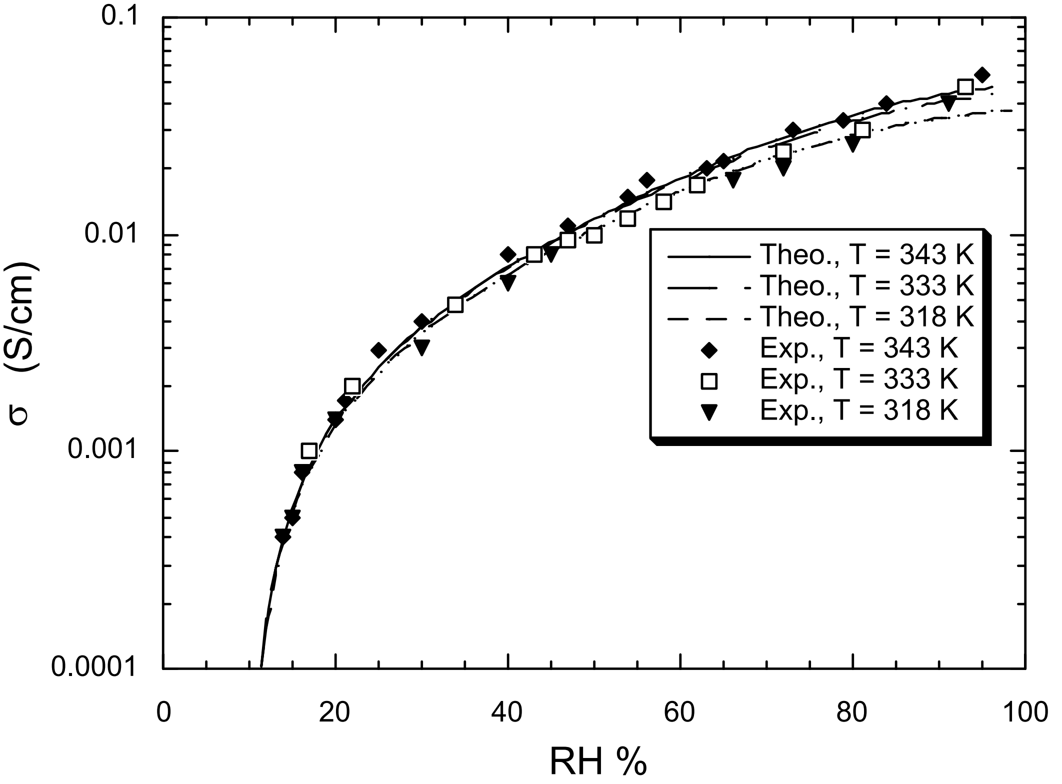

Figure I-6: Nafion 117 equilibrated in water vapor vs. water vapor activity at different temperatures and simulation results[30].

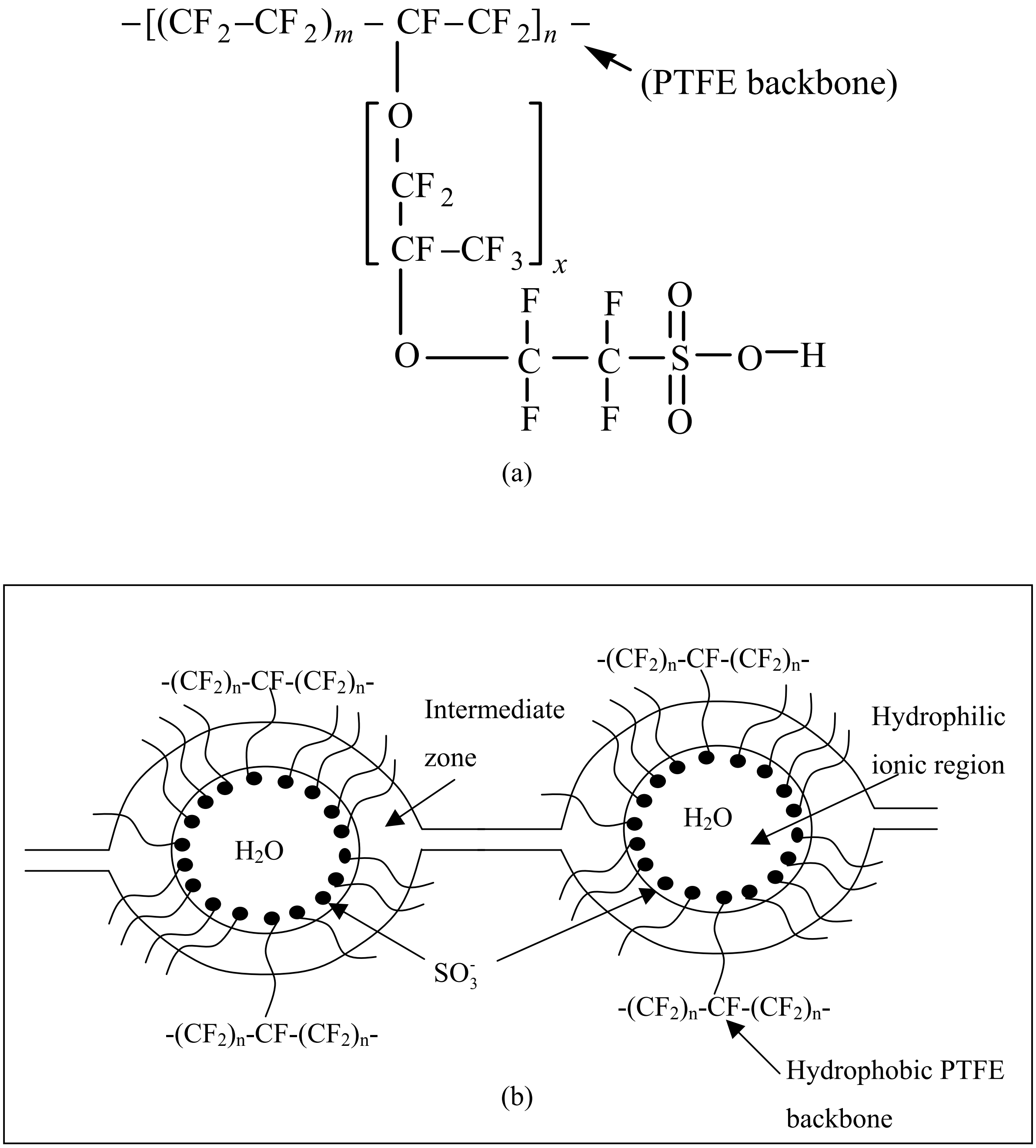

Figure I-7: (a) The chemical structure for Nafion®. (b) Model proposed for the Nafion® membrane showing the potential structure of the hydrophobic, hydrophilic and intermediate regions[26].

REFERENCES

1 P. Patil, *J. Power Sources*, **49**, 169 (1994).

2 L. Carrette, K.A. Friedrich and U. Stimming, *Fuel Cells* **1**, 1(5) (2001).

3 B.C.H. Steele, *J. Mat. Sci*., **36**, 1053 (2001).

4 M. Jacoby, *Chem. & Eng, News* **81(3)**, 32 (2003).

5 Ch. N Borrani-Bird, *J. Power Sources* **61**, 33 (1996).

6 Mercatox Project, EC Contract JOE3-CT96-002 (Final Report, 1999).

7 S.G. Chalk, J.F. Miller and F.W. Wagner *J. Mat. Sci*., **86**, 40 (2000).

8 A. Heinzel, R. Nolte, K. Ledjeff-Hey and M. Zedda, *Electrochimica Acta* **43**, 3817 (1998).

9 S. Gottesfeld, J. Pafford, *J. Electrochem. Soc*. **135**, 2651 (1988).

10 H.-F. Oetjen, V.M. Schmmidt, U. Stimming and F. Trila, *J. Electrochem. Soc*. **143**, 3838 (1996).

11 N. M. Markovic, C. A. Lucas, B. N. Grgur and P. N. Ross, *J. Phys. Chem*., *B*, **103**, 9616 (1999).

12 M. S. Wilson, T.E. Springer, T.A. Zawodzinski, S.Gottesfeld Proc. 28th Intersociety Energy Conversion Engineering Conf., Atlanta, Georgia, Vol. 1, pp1203-1208 (1993)

13 V.M. Schmidt, H.-F. Oetjen and J. Divisek, *J. Electrochem. Soc*. **144**, L237 (1997).

14 R. Iannielo, V.M. Schmidt, U. Stimming, J. Strumper, A. Wallau, *Electrochimica Acta* **39**, 1863 (1994).

15 S.J. Lee, S.Mukerjee, E.A Ticianelli,,J. McBreen, B.N. Grgur, N.M. Markovic, P.N. Ross, J.R. Giallombardo and E.S. De Castro, *Electrochemical and Solid State Letters* **2**(1), 12 (1999).

16 S.J. Lee, S.Mukerjee, E.A Ticianelli, and J. McBreen, *Electrochimica Acta* **44**, 3283 (1999).

---

17 S. Gottesfeld and T. A. Zawodzinski, *Polymer Electrolyte Fuel Cells*, in R. Alkire, H. Gerischer, D. Kolb, C. Tobias, eds., Advances in Electrochemical Science and Engineering, **5**, 197 (1998).

18 M. Watanabe and S. Motoo, *J. Electroanal Chem*. **60**, 267 (1975).

19 J. Zhang, T. Thampan and R. Datta, *J. Electrochem. Soc*. **149**, 6 A765 (2002).

20 J.H. Hirschenofer, D.B. Stauffer, R.R. Engleman and M.G. Klett, *Fuel Cell 4th Edition* Nov. 1998 DOE/FETC-99/1076.

21 M. Mathias, *Proton Exchange Membrane Nanocomposites for Fuel Cells*, Advances in Materials for Proton Exchange Membrane Fuel Cell Systems, ACS, Pacific Grove, CA Feb. 23-27 (2003).

22 S.Malhotra and R. Datta, *J. Electrochem. Soc.* **144**, L23 (1997).

23 Bernardi, D. M., *J. Electrochem. Soc.*, **137**, 3344 (1990).

24 Y. Sone, P. Ekdunge and D. Simonsson, *J. Electrochem. Soc.,* **143**, 1254 (1996).

25 P. Choi and R. Datta, *In Press*.

26 T. D. Gierke, G. E. Munn, and F.C. Wilson, *J. Polym. Sci*., **19**, 1687 (1981).

27 P.L. Antonucci, A.S. Arico, P. Creti, E. Ramunni and V. Antonucci , *Solid Sate Ionics* **125**, 431 (1999).

28 N. Miyake, J.S. Wainright and R.F. Savinell *J. Electrochem. Soc.,* **148**, 8 A905 (1996).

29 D.H. Jung, S.Y. Cho, D.H. Peck, D.R. Shin and J.S. Kim, *J. Power Sources* **106**, 173 (2002).

30 T. Thampan, S. Malhotra, H. Tang and R. Datta, *J. Electrochem*. *Soc*., **147**, 1 3242 (2000).

31 T. Thampan, S. Malhotra, J. Zhang and R.Datta, *Catalysis Today*, **67**, 15 (2001).

II. MODELING OF CONDUCTIVE TRANSPORT IN PROTON-EXCHANGE MEMBRANES FOR FUEL CELLS[#],[*]

Abstract

An adequate understanding of the conductivity of polyperfluorosulfonic acid (PFSA) membranes as a function of water content, or relative humidity, and temperature is necessary for an analysis of the functioning of proton-exchange membrane (PEM) fuel cells. Although, much work has been done towards elucidating the microstructure and conduction mechanism in PFSA, a satisfactory theoretical model with a minimum of fitted parameters is not yet available. Such a model is developed here for the conduction of protons in hydrated Nafion® or like membranes based on the dusty-fluid model for the transport and percolation model for the structural aspects. Further, thermodynamics of dissociation of the acid groups in the presence of polar solvents such as water is included. The sorption of solvent from vapor is modeled using a finite-layers Brunauer-Emmett-Teller (BET) model. With the only fitted parameters employed being the BET constants, determined independently, and the ratio of diffusion coefficients representing the interaction of the protonated solvent molecules with solvent and that with the membrane, the model provides excellent correlation with a variety of experimental data.

[#] This work was published in *J. Electrochem. Soc.*, **147** 1 (2000) 3242.

[*] The contributions of S. Mahotra, H. Tang and R. Datta are gratefully acknowledged.

Introduction

The proton-exchange membrane (PEM) fuel cell has lately emerged as a highly promising power source for a wide range of applications. The solid polymer electrolyte utilized in these fuel cells is typically a polyperfluorosulfonic acid (PFSA) membrane (e.g., Nafion®, manufactured by Dupont), that provides excellent performance in the presence of water by virtue of its strong acidity, low permeability of hydrogen and oxygen, and good electrochemical stability in the presence of electrocatalysts. This has allowed the development of low temperature PEM fuel cells with impressive current densities. These membranes have also been widely utilized in the chlor-alkali industry. However, an understanding and modeling of the transport of ionic species through these ion-exchange membranes is not yet adequately developed, especially for proton transport, which is the focus of this paper.

There are numerous studies on the nanostructural aspects of the Nafion® membranes.[1-15] The unique properties of these PFSA membranes are attributable to their polymer structure that consists of a fluorocarbon, Teflon-like, backbone with side-chains terminating in $-SO_3H$ groups. In the presence of water or other polar solvents, these sulfonic acid groups dissociate, protonating the solvent molecules and forming a hydrophilic phase that also includes the solvated $-SO_3^-$ ions tethered to the hydrophobic backbone through the side-chains.[1] Based on small angle X-ray and other studies,[2–4] Gierke and co-workers[2,15] proposed in their “cluster–network model” that the incompatibility of the fluorocarbon and the ionic/solvent component leads to the formation of inverted micelles, existing as near-spherical aggregates, 3-5 nm in diameter, depending upon the level of hydration. These are interconnected through short narrow channels, 1-2 nm in diameter, to provide a network for diffusion interspersed throughout the fluorocarbon matrix. The extent of the solvent uptake and membrane swelling is controlled by a balance between the internal osmotic pressure of solvent in the pores and the elastic forces of the polymer matrix,[16] which, in turn, depend upon the temperature and membrane pretreatment. The cluster–network model provides a suitable structural framework for the development of ionic transport models in these membranes akin to those in porous media, e.g., the parallel-pore model, or the percolation model.

There is, of course, substantial literature on the modeling of transport through ion-exchange membranes,[17–20] although the majority of the work deals with the transport of electrolytes, i.e., salt/acid/base solutions, rather than with proton transport. The interest in diffusion of electrolytes through ion-exchange membranes stems mainly from their chlor-alkali and electro-dialysis applications. A theoretical model of ion-exchange membranes involves: 1) a structural model, and 2) a transport model. The cluster-network, the parallel-pore, and the percolation models referred to above belong to the former. As to the latter, there are three alternate approaches: 1) phenomenological models based on nonequilibrium thermodynamics;[21,22] 2) models based on the Nernst-Planck equations;[19,23,24] and 3) those based on the generalized Stefan-Maxwell (GSM) equations,[25–27] or equivalently, the frictional formalism of Spiegler.[20,28] The last two are of a similar form, the former involving diffusion coefficients and the latter incorporating frictional coefficients. The transport model of choice is suitably adapted to the chosen structural model to provide an overall description of ion transport in a membrane.

Fairly sophisticated capillary pore models incorporating the Nernst-Planck equations to describe diffusion, the Navier-Stokes equations for convective flow, and the Poisson-Boltzmann equation to describe the radial potential profile within individual pores have been developed,[23,24,29,30] that adequately simulate the transport of alkali metal ions through the membrane. However, the GSM equations, or equivalently Spiegler's frictional model, represent a more general starting point, the Nernst-Planck equations being strictly applicable to dilute solutions.[31] The GSM equations have been utilized with a fair degree of success by Spiegler,[28] Meares *et al.*,[20] Pintauro and Bennion,[27] Wesselingh *et al*. (1995),[32] and van der Stegen *et al.*,[33] for describing the transport of alkali electrolytes in ion-exchange membranes. The main limitation, however, is that many of the necessary GSM diffusion coefficients are not independently available in the literature, requiring their treatment as fitted parameters.[33]

The status of the modeling of transport of protons in hydrated PFSA membranes is less satisfactory, although there is much of relevance in the electrolyte transport literature. A number of experimental studies have, however, been performed under a variety of conditions.[10,15-18] These conductivity data show that at very low water uptake, i.e., for number of water molecules per $-SO_3H$ group, $\lambda < 2$, the Nafion® membrane behaves essentially as an insulator, the conductivity σ being of the order of 10^{-7} S/cm.[34] Beyond a critical hydration level uptake ($\lambda \approx 2$), or a "percolation" threshold, σ rises dramatically with water uptake reaching a plateau in the semiconductor range, of the order of about 10^{-1} S/cm, for a membrane immersed in water. In general, σ also rises with temperature, although the data of Sone *et al.*[35] indicate a low temperature range with anamolous behavior. Since the water uptake is determined by relative humidity (RH), temperature and membrane pretreatment, these are the key factors affecting membrane conductivity.

Fadley and Wallace[36] developed an absolute rate model for conduction in PEMs, in which the effect of hydration was included by assuming that it affected the Gibbs free energy of activation. The model agreed with data in the range of $0 < \lambda < 5$, but not beyond that. Hsu *et al.*[10] developed a percolation model to describe the effect of water uptake on conductivity, i.e., $\sigma = \sigma_0(\varepsilon - \varepsilon_0)^q$. The expression fitted the data well with the following parameters $q = 1.5$, $\sigma_0 = 0.16$ S/cm, and $\varepsilon_0 = 0.1$. No attempt, however, was made to predict σ_0 in terms of more fundamental transport parameters. Morris and Sun[37] also found the percolation model to be accurate but with different fitted parameters, namely, $q = 1.95$, $\sigma_0 = 0.125$ S/cm, and $\varepsilon_0 = 0.06$. Springer *et al.*[38] developed an empirical model to linearly relate the conductivity to λ, instead of to ε, and used the Arrhenius equation to describe temperature dependence of conductivity. In turn, λ was fitted to RH through a third-order polynomial. Eikerling *et al.*,[39] extended the percolation model by considering two different types of pores, those with only surface water and others containing additional bulk-like water, and ascribed different conductivities to each. Then by connecting the pores randomly within the framework of the random network theory, they predicted conductivity as a function of hydration level. Bernardi and Verbrugge[40] utilized the Nernst-Planck equation along with a parallel pore model to describe membrane conductivity within a larger model to predict PEM fuel cell performance. However, a direct comparison of the model with conductivity data was not provided. More recently, there have been attempts to do molecular simulation of proton transport within pores of Nafion®.[41,42]

The model developed here is based on the assumption that the diffusion mechanism in hydrated PEMs is similar to that in the liquid, i.e., protons are transported as hydronium ions via mutual diffusion, Grotthus mechanism, and flow through pores containing water within the ionomer,[34] rather than, e.g., through surface site-hopping. The hydronium ions in the liquid phase result from dissociation of the acid groups. The obstruction presented by the polymer matrix to the diffusion of hydronium ions is modeled as an additional frictional, or diffusional, interaction with the large "dust" particles (Fig. 1), representing the polymer species in the spirit of the "dusty-fluid model" (DFM),[43] with a molecular weight equal to the polymer equivalent weight (EW). The space filling aspects and tortuosity of the polymer matrix are accounted through the DFM structural constants, which also include provision for the absence of conduction below a percolation threshold. Thermodynamics of sulfonic acid group solvation and water sorption isotherm are included as well, as is the swelling of the membrane. Since it has been the subject of considerable study,[44] the model is utilized for hydrated Nafion®. However, it should be applicable to other PEMs as well as to solvents other than water.

Theory

General Transport Model for Ion-Exchange Membranes.-We start with the generalized Stefan-Maxwell equations with the electrochemical potential gradient as the driving force for describing diffusional velocity of species *i*, $\boldsymbol{v}_i^D$, in a *continuum* fluid[26,31]

$$-\frac{c_i}{RT}\nabla_T\mu_i^e = \sum_{\substack{j=1\\ j\neq i}}^{n}\frac{c_i c_j}{cD_{ij}}(\mathbf{v}_i^D - \mathbf{v}_j^D) \qquad (i = 1,2,\ldots,n) \qquad (1)$$

In Eq. 1, the electrochemical potential gradient at constant temperature is composed of chemical and electrical potential gradients:

$$\nabla_T\mu_i^e = \nabla_T\mu_i + z_iF\nabla\Phi = \left(RT\nabla\ln c_i + RT\nabla\ln\gamma_i + \bar{V}_i\nabla p\right) + z_iF\nabla\Phi \qquad (2)$$

Equation 1 may alternatively be written as per the frictional formalism of Spiegler[28]

$$-c_i\nabla_T\mu_i^e = \sum_{\substack{j=1\\ j\neq i}}^{n}c_i c_j\zeta_{ij}(\mathbf{v}_i^D - \mathbf{v}_j^D) \qquad (i = 1,2,\ldots,n) \qquad (3)$$

where the frictional coefficients and the diffusion coefficients are interrelated via

$$\zeta_{ij} \equiv \frac{RT}{cD_{ij}} \tag{4}$$

where ζ_{ij} is the frictional coefficient for the interaction between species i and j, defined by assuming that the frictional force $\boldsymbol{F}_{ij}^*$ (N/mol i) between species i and j, the latter being present in the mixture at unit concentration, is given by, $\mathbf{F}_{ij}^* \equiv -\zeta_{ij}(\mathbf{v}_i^D - \mathbf{v}_j^D)$. These, in turn, are related to Spiegler's[28] frictional coefficient f_{ij} by $c_j\zeta_{ij} = f_{ij}$. When applied to diffusional transport within an ion-exchange membrane, itself considered simply as an additional, albeit a large molecular weight "dust" species ($j = M$), within the framework of the dusty-fluid model (DFM),[43] constrained by external clamping forces to be stationary ($\boldsymbol{v}_M^D = 0$. In addition, of course, $\boldsymbol{v} = 0$), Eq. 1 results in

$$-\frac{c_i}{RT}\nabla_T\mu_i^e = \sum_{\substack{j=1\\ j\neq i}}^{n}\frac{c_ic_j}{cD_{ij}^e}(\mathbf{v}_i^D - \mathbf{v}_j^D) + \frac{c_i}{D_{iM}^e}\mathbf{v}_i^D \qquad (i=1,2,\ldots,n) \tag{5}$$

where the continuum diffusion coefficients D_{ij} have been replaced by their "effective" counterparts, D_{ij}^e, to account for space-filling aspect and tortuosity of the membrane, the latter reducing the effective driving force gradient. Further, D_{iM}^e, or equivalently ζ_{iM}^e, accounts for the frictional interaction between species i and the matrix, or dust particles. It is to be noted again that each sulfonic acid group along with its associated PTFE backbone is treated as the dust species M, with an EW ≈ 1100 for Nafion®. The effective and contiuum diffusion coefficients are interrelated through[45]

$$D_{ij}^e = K_1 D_{ij} \tag{6}$$

where K_1 is the DFM structural constant for molecular diffusion coefficient. Frequently, the relation $K_1 = \varepsilon^q$ suffices, where ε is the volume fraction of the phase through which the diffusion is occurring. A common value for the so-called Bruggeman exponent, $q = 1.5$.[31,32] Alternatively, if one adopts the percolation model for this,[15] which includes a percolation threshold ε_0 below which the diffusion is improbable owing to the lack of connectivity of phase through which the diffusion occurs, then

$$K_1 = (\varepsilon - \varepsilon_0)^q \tag{7}$$

where the critical exponent q is a universal constant predicted to be about 1.5,[15] although it is frequently used as a fitted parameter.[37] The threshold value ε_0 is best determined from experiments as a fitted parameter. This model, with $q = 1.5$, is adopted here in view of the well-known percolation behavior of conductivity in proton-exchange membranes.[15]

The effective membrane diffusion coefficient may similarly be written as

$$D_{iM}^{e} = K_0 D_{iM} \tag{8}$$

where K_0 is the DFM constant for matrix diffusion coefficient. Unlike for K_1, however, no general relationship is available to relate K_0 to the structural properties of the membrane for the case of liquid-phase diffusion, although for gaseous diffusion, relations are available for the corresponding effective Knudsen diffusion coefficient in terms of the porosity, tortuosity factor, and the mean pore radius.[45] As a result, there is little choice but to treat it as a fitted parameter here, as commonly done.[32,33]

The total species velocity, in general, comprises a convective component $\boldsymbol{v}$ in addition to the diffusive component, i.e., $\mathbf{v}_i = \mathbf{v}_i^D + \mathbf{v}$ (except for matrix M, for which there is no convective velocity as well). The convective velocity resulting from a pressure gradient and/or potential gradient may be given by Schlögl's equation[23]

$$\mathbf{v} = -\frac{B_0}{\eta}\left[\nabla p + \left(\sum_{j=1}^{n} c_j z_j\right) F \nabla \Phi\right] \tag{9}$$

where the term in the parenthesis accounts for all charged species in the liquid phase, which for the case of proton transport in fuel cells is only hydronium ion, but would involve other species for electrolyte transport. Implicit in equation (9) is the assumption of radial uniformity of charged species within the pores. In case radial non-uniformity is accounted, e.g., in terms of the double-layer theory, the effective d'Arcy permeability for pressure-driven flow B_0 and that for electro-osmosis B_Φ would not be the same.[40, 46] This difference is ignored here. Utilizing Eq. 9 in Eq. 5, thus, DFM takes the following form in terms of the total species fluxes $\boldsymbol{N}_i \equiv c_i \boldsymbol{v}_i$:

$$-\frac{c_i}{RT}\nabla_T \mu_i^e = \sum_{\substack{j=1 \\ j\neq i}}^{n} \frac{1}{cD_{ij}^e}(c_j \mathbf{N}_i - c_i \mathbf{N}_j) + \frac{\mathbf{N}_i}{D_{iM}^e} + \frac{c_i B_0}{\eta D_{iM}^e}\left[\nabla p + \left(\sum_{j=1}^{n} c_j z_j\right) F \nabla \Phi\right] \tag{10}$$

$$(i = 1, 2, \ldots, n)$$

Summing this over all species, the Stefan-Maxwell terms cancel out, resulting in

$$\left[\nabla p + \left(\sum_{j=1}^{n} c_j z_j\right) F \nabla \Phi\right] = -\frac{RT}{W}\sum_{j=1}^{n}\frac{\mathbf{N}_j}{D_{jM}^{e}} \tag{11}$$

where the term

$$W \equiv 1 + \frac{B_0 cRT}{\eta}\sum_{h=1}^{n}\frac{x_h}{D_{hM}^{e}} \tag{12}$$

An alternate form of Eq. 10 is, thus, obtained by using Eq. 8 to eliminate the convection driving force in the brackets

$$-\frac{c_i}{RT}\nabla_T \mu_i^e = \sum_{\substack{j=1\\ j\neq i}}^{n}\frac{1}{cD_{ij}^{e}}(c_j\mathbf{N}_i - c_i\mathbf{N}_j) + \frac{\mathbf{N}_i}{D_{iM}^{e}} - \frac{c_i B_0 RT}{\eta D_{iM}^{e} W}\sum_{j=1}^{n}\frac{\mathbf{N}_j}{D_{jM}^{e}} \qquad (i = 1,2,\ldots,n) \tag{13}$$

which may alternately be written in the more compact form

$$-\frac{c_i}{RT}\nabla_T \mu_i^e = \sum_{j=1}^{n} H_{ij}^{e}\mathbf{N}_j \qquad (i=1,2,\ldots,n) \tag{14}$$

with the effective frictional coefficients incorporating the convective terms being

$$H_{ij}^{e} = (\delta_{ij} - 1)\left(\frac{x_i}{D_{ij}^{e}} + \frac{cRTB_0 x_i}{\eta W D_{iM}^{e} D_{jM}^{e}}\right) + \delta_{ij}\left(\frac{1}{D_{iM}^{e}} + \sum_{\substack{h=1\\ h\neq i}}^{n}\frac{x_h}{D_{ih}^{e}} - \frac{cRTB_0 x_i}{\eta W (D_{iM}^{e})^2}\right) \tag{15}$$

where, as usual, the Kronecker delta function

$$\delta_{ij=}\begin{cases} 0 & (j \neq i) \\ 1 & (j = i) \end{cases} \tag{16}$$

If desired, Eq. 14 may be formally inverted to yield an expression that is explicit in species flux

$$\mathbf{N}_i = -\frac{1}{RT}\sum_{j=1}^{n}\kappa_{ij}^{e} c_j \nabla_T \mu_j^{e} \qquad (i=1,2,\ldots,n) \tag{17}$$

where the effective Onsager diffusional coefficients κ_{ij}^{e} are the elements of the matrix $[H^e]^{-1}$, with elements of the effective frictional coefficient matrix $[H^e]$ being given by Eq. 15. The current density is then obtained from

$$\mathbf{i} = F\sum_{i=1}^{n} z_i \mathbf{N}_i \tag{18}$$

Proton Transport in Ionomeric Membranes.-We utilize the above general model of transport of charged species *i* in ionomeric membranes to the case of proton transport. Figure II-1 shows depicts the PEM as a “dusty fluid,” in which the polymer matrix along with the attached acid groups are viewed as “dust” particles comprising the PEM. It is visualized that an acid group HA (e.g., sulfonic acid groups in Nafion®) is tethered to each dust particle, which are distributed in a spatially uniform manner. Thus, the molecular weight of the dust species is equal to the PEM equivalent weight. In the absence of a polar solvent, the protons are firmly attached to the pendant acid groups $\tilde{\mathrm{A}}$ and, consequently, exhibit extremely low conductivity ($\sigma \approx 10^{-7}$ S/cm). In the presence of a proton acceptor solvent BH (e.g., HOH, CH_3OH, etc.), however, these acid groups are induced to dissociate as shown below:

$$\mathrm{HA} \rightleftarrows \mathrm{A}^{-} + \mathrm{H}^{+} \quad ; \quad K_{\mathrm{HA}} = \frac{a_{\mathrm{A}^{-}} a_{\mathrm{H}^{+}}}{a_{\mathrm{HA}}} \tag{19}$$

$$\mathrm{H}^{+} + \mathrm{BH} \rightleftarrows \mathrm{BH}_2^{+} \quad ; \quad K_{\mathrm{BH}_2^{+}} = \frac{a_{\mathrm{BH}} a_{\mathrm{H}^{+}}}{a_{\mathrm{BH}_2^{+}}} \tag{20}$$

so that the overall reaction representing protonation of the solvent by the pendant acid group HA is

$$\mathrm{HA} + \mathrm{BH} \rightleftarrows \mathrm{BH}_2^{+} + \mathrm{A}^{-} \quad ; \quad K_{\mathrm{A}} = \frac{K_{\mathrm{HA}}}{K_{\mathrm{BH}_2^{+}}} = \frac{a_{\mathrm{BH}_2^{+}} a_{\mathrm{A}^{-}}}{a_{\mathrm{HA}} a_{\mathrm{BH}}} \tag{21}$$

The solvated proton here is shown to be associated with a single solvent molecule, which is not likely to be true. In fact, the number of associated solvent molecules would likely vary with λ, the number of solvent molecules per acid site. For simplicity, however, the stoichiometry shown above is assumed here. In addition, it is assumed that each acid group gives up a single proton, which is the case for sulfonic acid groups, although there would be other groups, e.g., phosphonic acid, when the acid may donate more than one proton. It is further assumed that it is this protonated solvent species BH_2^{+} that serves as the major charge carrier much as in liquid electrolytes. Assuming local thermodynamic equilibrium, thus, the concentration of the proton carrier

$$c_{\mathrm{BH}_2^{+}} = c_{\mathrm{HA},0}\,\alpha \tag{22}$$

where $c_{\mathrm{HA},0}$ is the concentration of the pendant acid groups per unit volume of pore solution. The degree of dissociation, α, assuming ideal solution is obtained by solving

$$K_{\mathrm{A},C} \equiv \frac{c_{\mathrm{BH}_2^+} c_{\mathrm{A}^-}}{c_{\mathrm{HA}} c_{\mathrm{BH}}} = \frac{\alpha^2}{(1-\alpha)(\lambda-\alpha)} \tag{23}$$

where λ is the number of solvent molecules per acid site = $c_{\mathrm{BH},0} / c_{\mathrm{HA},0}$. The solution to Eq. 23 provides

$$\alpha = \frac{(\lambda+1) - \sqrt{(\lambda+1)^2 - 4\lambda(1-1/K_{\mathrm{A},C})}}{2(1-1/K_{\mathrm{A},C})} \tag{24}$$

Thus, the extent of dissociation depends upon $K_{\mathrm{A},C}$, i.e., on the relative proton affinities of A^- and BH, or in other words on the strength of the acid group (K_{HA}) and the nature of the solvent ($K_{\mathrm{BH}_2^+}$), as well as solvent uptake, λ. It is shown below that the acid dissociation is not complete, in general, even for superacidic membranes such as Nafion®.

Conductivity of Proton-Exchange Membranes.-For the case of a proton-exchange membrane consisting of water as the solvent, denoting water as species 2 and the protonated solvent, i.e., hydronium ion (H_3O^+) as species 1, Eq. 13, or equivalently Eq. 14, for this binary case (n = 2) reduces to

$$\mathbf{N}_1 = -\left(\frac{c}{RT}\right) \frac{x_1}{\dfrac{1}{D_{1M}^e} + \dfrac{1+(\nu-1)x_1}{D_{12}^e} - \dfrac{c x_1 B_0 RT}{\eta W D_{1M}^e}\left(\dfrac{1}{D_{1M}^e} - \dfrac{\nu}{D_{2M}^e}\right)} (\nabla_T \mu_1 + z_1 F \nabla \Phi) \tag{25}$$

where the flux ratio, $\nu \equiv -\mathbf{N}_2 / \mathbf{N}_1$, and from Eq. 12

$$W = 1 + \frac{c B_0 RT}{\eta}\left(\frac{x_1}{D_{1M}^e} + \frac{1-x_1}{D_{2M}^e}\right) \tag{26}$$

We shall restrict the following discussion to conductivity measurements in a closed conductivity cell, i.e., the case of equimolar counter-diffusion, so that $\nu = 1$. In the case of a fuel cell, of course, this would not hold, and then either ν would be specified by fuel cell reaction stoichiometry (e.g., ν = 3/2 for 2 hydronium ions diffusing to cathode to produce 1 water molecule plus releasing 2 water molecules that served as proton carriers) or it be appropriate to write another flux equation for species 2 (water) in terms of *its* chemical potential gradient. Due to the similarity in species 2 (water) and 1 (hydronium ion), it is further assumed here that $D_{1M}^{e} \approx D_{2M}^{e}$. Actually, this along with equimolar counter-diffusion is tantamount to the assumption that there is no convection (Eq. 11). Furthermore, the concentration gradient of hydronium ions (species 1) is zero owing to the assumption of spatial uniformity of the sulfonic acid groups coupled with electroneutrality.[40] This is further assumed to imply lack of chemical potential gradient for the hydronium ions, although due to the existence of a water concentration gradient, non-uniform proton activity coefficients, and hence non-zero chemical potential gradient through the membrane is possible. With the above assumptions, Eq. 25 reduces to the particularly simple form

$$\mathtt{N}_1 = -\left(\frac{1}{D_{1M}^{e}} + \frac{1}{D_{12}^{e}}\right)^{-1} \frac{F}{RT} c_1 z_1 \nabla\Phi \tag{27}$$

Further, from the use of this expression in Eq. 18, the current density

$$\mathtt{i} = -D_{12}^{e}\left(1 + \frac{D_{12}^{e}}{D_{1M}^{e}}\right)^{-1} \frac{F^2}{RT} c_1 z_1^2 \nabla\Phi \equiv -\sigma\nabla\Phi \tag{28}$$

assuming hydronium ions are the only charge carrying species. Furthermore, from the definition of conductivity in Eq. 28, $z_1 = +1$, and Eq. 22 for the concentration of the hydronium ions

$$\sigma = \frac{F^2}{RT} D_{12}^{e}\left(1 + \frac{D_{12}^{e}}{D_{1M}^{e}}\right)^{-1} c_{\mathrm{HA},0}\alpha \tag{29}$$

Finally, the use of Eq. 7 and defining $D_{12}^{e} / D_{1\,M}^{e} = \zeta_{1M}^{e} / \zeta_{12}^{e} = (K_1 / K_0)(D_{12} / D_{1M}) \equiv \delta$ results in

$$\sigma = \frac{F^2}{RT} (\varepsilon - \varepsilon_0)^q \left(\frac{D_{12}}{1+\delta}\right) c_{\mathrm{HA},0}\alpha \tag{30}$$

Alternatively, in terms of the equivalent conductance of hydronium ions in water, $\lambda_1^0 \equiv F^2 |z_1| D_{12}^0 / RT$,[31]

$$\sigma = (\varepsilon - \varepsilon_0)^q \left(\frac{\lambda_1^0}{1+\delta}\right) c_{\mathrm{HA},0}\alpha \tag{31}$$

Strictly, the numerator of Eq. (27) should include $\Gamma \equiv D_{12} / D_{12}^{0}$, the ratio of the diffusion coefficient of hydronium ion to that at infinite dilution. However, Γ is expected to be only slightly concentration dependent,[31] and is, consequently, assumed to be unity. The equivalent conductivity of hydronium ions, of course, is unusually high, i.e., $\lambda_1^0 = 349.8$ S.cm^2/equiv in water at 25°C, or $D_{12}^0 = 9.312 \times 10^{-5}$ cm^2/s,[31] and is explained in terms of the Grotthus diffusion mechanism in addition to the usual *en masse* diffusion.[47]

Some comments are also in order on the magnitude of δ. In addition to structural effects represented by K_1/K_0, which depends upon ε or RH, δ depends upon the ratio D_{12}/D_{1M}, which in turn depends upon the difference in collision frequencies of species 1 and 2 and that of 1 and M, as well as the molecular weights of species 2 and M.[48] The difference in collision frequencies in turn depend upon the size difference between species 2 and M. Thus, the ratio D_{12}/D_{1M} is expected to be >1. On the other hand, the ratio K_1/K_0 would be expected to have inverse dependence on ε or λ, being large at low water loading and reducing at higher loadings. Thus, δ would be a relatively large number at low water loadings and would reduce as ε increases, when a diffusing hydronium ion would encounter a water molecule more frequently than it would encounter the polymer matrix. Unfortunately, it is difficult to be more quantitative at this stage. Thus, δ is treated as a fitted parameter here, with its value depending upon the level of hydration.

Membrane Hydration and Swelling.-The equivalent weight (EW) of the membrane (g dry polymer/mol acid groups) and the partial molar volume of the membrane are interrelated

$$\bar{V}_M \approx \frac{\mathrm{EW}}{\rho_0} \tag{32}$$

where ρ_0 is density of the dry membrane. For Nafion® 117, 115, or 112, membranes of interest here, the EW = 1100, and ρ_0 = 2.05 g/cm.[3,37] Thus, $\bar{V}_M = 537$ cm^3/mol. The other properties of Nafion® required for the use in Eq. 31 include acid group concentration, defined on the basis of per unit volume of pore solution

$$c_{\mathrm{HA},0} = \frac{1}{\lambda \bar{V}_2} \tag{33}$$

where $\bar{V}_2$ is the partial molar volume of water, roughly 18 cm^3/mol. The volume fraction of water in swollen Nafion® corresponding to a water loading λ

$$\varepsilon = \frac{\lambda}{\frac{\bar{V}_M}{\bar{V}_2} + \lambda} \tag{34}$$

In addition, a relationship is needed for correlating the water uptake to RH. Recently, Futerko and Hsing[49] utilized a modified version of the Flory-Huggins model for this. Springer *et al*.,[38] and Hinatsu *et al*.,[50] on the other hand, simply used a 3rd order polynomial to empirically fit λ versus water vapor activity, a_2. We find, however, that the water sorption characteristics of Nafion® can be well-modeled by an n_2-layer Brunauer-Emmett-Teller (BET) equation[51] with physically meaningful parameters, and is hence adopted here

$$\frac{\lambda}{\lambda_m} = \frac{[Ca_2/(1-a_2)][1-(n_2+1)a_2^{n_2} + n_2 a_2^{n_2+1}]}{1+(C-1)a_2 - Ca_2^{n_2+1}} \tag{35}$$

where the RH or the water vapor activity, $a_2 = p_2 / p_2^o$, λ_m is the water loading at monolayer coverage, and n_2 is the total number of water layers in the pores at saturation, which is roughly equal to the maximum number of water molecules per sulfonate divided by λ_m, i.e., $n_2 \approx \lambda_{\mathrm{sat}} / \lambda_m$ for parallel plate pore geometry.

Results and Discussion

Water Uptake by Nafion®.- The conductivity of Nafion® and other proton-exchange membranes is highly dependent upon their water content, the highest conductivity, σ_{sat}, corresponding to water-equilibrated membranes, which have the highest water uptake, λ_{sat}, for a given imbibition temperature and membrane pretreatment procedure.[50] It is useful to recall that three different Nafion® pretreatment protocols have been described in the literature:[52] 1) boiling the membrane in water, which results in the so-called E (expanded)-form; 2) drying at 80ºC, which produces N (normal) form; and 3) drying at 105ºC, which produces the S (shrunken) form. Hinatsu *et al*.[50] report that the E-form of Nafion®117 absorbs more water ($\lambda_{\mathrm{sat}}^{\mathrm{liq}}$= 23, at 25ºC) than the N− or S− forms, which absorb $\lambda_{\text{sat}}^{\text{liq}} = 13.5$ and $\lambda_{\text{sat}}^{\text{liq}} = 11$, respectively, at 25ºC. However, this increases with the temperature of immersion, except for the E-form membranes, for which it remains independent of temperature. Drying of the membranes at elevated temperatures apparently results in pore shrinkage due to polymer creep, which can be reversed only by exposure to water at elevated temperatures.

Curiously, the water uptake in membranes equilibrated with saturated water vapor at otherwise identical conditions is significantly lower than in those immersed in water. Thus, Zawodzinski *et al.*[53] observed that at 30ºC the water content of Nafion®117 equilibrated with liquid water, $\lambda_{\text{sat}}^{\text{liq}} \approx 22$, while for membrane equilibrated with saturated water vapor, $\lambda_{\text{sat}}^{\text{vap}} \approx 14$. Further, when liquid water equilibrated membrane was removed and suspended over saturated water vapor, λ_{sat} dropped from 22 to 14, indicating that the two states are thermodynamically stable. This phenomenon, sometimes known as Schroeder's paradox, is apparently not uncommon in polymer systems, and is discussed briefly by Zawodzinski *et al.*[53]

Figure II-2 shows the equilibrium sorption from water vapor on Nafion®117 as a function of water vapor activity, or RH, taken from the experimental data of Zawodzinski *et al.*[52] at 30ºC as well as those of Morris and Sun[37] at 25ºC. These data are also similar to those reported by Pushpa *et al.*,[54] although the data of Hinatsu *et al.*[50] at the higher temperature of 80ºC are somewhat different. Although there is some scatter in Fig. 2, it can be seen that Eq. (35) represents the data well with physically realistic values of parameters ($\lambda_m = 1.8$, $n_2 = 13.5$, $C = 150$) as listed in Table II-1. The monolayer coverage λ_m was estimated from knowledge of the specific pore surface area S and by using

$$\lambda_m = \left(\frac{S}{\rho_0}\right)\frac{\text{EW}}{N_A A_2} \tag{36}$$

where the surface area occupied by an adsorbate molecule on the pore surface was estimated from[55]

$$A_2 = 1.091\left(\frac{MW_2}{\rho_2 N_A}\right)^{\frac{2}{3}} \tag{37}$$

For Nafion® 117, S = 210 (m^2/cm^3),[56] and these expressions provide λ_m= 1.8, which was adopted here. However, as indicated in Table II-1, C and n_2 were used simply as fitted parameters, but their values utilized are not entirely unreasonable. Thus, $n_2 \times \lambda_m \approx 24$, which is certainly more than $\lambda_{\text{sat}}^{\text{vap}} \approx 14$, but is of the order of $\lambda_{\text{sat}}^{\text{liq}}$. The parameter C, generally >> 1, represents the ratio of the adsorption equilibrium constant of the first layer to that of the subsequent layers

$$C = m \exp\left(\frac{Q_1 - Q_L}{RT}\right) \tag{38}$$

where Q_1 is the enthalpy of adsorption of first layer, while Q_L is that of the succeeding layers, usually assumed to be constant and equal to the latent heat of condensation of the adsorbate. Thus, assuming m = 1, the C = 150 implies a $(Q_1 - Q_L) \approx 12$ kJ/mol, i.e., at 25ºC, $Q_1 \approx 56$ kJ/mol. In comparison, Escoubes and Pineri,[57] based on microcalorimetric studies, found the heat of adsorption of water vapor in Nafion® to vary from 16.7 to 52.3 kJ/mol, the higher values corresponding to lower water uptake ($\lambda < 4$). Of course, the assumption of the heat of adsorption of second and higher layers being equal to the heat of condensation (≈ 44 kJ/mol at 25ºC for water) may not be true in Nafion® due to the strongly hydrophobic nature of the polymer backbone. At any rate, for $(Q_1 - Q_L) \approx$ constant, Eq. (38) shows that C would decline with temperature, which appears to be consistent with the adsorption isotherms measured at higher temperatures,[50] having a more rounded "knee" at low RHs. Of course, one would also expect n_2 to vary with temperature and the membrane pretreatment procedure. It appears, in short, that the finite-layers BET adsorption isotherm, with C and n_2 dependent upon temperature and pretreatment procedure, is a suitable representation of adsorption on Nafion®.

Finally, it is noteworthy from Fig. 2 that there is a relatively small change in λ over a rather broad range of RH, i.e., from about 10 to 70%. At higher RH, however, the increase in λ is more pronounced, particularly as saturation is approached. This has important implications in the range of RHs required for effective conduction and fuel cell performance, where it is found that there is a precipitous decline in performance at RH substantially less than 100%. This point is further discussed later on.

Conductivity in Liquid Water-Equilibrated Membrane.-Since the water content of the membranes immersed in liquid water is quite different from that in those equilibrated with saturated water vapor, the conductivities observed in the two different cases are also significantly different.[53] Therefore, conductivity of liquid water equilibrated Nafion®115 was determined experimentally using the AC impedance method over the temperature range from 25ºC to 100ºC. Conductivity in the longitudinal (XY) plane was measured using a pair of pressure-attached, high surface platinum electrodes. The mounted sample was immersed in deionized and distilled water at a given temperature and equilibrated for 30 minutes. The conductivity measurements were made with a perturbation voltage of 10 mV in the frequency range from 0.01 Hz to 2.0 x 10^7 Hz using a Solartron SI 1260 Frequency Response Analyzer. Both real and imaginary components of the impedance were measured and the real Z-axis intercept was closely approximated. The cell constant was calculated from the spacing of the electrodes and the membrane cross-sectional area, i.e., the thickness and the width of the membrane. The experimental results of σ versus inverse temperature are shown in Fig. 3 along with theoretical predictions for the parameters listed in Table II-1.

The agreement between theory and experiments in Fig. 3 is seen to be good, particularly in view of the fact that $\delta_{\mathrm{sat}}^{\mathrm{liq}}$ = 0.6 was the only fitted parameter employed, all other parameters being adopted from the literature (Table II-1) and BET constants determined independently as described above. Thus, $\lambda_{\mathrm{sat}}^{\mathrm{liq}} = 23$ is reported by Hinatsu *et al.*,[50] $\lambda_0 = 1.9$ is given by Morris and Sun[37] (which is also physically realistic in view of $\lambda_m = 1.8$ calculated above), q = 1.5 is given by Gierke and Hsu,[15] as well as by Newman,[31] and others,[32] although Morris and Sun[37] propose $q = 1.9$.

The temperature dependence of equivalent conductance is assumed to be given by

$$\lambda_i^0 = \lambda_{i,298}^0 \exp\left[-\frac{E_\eta}{R}\left(\frac{1}{T}-\frac{1}{298}\right)\right] \tag{39}$$

which results from $\lambda_i^0 \eta \approx$ constant and Arrhenius temperature dependence of viscosity. Consequently, $E_\eta \approx$ 14 kJ/mol, the activation energy for viscosity of water in the temperature range of interest, is assumed here, along with $\lambda_{1,298}^0 = 349.8$ S.cm^2/equiv for protons in aqueous solvents.[31] This value of activation energy adopted is justified in view of the following, even though there is a large variation in activation energies for σ reported in literature, i.e., from 2 kJ/mol to 16 kJ/mol.[4,35,52] For ordinary liquid-phase diffusion, the relation $\lambda_i^0 \eta \approx$ constant stems directly from the well-known relation $D_i \eta / T \approx$ constant,[31] along with the relation between equivalent conductance and diffusivity, $\lambda_i^0 \equiv F^2 |z_i| D_i^0 / RT$. However, it is well known that for the case of hydronium ions, ordinary diffusion is supplemented with Grotthus hopping.[47] It turns out, nonetheless, that the activation energy for Grotthus conduction is also of the same order (14 - 40 kJ/mol),[35] so that $E_\eta = 14$ kJ/mol seems to be a reasonable estimate.

As shown below, however, the temperature dependency of conductivity is also affected by the degree of acid group dissociation, α, which varies with temperature owing to the temperature dependence of the acid dissociation constant

$$K_{\mathrm{A,C}} = K_{\mathrm{A,C,298}} \exp\left[-\frac{\Delta H^o}{R} \left(\frac{1}{T} - \frac{1}{298} \right) \right] \tag{40}$$

which is based on the assumption that the heat of solvation, $\Delta H^o \approx$ constant. Unfortunately, however, the $K_{\mathrm{A,C,298}}$ value for Nafion® is not available in the literature, although the study of Twardowski *et al.*,[58] indicates a $\mathrm{pK}_a < 1$, suggesting strong acidity. Further, the Hammett acidity function of Nafion® is reportedly similar to that for 100% sulfuric acid.[59] Consequently, it was decided to use the thermodynamics of the liquid solvation reaction

$$\mathrm{H_2SO_4 + H_2O \Leftrightarrow H_3O^+ + HSO_4^-} \tag{41}$$

to simulate that of the sulfonic acid groups in Nafion®. For $\mathrm{H_2SO_4}$, the reported $K_{\mathrm{A,C,298}}$ values range from 1.2 to 50.[60] Based on the data of Vinik and Zarakhani,[61] thus, $K_{\mathrm{A,C,298}} = 6.2$ was adopted for Nafion®. Further, it may be recalled that the study of Escoubes and Pineri[57] found the heat of adsorption of water vapor in Nafion® to be 52.3 kJ/mol at $\lambda < 4$. Consequently, $\Delta H^o = -52.3$ kJ/mol in Eq. 40 was adopted. With the above parameters thus chosen from the literature, a choice of $\delta = 0.6$ provides a good fit between the theoretical model and the experimental data as shown in Fig. 3. Particularly noteworthy is that the model captures the decrease in slope, or the effective activation energy, at higher temperatures. This is due to incomplete acid dissociation at the higher temperatures as discussed below, and may account for some of the discrepancy in activation energies reported in the literature. Interestingly, as a result of this, the theoretical model predicts a maximum in conductivity at higher temperatures, which needs to be experimentally confirmed.

It is of interest to investigate, assuming of course that the acid dissociation constant adopted above is reasonable, whether the sulfonic acid groups are completely dissociated, as usually assumed, under different conditions of water uptake and temperature. Thus, using Eq. (40) in (24), the degree of dissociation is plotted in Fig. 4 versus λ at different temperatures. It is noteworthy that even at low temperatures, the dissociation is not complete for $\lambda < 10$. Further, as expected for an exothermic reaction, the dissociation at higher temperatures typical of PEM fuel cells is incomplete even under saturation conditions. At higher temperatures, thus, higher water contents are required for adequate dissociation. These considerations are clearly of practical significance in view of current efforts to develop higher temperature proton-exchange membranes.[62]

Conductivity in Water Vapor-Equilibrated Nafion®.-A predictive model for the dramatic effect of RH on the conductivity of Nafion® is, of course, crucial in studying and optimizing the fuel cell performance. Figure II-5 compares the model developed here with the data of Sone *et al.*[35] for conductivity of Nafion®117 versus RH for water vapor equilibrated membrane at three different temperatures. The agreement is seen to be very good over 2 orders of magnitude, providing confidence in the soundness of the theoretical approach. Further, the model predicts the effect of temperature on σ adequately in this range. It is noteworthy that the parameter values determined as described above and listed in Table II-1 remain unchanged, except for δ, which takes on a value of 5.5 for water vapor equilibrated Nafion®. It may be recalled from a discussion of this parameter that it would be expected to increase as the water content of the membrane declines. It turns out, however, that a single value of for $\delta = 5.5$ is adequate for fitting the data over the entire range of RHs. As expected, its value is greater than that for the case of liquid water equilibrated membrane. Although it is not yet possible to determine if this value of δ is reasonable, it compares well to the value of $\delta = 3.7$ for the case of Na^+ cation transport through the membrane, used by van der Stegen[33] as a fitted parameter. Finally, it is clear from this figure that RH has a very pronounced effect on the membrane conductivity, and explains the precipitous drop in fuel cell performance at lower RHs.[62]

Effect of Temperature on Conductivity of Vapor-Equilibrated Nafion®.-The conductivity of Nafion® is strongly dependent upon temperature for a given partial pressure of water. This aspect is important due to the current efforts to develop higher temperatures (≥ 120ºC) PEM fuel cells that operate at or around ambient pressure,[61] which would clearly require membranes that perform adequately at lower RHs. Such is not the case, of course, for conventional PFSAs such as Nafion®. Thus, Fig. 6 shows the data of Sumner *et al*.[34] for the conductivity of Nafion®117 as a function of temperature at a fixed partial pressure of water (2.0×10^4 Pa, i.e., a humidifier temperature of 60ºC) along with the model predictions based on the parameters listed in Table II-1, with no additional fitted parameters employed. It may be gleaned from this figure that if the temperature of a fuel cell operating at 60ºC were raised, for instance, to around 100ºC, with the humidifier temperature remaining at 60 ºC, its performance would drop hopelessly corresponding to a decline in membrane conductivity of about two orders of magnitude. Malhotra and Datta[62] found this indeed to be the case, which is a major impediment in the development of higher temperature ambient pressure fuel cells based on conventional PEMs.

Conclusions

A predictive transport model is proposed here for the conductivity of proton-exchange membranes based on the dusty-fluid model founded on the generalized Stefan-Maxwell equations and including diffusion and convection, the latter resulting from a pressure and/or potential gradients. The theoretical model also incorporates thermodynamic equilibrium analysis for dissociation of the pendant acid groups in the presence of polar solvents such as water. Further, the physicochemical characteristics of the membrane are included, as is a finite-layers BET model for the sorption isotherm of the solvent by the membrane from vapor phase. The result is a robust model that is able to provide reliable predictions for the membrane conductivity under a variety of conditions of relative humidity and temperature, as well as for water-equilibrated membranes. All the parameters employed in the calculations were obtained from the literature, with only the BET parameters C and n_2, as well as δ, the ratio of diffusion coefficients representing interaction of the hydronium ion with water and that with the membrane, employed as fitted parameters. Further, these fitted parameters have values that appear justifiable. The described model should be useful in predicting and optimizing the performance of PEM fuel cells.

Acknowledgement

The financial support for this work provided by the H Power Corp. under Naval Surface Warfare Center (NSWC) Contract No. N00167-99-C-0002 is gratefully acknowledged.

References

0 W. Grot, in *Encyclopedia of Polymer Science and Engineering*, **16**, 2nd. ed. (1989).

1 T. D. Gierke, G. E.. Munn and F. C.Wilson, *J. Polym. Sci., Polym. Phys. Ed.* **19,** 1687 **(**1981).

2 S. W. Yeo and A. Eisenberg, *J. of Applied Polymer Science*, **21**, 875 (1977).

3 J. Halim, F. N. Buchi, O. Haas, M. Stamm and G. G. Scherer, *Electrochimica Acta*, **39**, 8/9 (1994).

4 B. Rodmacq, J. M. D. Coey, M. Escoubes, E. Roche, R. Duplessix, A. Eisenberg and M. Pineri, in *Water in Polymers*, S. P. Rowland, Editor, Chapter 29, ACS Symposium Series **127**, ACS (1980).

5 H. L. Yeager and A. Steck,, *J Electrochem Soc*., **128**, 1880 (1981).

6 K. A. Mauritz, C. J. Hora, A. J. Hopfinger, in *Ions in Polymers,* A. Eisenberg, Editor, Chapter 8, Advanced Chemistry Series **187**, American Chemical Society, Washington, DC (1980).

7 S. R. Lowry and K. A. Mauritz, *J.Am. Chem. Soc*., **102**, 4665 (1980).

8 T. D. Gierke, *J Electrochem. Soc***.**, **124**, 319(C) (1977).

9 W. Y. Hsu, J. R. Barley and P. Meakin, *Macromolecules*, **13,** 198, (1980).

10 V. K. Dayte, P. L. Taylor and A. J. Hopfinger, *Macromolecules*, **17,** 1704 (1984).

11 K. A. Mauritz and C. E. Rogers, *Macromolecules*, **18,** 483 (1985).

12 P. Aldebert, B. Dreyfus, G. Gebel, N. Nakamura, M. Pineri and F. Volino, *J. Phys. France*, **49**, 2101 (1988).

13 M. Falk, *Can. J. Chem.* **58**, 1495 (1980).

14 T.D. Gierke and W.Y. Hsu, *Perfluorinated Ionomer Membrane,* A. Eisenberg and H. L. Yeager, Editors, American Chemical Society, Washington, DC (1982).

15 W. Y. Hsu and T. D. Gierke, *Macromolecules*, **15**, 101 (1982).

16 F. Helfferich, *Ion Exchange*, McGraw-Hill, New York (1960).

17 N. Lakshminarayanaiah, *Transport Phenomena in Membranes*, Academic Press, New York (1969).

18 E. Riande, in *Physics of Electrolytes*, Vol. 1, J. Hladik, Editor, p. 401, Academic Press, New York (1972).

19 P. Meares, J. F. Thain, and D. G. Dawson, in *Membranes. A Series of Advances*, G. Eisenman, Editor, p. 55, Marcel Dekker, New York (1972).

20 O. Kedem and A. Katchalsky, *Trans. Faraday Soc.,* **59,** 1918 (1963).

21 A. Katchalsky and P. F. Curran, *Nonequilibrium Thermodynamics in Biophysics*, Harvard University Press, Cambridge (1965).

22 M. Verbrugge, and R. Hill, *J. Electrochem. Soc.*, **137**, 886 (1990).

23 E. H. Cwirko and R. G. Carbonell, *J. Membrane Sci.,* **67**, p. 227 (1992).

24 M. A. Scattergood and E. N. Lightfoot, *Trans. Faraday Soc.*, **64**, 1135 (1968).

25 E. N. Lightfoot, *Transport Phenomena and Living Systems*, Wiley, New York (1974).

26 P. N. Pintauro and D. N. Bennion, *Ind. Eng. Chem., Fundam.*, **23**, 230 (1984).

27 K. S. Spiegler, *Trans. Faraday Soc.*, **54**, 1408 (1958).

28 A. G. Guzmán-Garcia, P. N. Pintauro, M. W. Verbrugge and R. Hill, *AIChE Journal*, **36,** 1061, (1990).

29 P. Pintauro and Y. Yang, in *Tutorials In Electrochemical Engineering- Mathematical Modeling,* R. F. Savinell, J. M. Fenton, A. West, S. L. Scanlon, J. Weidner, Editors, PV 99-14 p.178 The Electrochemical Society Proceeding Series, Pennington , NJ (1999).

30 J. S. Newman, *Electrochemical Systems*, 2nd ed., pp. 255, 299, 461, Prentice Hall, Englewoods Cliffs, NJ (1991).

31 J. A. Wesseling, P. Vonk, G. Kraaijeveld, *Chem. Eng. J.*, **57**, 75, (1995).

32 J. H. G. van der Stegen, A. J. van der Veen, H. Weerdenburg, J.A. Hogendoorn and G.F. Versteeg, *Chem. Eng. Sci.,* **54,** 2501 (1999).

33 J. J. Sumner, S. E. Creager, J. J. Ma, and D. D. DesMarteau, *J. Electrochem. Soc.*, **145**, 107 (1998).

34 Y. Sone, P. Ekdunge and D. Simonsson, *J. Electrochem. Soc.*, **143**, 1254 (1996).

35 C. S. Fadley and R. A. Wallace, *J. Electrochem. Soc.*, **115**, 1264 (1968).

36 D. Morris and X. Sun, *J. Applied Polymer Science*, **50,** 1445 (1993).

37 T. E. Springer, T. A. Zawodzinski, S. Gottesfeld, *J. Electrochem. Soc.*, **136**, 2334 (1991).

38 M Eikerling, A. A. Kornyshev, and U. Stimming, *J. Phys. Chem. B***, 101** 1997.

39 D. M. Bernardi and M. W. Verbrugge, *AIChE J.*, **37**, 1151 (1991).

40 S. J. Paddison., R. Paul, and T. A. Zawodzinski Jr., *J. Electrochem. Soc.*, **147**, 617 (2000).

41 X.-D. Din and E. E. Michaelides, *AIChE J.*, **44**, 35 (1998).

42 E. A. Mason and A. P. Malinauskas, *Gas Transport in Porous Media: The Dusty-Gas Model*, p. 142, Elsevier, Amsterdam (1983).

43 A. Eisenberg, and J. S. Kim, *Introduction to Ionomers*, Wiley-Interscience, (1998).

44 R. Jackson, *Transport in Porous Catalysts*, Elsevier, Amsterdam (1977).

45 R. Datta, and V. R. Kotamarthi, *AIChE J.*, **36**, 916, (1990).

46 T. A. Zawodzinski, M. Neeman, L. O. Sillerud, and S. Gottesfeld, *J. Phys. Chem.*, **95**, 6040 (1991).

47 F. A. Williams, *Am. J. Phys.,* **26**, 467 (1958).

48 P. Futerko and I.-M. Hsing, *J. Electrochem. Soc.*, **146**, 2049 (1999).

49 J. T. Hinatsu, M. Mizuhata, and H. Takenaka, *J. Electrochem. Soc.*, **141**, 1493 (1994).

50 A. W. Adamson and A. P. Gast, *Physical Chemistry of Surfaces*, 6th ed., p.622, Wiley Interscience, New York (1997).

51 R. S. Yeo and H. L. Yeager, in *Modern Aspects of Electrochemistry*, No. 16, B. E. Conway, R. E. White, and J.O'M. Bockris, Editors, p. 437, Plenum Press, New York (1985).

52 T. A. Zawodzinski, C. Derouin, S. Radzinski, R. J. Sherman, V. T. Smith, T. E. Springer and S. Gottesfeld, *J. Electrochem. Soc.*, **140**, 1041 (1993).

53 K. K. Pushpa, D. Nandan, and R. M. Iyer, *J. Chem. Soc., Faraday Trans. I*, **84**(6), 2047 (1988).

54 J. J. F. Scholten, *Studies in Surface Science and Catalysis*, 79, (1993).

55 J. Divisek, M. Eikerling, V. Mazin, H. Schmitz, U. Stimming and Yu. M. Volfkovich, *J. Electrochem. Soc.,* **145**, 2677 (1998).

56 M. Escoubes and M. Pineri, in *Perfluorinated Ionomer Membranes*, A. Eisenberg and H. L. Yeager, Eds. ACS Symposium Series No. 180, p. 9, American Chemical Society, Washington, DC (1982).

57 Z. Twardowski, H. L. Yeager, and B. O'Dell, *J. Electrochem. Soc.*, **129**, 328 (1982).

58 M. Misono and T. Okuhara, *Chemtech.*, 23, November, (1993).

59 M. Liler, *Reaction Mechanisms in Sulphuric Acid,* Academic Press, New York (1971).

60 M. I. Vinnik and N. G. Zarakhani, *Dokl. Akad. Nauk SSSR,* **152**, 1147 (1963).

61 S. Malhotra and R. Datta, *J. Electrochem. Soc*., **144**, L23-L26, (1997).

Table II-1. Parameter Values Employed in Model for Nafion® Membrane

Parameter	Value	Units	Comments/Reference
EW	1100	g/equiv.	Morris and Sun[37]
ρ_0	2.05	g/cm^3	Morris and Sun[37]
S	210	m^2/cm^3	Divisek *et al.*[56]
λ_m	1.8		Calculated from Eq. (36) and *S*
C	150		Fitted for BET adsorption isotherm, Fig. 2
n_2	13.5		Fitted for BET adsorption isotherm, Fig. 2
λ_0	1.9		Morris and Sun[37]
q	1.5		Gierke and Hsu[15]; Newman[31] p. 461
$\lambda_{\mathrm{sat}}^{\mathrm{liq}}$	23		Hinatsu *et al.*[50]
$K_{\mathrm{A,C,298}}$	6.2		Vinik and Zarakhani[61]
ΔH^{o}	–52.3	kJ/mol	Escoubes and Pineri[57]
E_η	14	kJ/mol	Activation energy for viscosity of water
$\lambda_{1,298}^{0}$	349.8	S.cm^2/equiv.	Newman,[31] p. 255
$\delta_{\mathrm{sat}}^{\mathrm{liq}}$	0.6		Fitted for liquid-equilibrated conductivity
$\delta_{\mathrm{sat}}^{\mathrm{vap}}$	5.5		Fitted for vapor-equilibrated conductivity

AH = Acid Group; BH = Solvent; ⊕ = H^+

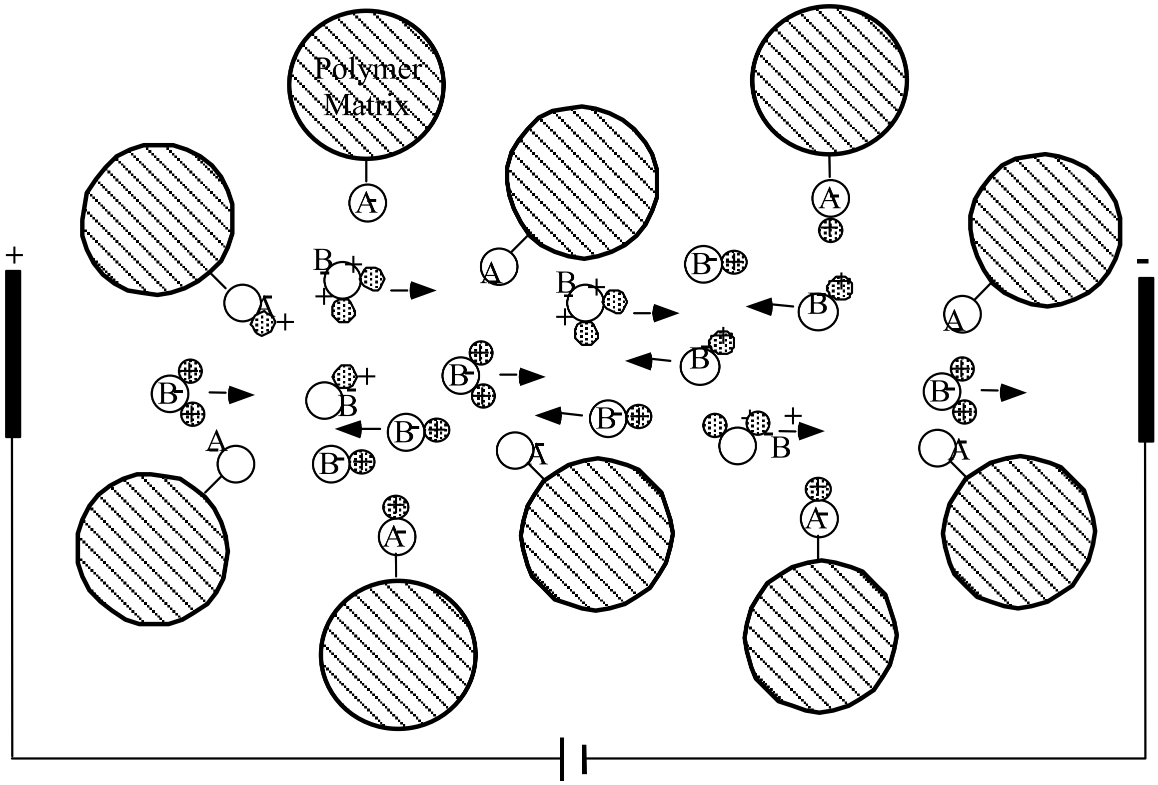

Figure II-1. A “dusty fluid model” depiction a proton-exchange membrane (PEM). The polymer matrix along with an acid groups are viewed as “dust” particles comprising the PEM. The membrane imbibes a polar solvent BH (e.g., HOH, CH_3OH), that solvates the protons from the pendant acid HA forming BH_2^+ that serves as the charge carrier.

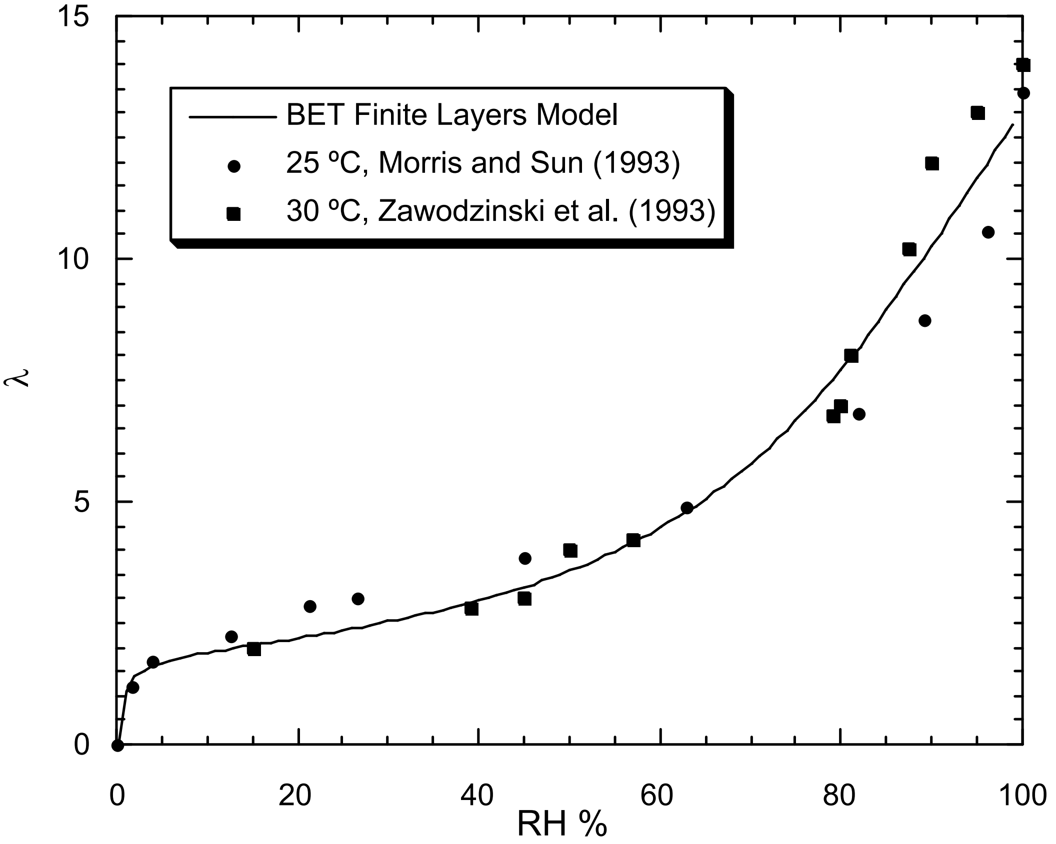

Figure II-2. Adsorption isotherm for water uptake by Nafion®117 from water vapor. The finite layers BET isotherm is compared with the data of Zawodzinski *et al.*[53] at 30ºC and that of Morris and Sun[37] at 25ºC for parameters listed in Table II-1.

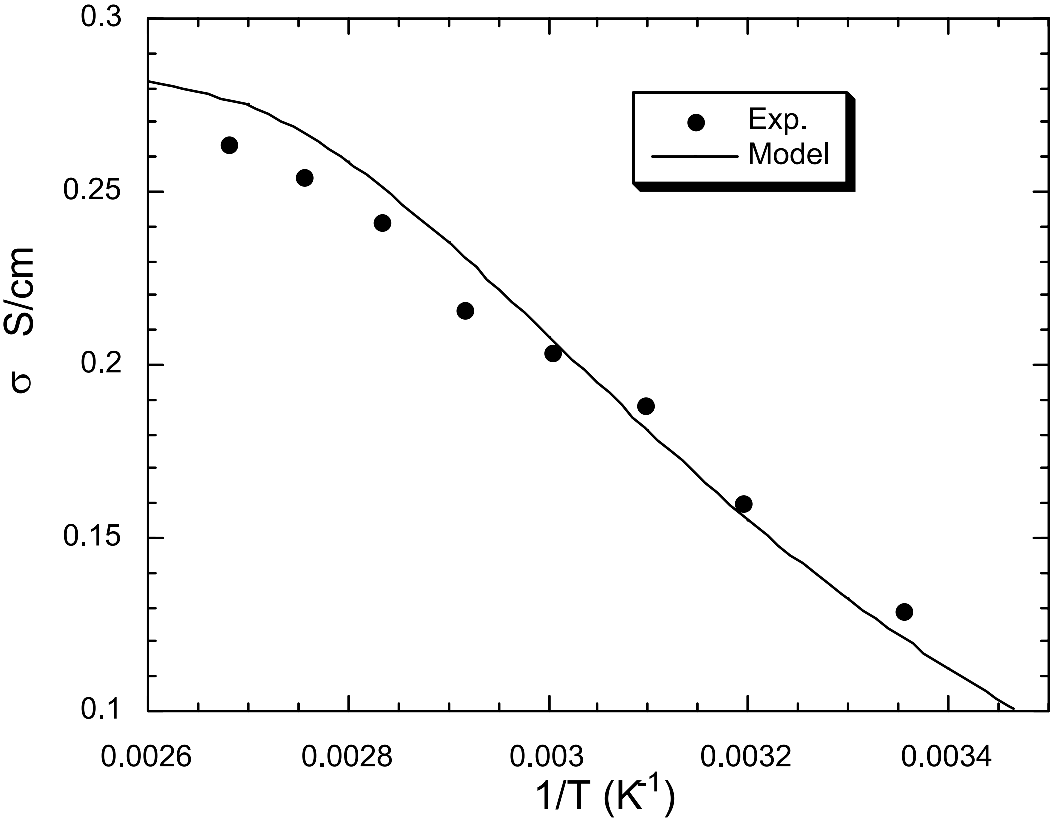

Figure II-3. Experimental σ_{max} for Nafion®115 immersed in liquid water versus inverse temperature along with theoretical predictions for parameters listed in Table II-1.

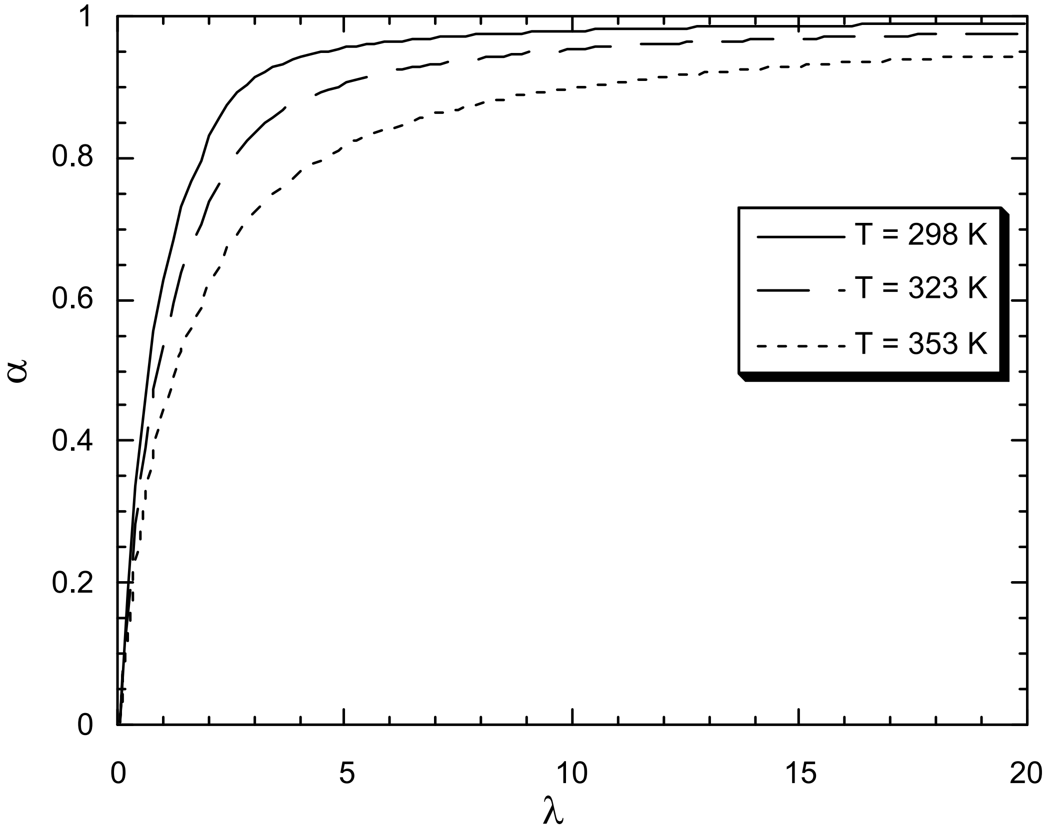

Figure II-4. Predicted equilibrium fractional dissociation of sulfonic acid groups in Nafion® as a function of the water uptake at different temperatures.

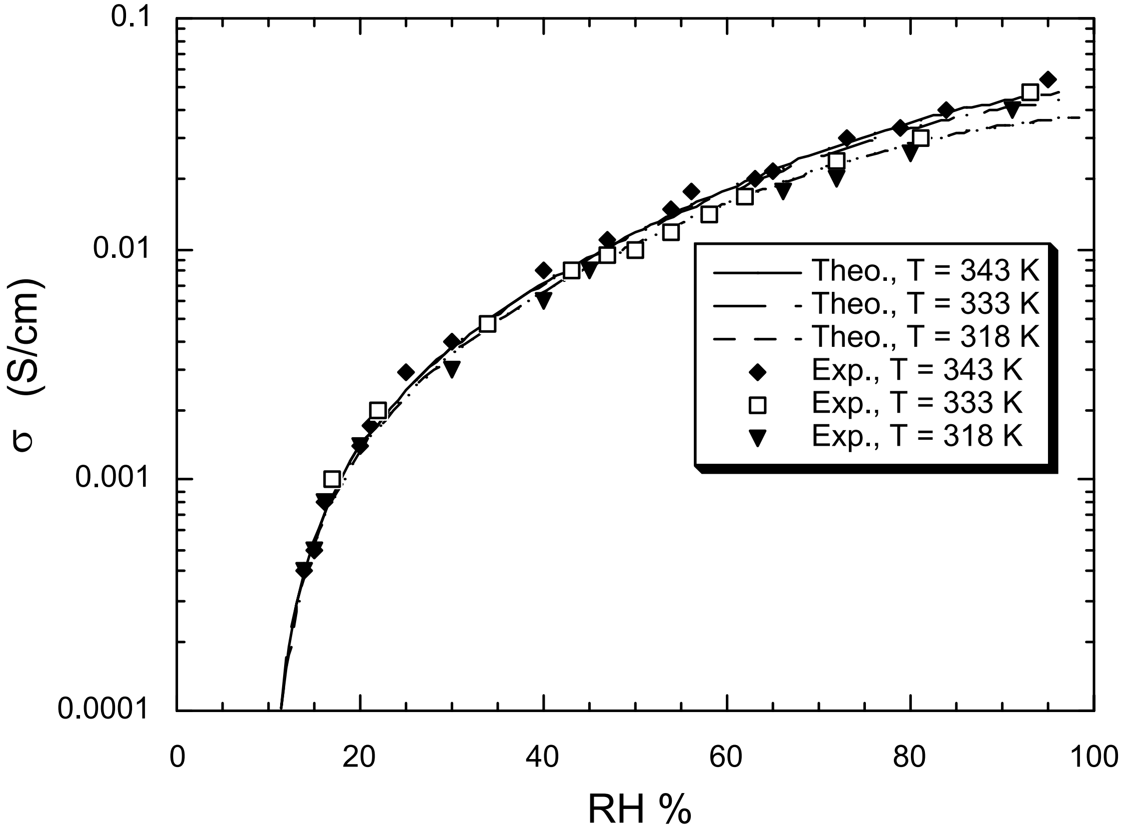

Figure II-5. The experimental results of Sone *et al.*[35] for σ of Nafion® 117 equilibrated in water vapor versus RH or water vapor activity at different temperatures along with theoretical predictions for parameters listed in Table II-1.

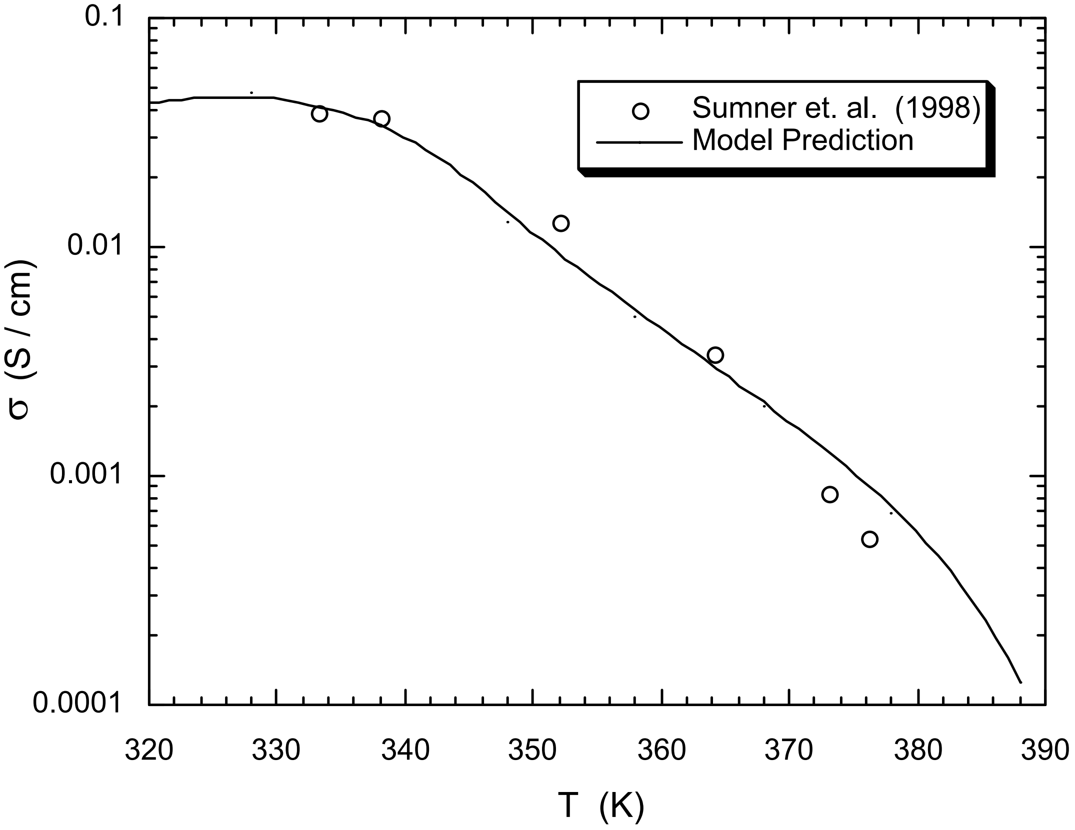

Figure II-6. Effect of temperature on conductivity of Nafion®117 at a fixed partial pressure of water (2.0 x 10^4 Pa, i.e., humidifier temperature = 333K). The data of Sumner *et al.*[34] are plotted along with model predictions for parameters listed in Table II-1.

III. PEM FUEL CELL AS A MEMBRANE REACTOR[#,‡]

Abstract

The H_2-O_2 proton exchange membrane (PEM) fuel cell, among numerous other potential applications now slated to provide the motive power for the next generation of highly efficient and largely pollution-free automobiles, is an incomparable membrane reactor, comprising an exquisitely designed membrane-electrode-assembly (MEA), a five-layer composite of two gas-diffusion layers, two supported-catalyst layers, and a proton-exchange membrane. The device allows catalytic reaction and separation of hydrogen and oxygen as well as protons and electrons. This paper describes the structure and performance of the PEM fuel cell considered as a membrane reactor and develops an analytical transport-reaction model that, despite some assumptions, captures the essential features of the device very well. The key assumptions are that transport resistance as well as ohmic drop are negligible in the catalyst layer. While the latter is defensible, the former causes deviations at high current densities. Nonetheless, the model predicts the fuel cell performance well with parameter values reported in the literature.

[#] Paper presented at ICCMR-2000, Zaragoza, Spain and published in *Catalysis Today*, **67** (2001) 15.

[‡] The Contributions of S. Malhotra, J. Zhang, and R. Datta are gratefully acknowledged.

Introduction

Fuel cells offer the potential of revolutionizing electrical energy production by affording highly efficient and largely pollution-free power generation systems for both transportation and stationary applications[1,2]. Proton-exchange membrane (PEM) fuel cells[3], operating on H_2 and O_2 (from air), are the focus at this time, although other fuel cells, namely, molten carbonate fuel cells (MCFCs), solid-oxide fuel cells (SOFCs) and direct methanol fuel cells (DMFCs) also hold promise for various applications[4,5]. The PEM fuel cell is particularly attractive because of mild operating conditions (50 - 80 ºC temperature, 1 - 3 atm. pressure), low Pt loadings, relative robustness, long life, and the fact that all of its components are solid. It comprises an intricate membrane-electrode-assembly (MEA), a five-layer composite of two gas-diffusion layers that allow simultaneous transport of gases and water while collecting current, two three-phase supported-catalyst (typically Pt/C) layers, and a proton-exchange membrane, typically a perfluorosulfonic acid (PFSA) polymer such as Nafion®. It is, in fact, a superb example of a catalytic membrane reactor performing a variety of reactions and separations. The MEA nanostructure has evolved over a considerable period of time to now provide exceptional performance. Thus, many of the fabrication issues for attaining superior performance have been resolved. However, before wide-spread usage of PEM fuel cells becomes a reality, there still are a number of technical/cost challenges that remain to be addressed.

A key limitation is that the proton conductivity of the PEM is strongly dependent upon its water content, calling for elaborate water management and limiting the practical operating temperature to 80 ºC to avoid membrane drying[6]. At these low operating temperatures, however, the Pt anode is particularly susceptible to poisoning by even traces of CO in the anode H_2 feed[7]. However, since the storage and transportation of H_2 fuel at this time is impractical, conventional hydrocarbon or alcohol fuels must be locally reformed into a H_2 rich reformate gas that cannot be completely rid of CO. These catalytic processes, while well-developed for the industrial scale, have special requirements for fuel cell applications, thus offering innumerable challenges and opportunities in catalysis and reaction engineering[8,9]. Further, while the field of membrane reactors is of relatively recent vintage[10], fuel cells that possess many of the characteristics of membrane reactors have been around for well over a century. Thus, the field of membrane reactors can glean much from a careful study of this intriguing device.

The transport-kinetic modeling of fuel cell viewed as a catalytic membrane reactor[52] can shed further light on its design and operational factors, which is our objective here. Theoretical modeling of transport and reaction in fuel cells is challenging due to the complexity of the device and the numerous design and operating parameters that can influence its performance. Models describing gas-diffusion electrodes and processes therein have been in development since the 1960s[11,12,13,34]. Theoretical models of fuel cell performance tend to be either rather complex requiring considerable numerical effort, e.g., the comprehensive model of Bernardi and Verbrugge[14,15] or semi-empirical[16], or empirical[17]. The former are useful for a detailed mechanistic understanding of the factors that influence the fuel cell performance, while the latter are useful for simply predicting the overall performance of individual fuel cells in a stack[18]. Fuel cell models of varying degrees of detail and complexity are also given by Leddy and Vanderborgh[19], Ridge et al.[36], Fuller and Newman[20], Nguyen et al.[21], Springer et al.[22,23,24], Weisbrod et al.[37] and Perry et al.[25]. Our objective here is to develop an analytical model for PEM fuel cells by drawing parallels with membrane reactors and incorporating transport and reaction details coupled with judicious assumptions to provide an analytical model that is both simple to use as well as quite complete. Some aspects, e.g., MEA structure and electrocatalysis, are described in sufficient detail to introduce the catalytic membrane reactor technologist to the PEM fuel cell.

MEA Nanostructure

The MEA structure comprising of gas-diffusion layer/anode catalyst/electrolyte/cathode catalyst/gas-diffusion layer composite is shown in Figure III-1. In a nutshell, H_2 is split into protons and electrons at the anode electrocatalyst. Protons find their way to the cathode through the proton-exchange membrane, while the electrons arrive at the cathode via the external circuit after performing useful work. Here, aided by electrode potential, the protons and electrons recombine with O_2 at the catalyst surface to form water. The MEA is sandwiched between two graphite plate current collectors, with machined microchannels, as in microchannel reactors[26] for gas distribution.

The gas-diffusion backing (GDB) (layers *D* and *E*) serves as the electron collector and a permeator for reactant gases as well as for liquid water. The proton-exchange membrane (PEM) (layer *B*) requires water for effective proton transport, which limits the practical operating temperature of atmospheric fuel cells to about 80 ºC (when water vapor pressure is roughly half an atm). However, if the pores of the gas-diffusion layers get filled with liquid water, transport of oxygen and hydrogen to the catalyst layers is impeded, severely limiting the fuel cell performance. This is avoided by imparting hydrophobicity to the gas-diffusion layers to allow gas and liquid phases to co-exist within pores. The gas-diffusion backing typically involves a carbon cloth, about 350 μm in thickness and woven from carbon fibers, on the one side of which the catalyst layer is deposited. The carbon cloth is treated with 40 - 70 wt.% poly-tetrafluoroethylene (PTFE, e.g., Teflon®) mixed with 10 - 20 nm carbon particles followed by sintering to melt the PTFE and coat the carbon fibers[27] and rendering it quite hydrophobic. The initial porosity of the carbon cloth is 70 - 80%, but its finished porosity is 55 - 65%.

The catalyst layer is 5-50 μm in thickness and contains Pt microcrystallites, roughly 2 - 4 nm in diameter, supported on the surface of largely non-porous carbon black particles, around 30 nm in diameter, at a Pt/C loading of about 20 - 40 wt.% and ≤ 0.4 mg Pt/cm^2 of MEA area. The interstitial spaces among the carbon particles are filled with an ionomer (e.g., Nafion®) solution to allow proton transport[28], and occasionally with some PTFE, although the latter may not be necessary for thin catalyst layers[29]. The deposition of the catalyst layer on the gas-diffusion electrode is accomplished by painting, spraying, or filtration, of the catalyst/ionomer dispersion. A polymer electrolyte membrane (e.g., Nafion® 115 or 117), 50-175 μm thick, is hot-pressed at a temperature slightly above its glass-transition temperature between the two electrodes such that the catalyst layers are on either side of the membrane. Alternate fabrication procedures are also employed[29].

The electrons produced at the anode catalyst surface are conducted via the carbon catalyst support and the carbon fibers of the gas-diffusion backing to the current collector and thence to the external circuit. The protons diffuse through the ionomer solution within the catalyst layer and then through the proton-exchange membrane to arrive at the cathode. The catalyst layer is, thus, designed to maximize the interfacial area among the its various phases, namely, the catalyst crystallites, the carbon support, the hydrophilic region consisting of ionomer, and any hydrophobic region containing Teflon®. In addition to good interfacial contact among the layers, the continuity of the respective phases for electronic and protonic conduction is also essential. If there is too little ionomer, for instance, the proton conduction pathway will be fragmented. On the other hand, too much ionomer could compromise electronic conductivity by further distancing the carbon particles and increasing the path length for proton conduction.

The PFSA membranes such as Nafion® produced by Du Pont (and similar membranes produced by Dow, W. L. Gore, and Asahi Glass) consist of a fluorocarbon, Teflon®-like, backbone with side-chains culminating in $–SO_3H$ groups. In the presence of water, these sulfonic acid groups dissociate, forming hydronium ions[30] responsible for proton conduction. There are many studies on the nanostructural aspects of the Nafion® membranes. Based on small angle X-ray diffraction and other characterization studies, Gierke and co-workers[31,32] proposed in their "cluster–network model" that the incompatibility of the fluorocarbon and the hydrophilic phase leads to the formation of inverted micelles, 3 - 5 nm in diameter, which are interconnected through short narrow channels, 1 - 2 nm in diameter, to provide a network for proton diffusion interspersed throughout the fluorocarbon matrix. The conductivity of Nafion® is extremely sensitive to relative humidity (RH), being essentially an insulator below a threshold of about 10% RH and rising through several orders of magnitude to about 0.07 Siemens/cm at 80 ºC and 100% RH[6]. The mechanism involving ordinary diffusion and Grotthus chain conduction explaining high proton conductivity in aqueous solutions is discussed by Glasstone et al.[33] and Bockris and Reddy [34]. Nafion® also deters short-circuiting of electrons, as well as cross-over of reactants, its permeability of H_2 and O_2 being of the order of only 10^{-10} mol/cm^2 s atm[3].

Constitutive Relations

The mass balance equations for species *i* (*i*=1,2,…,*n*)

$$\nabla \cdot \mathbf{N}_i = \sum_{\rho=1}^{q} \nu_{\rho i} r_\rho \qquad [1]$$

need to be solved subject to appropriate boundary conditions in the various layers of the fuel cell MEA (Figure III-1), for which flux relations for the different layers are needed as well as the kinetics of the anode and cathode reactions. Since the constitutive relations used here are somewhat different from those used conventionally, these are first discussed. Once the species fluxes are determined, the current density is obtained from

$$\mathbf{i} = F\sum_{i=1}^{n} z_i \mathbf{N}_i \qquad [2]$$

Dusty-Fluid Model

The flux model for $\boldsymbol{N}_i$ in a porous layer α is assumed here to be the dusty-fluid model (DFM)[35] (Mason and Malinauskas, 1983), written in the form (Thampan et al., 2000)[6]

$$-\frac{c_i}{RT}\nabla_T \mu_i^e = \sum_{\substack{j=1 \\ j\neq i}}^{n} \frac{1}{cD_{ij}^e}(c_j\mathbf{N}_i - c_i\mathbf{N}_j) + \frac{\mathbf{N}_i}{D_{iM}^e} + \frac{c_i B_0}{\mu D_{iM}^e}\left[\nabla p + \left(\sum_{j=1}^{n} c_j z_j\right) F \nabla \phi\right] \qquad [3]$$

$$(i = 1, 2, ..., n)$$

where the electrochemical potential gradient on the left-hand side represents the driving force for an electrochemical system, $\nabla_T \mu_i^e = \nabla_T \mu_i + z_i F \nabla \phi$. The DFM includes ordinary diffusion represented by D_{ij}^e, membrane diffusion represented by D_{iM}^e that accounts for the friction between i and the membrane, as well as convective flux represented by the last term on the right-hand side (rhs) of Eq. 3, which includes contributions both due to a pressure gradient (d'Arcy term) as well as a potential gradient (electroosmosis). The d'Arcy permeability and the effective diffusion coefficients in the DFM for layer α are given by the relations

$$D_{ij}^e = K_{1\alpha} D_{ij} = (\varepsilon_\alpha - \varepsilon_{\alpha 0})^q D_{ij} \quad ; \; D_{iM}^e = K_{0\alpha} D_{iM} \, ; \; B_{0\alpha} = (\varepsilon_\alpha - \varepsilon_{\alpha 0})^q a_\alpha^2 / 8 \qquad [4]$$

where ε_α is the void fraction of layer α, $\varepsilon_{\alpha 0}$ is the corresponding percolation threshold, and the critical (or Bruggeman) exponent $q = 1.5^6$ and a_a is the mean pore radius. Summing Eq. 3 over all species, the Stefan-Maxwell terms cancel out, resulting in

$$\left[\nabla p + \left(\sum_{j=1}^{n} c_j z_j\right) F \nabla \Phi\right] = -\frac{RT}{W} \sum_{j=1}^{n} \frac{\mathbf{N}_j}{D_{jM}^e} \qquad [5]$$

where

$$W \equiv 1 + \frac{B_0 cRT}{\mu} \sum_{h=1}^{n} \frac{x_h}{D_{hM}^e} \qquad [6]$$

Using Eq. 5 in Eq. 3 to eliminate the convective driving force on its right-hand side, the DFM may be written in the following alternate form

$$-\frac{c_i}{RT} \nabla_T \mu_i^e = \sum_{\substack{j=1 \\ j \neq i}}^{n} \frac{1}{cD_{ij}^e} (c_j \mathbf{N}_i - c_i \mathbf{N}_j) + \frac{\mathbf{N}_i}{D_{iM}^e} - \frac{c_i B_0 RT}{\mu D_{iM}^e W} \sum_{j=1}^{n} \frac{\mathbf{N}_j}{D_{jM}^e} \qquad [7]$$

$$(i = 1, 2, ..., n)$$

This form of DFM contains the driving force for *i* on the left-hand side, and fluxes of all species on the right-hand side. It may, of course, be inverted to alternately provide flux of species *i* in terms of the driving forces of all species[6]. However, if the flux ratios N_j/N_i of the various species *j* with respect to the key species *i* are known, as, e.g., through reaction stoichiometry (as in the case for fuel cells), the following Fickian form for flux may be obtained

$$\mathbf{N}_i = -\frac{1}{RT} D_i^e c_i \nabla_T \mu_i^e \quad ; \quad (i=1,2,...,n) \qquad [8]$$

where the effective diffusivity is

$$\frac{1}{D_i^e} = \sum_{\substack{j=1 \\ j \neq i}}^{n} \frac{1}{cD_{ij}^e} \left(c_j - c_i \frac{\mathbf{N}_j}{\mathbf{N}_i}\right) + \frac{1}{D_{iM}^e} - \frac{c_i B_0 RT}{\mu D_{iM}^e W} \sum_{j=1}^{n} \frac{1}{D_{jM}^e} \frac{\mathbf{N}_j}{\mathbf{N}_i} \qquad [9]$$

$$(i = 1, 2, ..., n)$$

These results are used to obtain permeability of the gas-diffusion layers as well as the conductivity of the proton-exchange membrane.

Transport of Gases in Gas-Diffusion Backing (Layers D and E)

Although it has been conventional to use Stefan-Maxwell equations to describe the gas-phase diffusion in GDB[36,22,14,37], these equations include only the molecular diffusion and are, in general, incomplete for description of transport of gases in porous media. Thus, the dusty-gas model (DGM)[38,35], obtained simply from the DFM described above specialized to the case of gases is utilized here. For the case of gaseous transport, the driving force in DFM reduces simply to $c_i \nabla_T \mu_i^e = \nabla p_i$. Further, the membrane diffusion coefficient D_{iM}^e simply becomes the familiar Knudsen diffusion D_{iK}^e coefficient for gases. Actually, the effective diffusivity in a partially liquid-filled porous layer α is appropriately given by[39]

$$D_{i\alpha}^e = (1-q_w)^q D_{iG}^e + q_w^q \kappa_{iL} K_1 D_{iL} \approx (1-q_w)^q D_{iG}^e \qquad [10]$$

where D_{iL} is the liquid-phase diffusivity, and D_{iG}^e is the effective gas-phase diffusivity for the *dry* porous layer. Equation 10 accounts for the simultaneous transport of species *i* through the residual gas pore space as well as any through the liquid phase. The approximation on the right-hand side of Eq. 10 is made here, however, assuming that the flux contribution of the aqueous phase within the gas-diffusion layers is unimportant due to the low solubility (small partition coefficient, κ_{iL}) of the gases. The gas-phase diffusivity in Eq. 10 is obtained from Eq. 9, written in terms of partial pressures, however, rather than concentrations

$$\frac{1}{D_{iG}^e} = \frac{1}{D_{iK}^e} + \sum_{\substack{j=1 \\ j\neq i}}^{n} \frac{1}{D_{ij}^{eo}}\left(p_j - p_i \frac{\mathbf{N}_j}{\mathbf{N}_i}\right) - \frac{p_i B_0}{\mu W D_{iK}^e} \sum_{j=1}^{n} \frac{\mathbf{N}_j}{\mathbf{N}_i} \frac{1}{D_{jK}^e} \qquad [11]$$

Here the pressure-independent ordinary diffusivity and the effective Knudsen diffusivity[40]

$$D_{ij}^{eo} \equiv pD_{ij}^{e} = pK_1 D_{ij} \qquad ; \qquad D_{iK}^{e} = K_0 \sqrt{\frac{8RT}{\pi M_i}} \qquad [12]$$

where the dusty-gas structural parameters for the dry porous layer for Knudsen diffusion is $K_0 = (\varepsilon_\alpha - \varepsilon_{\alpha 0})^q (2a_\alpha / 3)$.

As done by others[13], it is next assumed that due to the presence of liquid water in the pores of the gas-diffusion backing, the gas phase is saturated with water vapor, i.e., the partial pressure of water is equal to its vapor pressure at the fuel cell temperature ($p_w = p_w^o$). Thus, under isothermal conditions, there is no partial pressure gradient of water vapor in GDB. Although this does not necessarily imply that the water vapor flux in the gas phase is zero, for simplicity it is further assumed here that $\boldsymbol{N}_w = 0$. In other words, water transport is assumed to occur entirely through the liquid phase. Further, for N_2 in the case of cathode and CO_2 in the case of anode, denoted as the diluent species *d*, $\boldsymbol{N}_d = 0$. Using this in Eqs. 11 and 6, the effective diffusivity of *i* (H_2 in the case of anode, or O_2 in the case of cathode)

$$\frac{1}{D_{iG}^{e}} = \frac{p_w}{D_{iw}^{eo}} + \frac{p_d}{D_{id}^{eo}} + \frac{1}{D_{iK}^{e}} \left\{ \frac{1 + \frac{B_0}{\mu}\left(\frac{p_w}{D_{wK}^{e}} + \frac{p_d}{D_{dK}^{e}} \right)}{1 + \frac{B_0}{\mu}\left(\frac{p_i}{D_{iK}^{e}} + \frac{p_w}{D_{wK}^{e}} + \frac{p_d}{D_{dK}^{e}} \right)} \right\} \qquad [13]$$

Transport of Protons in Proton-Exchange Membrane (Layer B)

We have recently shown[6] that for binary case of proton transport in a PEM consisting of water as the solvent (species *w*), and the hydronium ion (H_3O^+), denoted as species H^+, as the charge carrier, and for spatially homogeneous sulfonic acid groups within PEM coupled with local electroneutrality, the electrochemical potential gradient simply becomes potential gradient.

Further, for equimolar counter-diffusion and for $D^e_{\mathrm{H}^+M} \approx D^e_{wM}$ due to the similarity between w (water) and H^+ (hydronium ion), the effective diffusivity (Eq. 9) reduces to

$$\frac{1}{D^{\mathrm{e}}_{\mathrm{H}^+}} \approx \frac{1}{D^e_{\mathrm{H}^+w}} + \frac{1}{D^e_{\mathrm{H}^+M}} \qquad [14]$$

namely, the Bosanquet equation[40]. Further, with $\sigma = (F^2 / RT) D^{\mathrm{e}}_{\mathrm{H}^+} c_{\mathrm{H}^+}$, and $c_{\mathrm{H}^+} = c_{\mathrm{HA},0}\alpha$, and in terms of the equivalent conductance, $\lambda^0_{\mathrm{H}^+} \equiv F^2 \left| z_{\mathrm{H}^+} \right| D_{\mathrm{H}^+w} / RT$, the conductivity of PEM becomes

$$\sigma = (\varepsilon_B - \varepsilon_{B0})^q \left(\frac{\lambda^0_{\mathrm{H}^+,298}}{1+\delta} \right) \exp\left\{ -\frac{E_\mu}{R}\left(\frac{1}{T} - \frac{1}{298} \right) \right\} c_{\mathrm{HA},0}\alpha \qquad [15]$$

where the ratio $\delta \equiv D^e_{\mathrm{H}^+w} / D^e_{\mathrm{H}^+M}$, and the degree of dissociation in terms of the equilibrium constant $K_{\mathrm{A},C}$ for the protonation reaction, $\mathrm{AH} + \mathrm{H_2O} \leftrightarrows \mathrm{H_3O^+} + \mathrm{A^-}$, is

$$\alpha = \frac{(\lambda+1) - \sqrt{(\lambda+1)^2 - 4\lambda(1 - 1/K_{\mathrm{A},C})}}{2(1 - 1/K_{\mathrm{A},C})} \qquad [16]$$

where

$$K_{\mathrm{A,C}} = K_{\mathrm{A,C,298}} \exp\left[-\frac{\Delta H^o}{R}\left(\frac{1}{T} - \frac{1}{298} \right) \right] \qquad [17]$$

The volume fraction of water in PEM is related to the number of water molecules sorbed per –$\mathrm{SO_3H}$ group, λ,

$$\varepsilon_B = \frac{\lambda}{\frac{\overline{V}_M}{\overline{V}_w} + \lambda} \qquad [18]$$

where $\overline{V}_M \approx EW / \rho_0$ = 537 cm^3/mol, and $\overline{V}_w$ = 18 cm^3/mol. The water molecules sorbed are given in terms of relative humidity (RH, or a_w), by n_w–layer Brunauer-Emmett-Teller (BET) equation[41] (Adamson and Gast. 1997)

$$\frac{\lambda}{\lambda_m} = \frac{[Ca_w/(1-a_w)][1-(n_w+1)a_w^{n_w} + n_w a_w^{n_w+1}]}{1+(C-1)a_w - Ca_w^{n_w+1}} \tag{19}$$

where the RH or the water vapor activity, $a_w = p_w / p_w^o$, λ_m is the water loading at monolayer coverage, and n_w is the total number of water layers in the pores at saturation. We have recently shown that the above model for proton conduction in PEM provides an excellent correlation with a variety of experimental data[6].

Electrocatalysis: General Considerations

Some of the general characteristics of electrocatalytic reactions are first presented, including how their rates are influenced by potential. Consider the electrode surface reaction ρ

$$\sum_{\substack{i=1 \\ i\neq e^-}}^{n} \nu_{\rho i} \mathrm{A}_i^{z_i} + \nu_{\rho e^-} \mathrm{e}^- = 0 \tag{20}$$

among n species, $\mathrm{A}_i^{z_i}$, carrying a charge z_i, where $\nu_{\rho e^-}$ is the stoichiometric coefficient of the electron in reaction ρ. Thus, $\nu_{\rho e^-} = +n_\rho$ for an anodic reaction while $\nu_{\rho e^-} = -n_\rho$ for a cathodic reaction, where n_ρ is the number of electrons involved in the reaction ρ. There is, of course, overall charge balance in the electrode reaction, i.e.,

$$\sum_{\substack{i=1 \\ i\neq e^-}}^{n} \nu_{\rho i} z_i = \nu_{\rho e^-} \tag{21}$$

For an *elementary* electrode reaction ρ, the *net* rate of reaction per unit supported metal catalyst surface area, r_ρ^* (e.g., mol/ cm^2 Pt. s), from the thermodynamic formulation of the transition-state theory (TTST)[42] is

$$r_\rho^* = \vec{r}_\rho^* - \overleftarrow{r}_\rho^* = \vec{k}_\rho^* \prod_{i=1}^{r} a_i^{-\nu_{\rho i}} - \overleftarrow{k}_\rho^* \prod_{i=r+1}^{n} a_i^{\nu_{\rho i}} \tag{22}$$

where the first r of the total of n species are assumed to be the reactants while the remaining are products. For surface species, the activity in Eq. 22 corresponds to surface activity, which for an ideal surface is just the fractional surface coverage. The potential dependence of the rate constants

$$\vec{k}^*_\rho = \vec{k}^*_{\rho,\Phi_0} \exp\left\{\frac{\beta_\rho \nu_{\rho e^-} F\eta}{RT}\right\} \quad ; \quad \overleftarrow{k}^*_\rho = \overleftarrow{k}^*_{\rho,\Phi_0} \exp\left\{\frac{(\beta_\rho - 1)\nu_{\rho e^-} F\eta}{RT}\right\} \qquad [23]$$

where $\vec{k}^*_{\rho,\Phi_0}$ is the rate constant at the equilibrium electrode potential Φ_0, i.e.,

$$\vec{k}^*_{\rho,\Phi_0} = \left(\kappa \frac{k_B T}{h\gamma^\pm} e^{\frac{\Delta \vec{S}^{\pm o}_{\rho T,\Phi=0}}{R}}\right) \exp\left(-\frac{\Delta \vec{H}^{\pm o}_{\rho T,\Phi=0} - \beta_\rho \nu_{\rho e^-} F\Phi_0}{RT}\right) \equiv A_\rho \exp\left(-\frac{E_{\rho,\Phi_0}}{RT}\right) \qquad [24]$$

and similarly for $\overleftarrow{k}_{\rho,\Phi_0}$. These equations clearly show that the potential has a powerful effect on the Gibbs free energy of activation and hence the rate constants of electrodic reactions, in addition, of course, to the strong effect of temperature. In the above, Φ_0 is a function of composition as given by the Nernst equation, $\eta \equiv \Phi - \Phi_0$ is the electrode overpotential, and β_ρ is the so-called symmetry factor for the reaction ρ, also referred to as the transfer coefficient resulting from the application of linear free energy relationship, universally assumed to be one-half for elementary reactions[42]. The second form of the rate constant Φ_0 in Eq. 24 is the usual Arrhenius form, for which the pre-exponential factor and activation energy may be obtained by comparison with the TTST form. It may be noted that the effect of potential on the forward and reverse rate constants is such that one increases while the other reduces with overpotential. The ratio, $K_\rho = \vec{k}_\rho / \overleftarrow{k}_\rho$, namely the equilibrium constant for the elementary reaction ρ

$$K_\rho = K_{\rho,\Phi_0} \exp\left(\frac{\nu_{\rho e^-} F\eta}{RT}\right) \qquad [25]$$

is also greatly influenced by potential.

Under open-circuit conditions for the given composition, $\eta = 0$, $r_\rho^* = 0$, and, thus, from Eqs. 22 and 23,

$$\vec{r}^{\,*}_{\rho 0} = \vec{k}^{*}_{\rho,\Phi_0}\prod_{i=1}^{r} a_i^{-\nu_{\rho i}} = \overleftarrow{r}^{*}_{\rho 0} = \overleftarrow{k}^{*}_{\rho,\Phi_0}\prod_{i=r+1}^{n} a_i^{\nu_{\rho i}} \qquad [26]$$

i.e., the cell potential assumes the equilibrium value Φ_0, corresponding to the given composition and temperature, so that the forward and reverse reactions rates are equal and a dynamic equilibrium is established. This may be rearranged into the well-known Nernst equation,

$$\Phi = \Phi_0^0 + \frac{RT}{F\nu_{\rho e^-}}\ln\prod_{\substack{i=1\\ i\neq 1}}^{n} a_i^{\nu_{\rho i}} \qquad [27]$$

where Φ_0^o is the standard equilibrium electrode potential corresponding to unit species activities.

The above kinetic equations may be written in the form of the Butler-Volmer equation as follows. Using Eqs. 23 and 26, Eq. 22 may be written as

$$\begin{aligned} r_\rho^* &= \vec{r}^{\,*}_{\rho 0}\left[\exp\left\{\frac{\beta_\rho \nu_{\rho e^-} F\eta}{RT}\right\} - \exp\left\{\frac{(\beta_\rho - 1)\nu_{\rho e^-} F\eta}{RT}\right\}\right] \\ &= \overleftarrow{r}^{*}_{\rho 0}\left[\exp\left\{\frac{\beta_\rho \nu_{\rho e^-} F\eta}{RT}\right\} - \exp\left\{\frac{(\beta_\rho - 1)\nu_{\rho e^-} F\eta}{RT}\right\}\right] \end{aligned} \qquad [28]$$

or in a pseudo-irreversible form

$$r_\rho^* = k_\rho^*\prod_{i=1}^{r} a_i^{-\nu_{\rho i}} \qquad [29]$$

where the effective rate constant is given by the Butler-Volmer form

$$k_\rho^* = \vec{k}^{*}_{\rho,\Phi_0}\left\{\exp\left(\frac{\beta_\rho \nu_{\rho e^-} F\eta}{RT}\right) - \exp\left(\frac{(\beta_\rho - 1)\nu_{\rho e^-} F\eta}{RT}\right)\right\} \qquad [30]$$

For the common value $\beta_\rho = 1/2$, this may be written in the more convenient alternate form

$$k_\rho^* = \vec{k}_{\rho,\Phi_0}^* \left\{ 2\sinh\left(\frac{\nu_{\rho e^-} F\eta}{2RT} \right) \right\} \qquad [31]$$

The corresponding current density of i^* (A/cm^2 catalyst surface) is obtained from

$$i^* = F\sum_{\substack{i=1 \\ i\neq e^-}}^{n} z_i N_i^* = Fr_\rho^* \sum_{\substack{i=1 \\ i\neq e^-}}^{n} z_i \nu_{\rho i} = F\nu_{\rho e^-} r_\rho^* \qquad [32]$$

where the current direction is determined by the stoichiometric coefficient of electrons. The second equality in Eq. 32 stems from the assumption of the absence of diffusional limitations, while the third equality utilizes Eq. 21. Similarly, the exchange-current density, namely the current in the forward and reverse direction under open circuit conditions, $i_0^* = F\nu_{\rho e^-}\vec{r}_{\rho 0}^*$, which depends upon temperature and composition.

The current density i in terms of A/cm^2 of geometric (MEA) area is $i = \gamma_M i^*$ and $i_0 = \gamma_M i_0^*$. Here, the ratio of electrochemically active metal catalyst surface area to the geometric MEA area (cm^2 Pt/cm^2 geometric MEA area)[56], also frequently referred to as the roughness factor[61].

$$\gamma_M = \varphi_I m_M \left(\frac{6\varphi_M}{\rho_M d_M} \right) \qquad [33]$$

where φ_M accounts for the part of the metal crystallite of diameter d_M which is not accessible for reaction, e.g., the side which is in contact with the support, and φ_I is the fraction of the available metal surface participating in electrocatalysis. This would be less than unity, e.g., if not all of the available metal area is in contact with the ionomer, and hence depends upon ionomer loading m_I. Using the above, the current density is related to exchange-current density and over-potential by

$$\frac{i^*}{i_0^*} = \frac{i}{i_0} = \left\{ 2\sinh\left(\frac{\nu_{\rho e^-} F\eta}{2RT} \right) \right\} \quad [34]$$

For large overpotential η, this reduces to the familiar Tafel equation

$$\frac{i}{i_0} \approx \exp\left(\frac{\nu_{\rho e^-} F\eta}{2RT} \right) \quad [35]$$

whereas for small overpotential η, may be approximated by a linear form

$$\frac{i}{i_0} \approx \frac{\nu_{\rho e^-} F\eta}{RT} \quad [36]$$

Hydrogen Oxidation Reaction (HOR)

The catalytic hydrogen electrode reaction

$$H_2 \leftrightarrows 2H^+ + 2e^- \quad [37]$$

has been much studied[43], but its mechanism and kinetics are still uncertain[44,47]. The two most common mechanisms are the so-called Tafel-Volmer mechanism and the Heyrovsky-Volmer mechanism[44]. The former constitutes a Tafel step, namely, the dissociative chemisorption of hydrogen, which is usually assumed to be the rate determining step (rds), followed by a Volmer step involving dissociation of the adsorbed hydrogen atom to produce an electron and a solvated proton, i.e.,

(Tafel step) $2S + H_2 \leftrightarrows 2S{\bullet}H$ (rds) [38]

(Volmer step) $S{\bullet}H \leftrightarrows S + H^+ + e^-$ [39]

where S represents a catalyst site. A rate expression for the HOR is[45]

$$r_A^* = \vec{k}_A^* c_{H_2} \exp\left(\frac{\vec{\alpha}_A F\eta_A}{RT} \right) - \overleftarrow{k}_A^* c_{H^+}^2 \exp\left(-\frac{\overleftarrow{\alpha}_A F\eta_A}{RT} \right) \quad [40]$$

The lack of an adsorption term in the denominator of this expression may be justified in view of $\theta_{\mathrm{S\bullet H}} << 1$. Following the development in the above section, for the effective transfer coefficient of the overall HOR, $\vec{\alpha}_A = \overleftarrow{\alpha}_A = 1/2$, this may be written in the pseudo-irreversible form

$$r_A^* = k_A^* c_{H_2} \tag{41}$$

where

$$k_A^* = \vec{k}_{A,\Phi_0}^* \left\{ 2\sinh\left(\frac{\vec{\alpha}_A F \eta_A}{RT} \right) \right\} \tag{42}$$

Further, from $i_{A,0}^* = F\nu_{Ae^-}\vec{r}_{A0}^*$ with $\nu_{Ae^-} = +2$ (reaction 37), the *reference* exchange current density, $i_{A,0,ref}^* = 2F\vec{k}_{A,\Phi_0}(T_{ref})c_{H_2,ref}$. The reaction is very rapid, particularly as compared with the oxygen reduction reaction at the cathode, with an exchange current density $i_{A,0,ref}^* \approx 1$ mA/cm^2 Pt[3] at standard conditions, so that the overpotential due to the HOR is relatively small. Even though the HOR reaction is very facile on Pt, the many species emanating from the reformer can successfully compete with it for Pt sites. In particular, for reformed hydrocarbons, anode feed may contain roughly 100 ppm CO, which adsorbs on Pt

$$\mathrm{S} + \mathrm{CO} \leftrightarrows \mathrm{CO{\bullet}S} \tag{43}$$

Since the adsorption enthalpy of CO on Pt (–32 kcal/mol) is much higher than that for the other species present, it may be considered as the most abundant surface species[57]. For instance, at 100 ppm, roughly 80% of the sites are occupied by CO. Under such conditions, therefore, the rate of HOR must be modified to include $(1 - \theta_{\mathrm{CO\bullet S}})^2$ on its right-hand side[46]. Thus, with $i_{A,0} = \gamma_{MA} i_{A,0}^*$, the exchange-current density

$$i_{A,0} = \gamma_{M,A}(1-\theta_{\mathrm{CO\bullet S}})^2 \left(\frac{c_{H_2}}{c_{H_2,ref}} \right) \exp\left\{ -\frac{E_{A,\Phi_0}}{R}\left(\frac{1}{T} - \frac{1}{T_{ref}} \right) \right\} i_{A,0,ref}^* \tag{44}$$

where E_{A,Φ_0} is the effective activation energy of i_{A0} or $\vec{k}_{A,\Phi_0}$ (Eq. 24). Thus, increasing $i_{A,0}$ may be accomplished by increasing $\gamma_{M,A}$, temperature, and H_2 concentration and reducing poisoning.

Oxygen Reduction Reaction (ORR)

The catalytic oxygen reduction reaction

$$O_2 + 4H^+ + 4e^- \leftrightarrows 2H_2O \qquad [45]$$

has also been extensively investigated due to its great importance in energy conversion and storage, and a large number of mechanisms have been proposed[47,48], none of which are entirely satisfactory from the viewpoint of observed kinetics. Certain experimental features of the reaction under acidic conditions, however, are well established[50] : *i*) two different Tafel slopes are observed, namely around −60 mV (−2.303 *RT*/*F*) at low cds (3×10^{-7} to about 3×10^{-5} A cm^{-2}) and −120 mV (−2.303 2*RT*/*F*) at higher cds (> 3×10^{-5} A cm^{-2}); *ii*) reduction is first-order in oxygen at all cds; *iii*) it is 1.5 order in proton concentration at low cds and first-order at higher cds[43]; *iv*) the surface coverage of adsorbed oxygen is probably small[43]; and *v*) H_2O_2 is a detectable intermediate. We adopt the following rate expression[49]

$$r_C^* = k_C^* c_{O_2} c_{H^+} \qquad [46]$$

with

$$k_C^* = \vec{k}_{C,\Phi_0}^* \left\{ 2\sinh\left(-\frac{\vec{\alpha}_C F \eta_C}{RT} \right) \right\} \qquad [47]$$

As mentioned above, the effective transfer coefficient $\vec{\alpha}_C = 1$ (Tafel slope, *b* = 2.303 *RT/F*) at low cds (fuel cell voltages above 0.8 V), while below this voltage (high cds), frequently $\vec{\alpha}_C$ = 1/2 (Tafel slope, *b* = 2.303 x 2*RT/F*) is observed[64,50]. Since most of the overpotential occurs at low cds, in this analysis we assume $\vec{\alpha}_C = 1$ at all cds. A more accurate analysis might utilize two different effective transfer coefficients. On the other hand, this doubling of slope may also been explained simply on the basis of diffusional control at higher cds. The exchange current density under reference conditions from $i_{C,0}^{*} = F\nu_{Ce^{-}}\vec{r}_{C0}^{*}$, with $\nu_{Ce^{-}} = -4$, is

$i_{C,0,ref}^{*} = -4\frac{c_t^{*}}{c^2}\vec{k}_{1C,\Phi_0}(T_{ref})c_{O_2,ref}c_{H^+,ref}$. Thus

$$i_{C,0} = \gamma_{M,C}\left(\frac{c_{O_2}}{c_{O_2,ref}}\right)\left(\frac{c_{H^+}}{c_{H^+,ref}}\right)\exp\left\{-\frac{E_{C,\Phi_0}}{R}\left(\frac{1}{T}-\frac{1}{T_{ref}}\right)\right\}i_{C,0,ref}^{*} \qquad [48]$$

MEA Analysis

In order to analyze the fuel cell as a membrane reactor, the following steady-state one-dimensional conservation equations are considered in the MEA[51,52] :

Anode Chamber (Region *T*) $\quad F_T(c_{iT,0} - c_{iT}) = N_{iz}(0)\cdot A \qquad$ [49]

GDB (Layers *D* and *E*) $\quad \frac{dN_{iz}}{dz} = 0; \qquad N_{iz} = -D_{i\alpha}^{e}\frac{dc_i}{dz} \qquad$ [50]

PEM (Layer *B*) $\quad \frac{di}{dz} = 0; \qquad i = -\sigma\frac{d\phi}{dz} \qquad$ [51]

Catalyst (Layers *A* and *C*) $\quad \frac{dN_{iz}}{dz} = \nu_{i\rho}r_{\rho}; \quad N_{iz} = -\frac{1}{RT}D_{i\alpha}^{e}\left(\frac{dc_i}{dz} + z_i c_i F\frac{d\phi}{dz}\right) \qquad$ [52]

Cathode Chamber (Region *S*) $\quad F_S(c_{iS,0} - c_{iS}) = N_{iz}(e)\cdot A \qquad$ [53]

The anode and the cathode chamber equations are for a single (differential) fuel cell rather than for a stack. . Further, while as discussed above, the effective diffusivities in the GDBs are clearly functions of composition and hence position, they are assumed to be constant here in order to obtain an analytical solution. The solution for flux in the gas-diffusion layer

α (layer *D* or *E*) obtained by integrating Fickian flux equation for constant flux and constant effective diffusivity is

$$N_{i\alpha} = P_{i\alpha}\left\{c_{iG} - \frac{c_{i\alpha}(L_\alpha)}{\kappa_{i\alpha}}\right\} \qquad [54]$$

In this, the permeability of species *i* is $P_{i\alpha} \equiv \kappa_{i\alpha} D_{i\alpha} / L_\alpha$, where $\kappa_{i\alpha} \equiv (c_{i\alpha}/c_{iG})_{\mathrm{eq}}$ is the partition coefficient for phase α.

For the proton-exchange membrane similarly for constant conductivity, the solution is

$$i = \frac{\sigma}{L_B}\left\{\phi_{S,B}(b) - \phi_{S,B}(c)\right\} \qquad [55]$$

Model With No Diffusion Limitations In The Catalyst Layer

In order to obtain a simple analytical solution, we shall assume that the catalyst layers are thin enough so that *i*) there is no potential drop and further, *ii*) there are no diffusional limitations within these layers. While there is some support for the former through the numerical calculations of Bernardi and Verbrugge[14], the latter assumption is likely to be erroneous at higher cds. Nonetheless, the rate of the anodic reaction within the catalyst layer under these assumptions can be written as $r_A^* = k_A^* c_{H_2,A}(a)$ from Eq. 41 along with $c_{H_2,A} = c_{H_2,A}(a)$, i.e., the concentration of hydrogen throughout the catalyst layer is assumed to be uniform and equal to its value at $z = a$ (Figure III-1). Using this in $i_A^* = F\nu_{Ae^-} r_A^*$ along with $i_A = \gamma_M i_A^*$ gives the anode current density

$$i_A = \gamma_{MA} F \nu_{Ae^-} k_A^* c_{H_2,A}(a) \qquad [56]$$

where the rate constant for the anode layer is given by Eq. 42 while γ_{MA} is given by Eq. 33. Similarly, the anode exchange-current density is

$$i_{A,0} = \gamma_{MA} F \nu_{Ae^-} \vec{k}^{*}_{A,\Phi_0} \kappa_{H_2,A} c_{H_2,T} \qquad [57]$$

where use is made of $c_{H_2,A}(a) = \kappa_{H_2,A} c_{H_2,T}$ under equilibrium conditions, since there are, of course, no diffusional limitations in the gas-diffusion backing under equilibrium conditions.

The hydrogen flux at $z = a$ for a PEM that is impervious to it is obtained from material balance

$$N_{H_2}(a) = \gamma_{MA}(-\nu_{AH_2}) k_A^{*} c_{H_2,A}(a) \qquad [58]$$

The flux of hydrogen in the gas-diffusion backing of anode (Layer *D*) is obtained from Eqs. 49 and 54

$$N_{H_2}(0) = \frac{F_T}{A}\left(c_{H_2,0} - c_{H_2,T}\right) = N_{H_2}(a) = \gamma_{MA}(-\nu_{AH_2}) k_A^{*} c_{H_2,A}(a) \qquad [59]$$

An expression for the anodic current density can be obtained by equating Eqs. 58 and 59, solving for $c_{H_2,A}(a)$, and then using it in Eq. 56

$$i_A = \frac{\gamma_{MA} \nu_{Ae^-} F k_A^{*} \kappa_{H_2,A} c_{H_2,T}}{1 + \gamma_{MA}(-\nu_{AH_2}) k_A^{*} \kappa_{H_2,A}\left(\frac{1}{P_{H_2,D}} + \frac{A}{F_T}\right)} \qquad [60]$$

For our purpose here, it is assumed that both pure hydrogen and oxygen are fed into the anode and cathode chambers, so that in $c_{iT} = c_{iT,0}$ and $c_{iS} = c_{iS,0}$, although this won't hold if reformate and air were used. Thus in the case of a gas-diffusion controlled rate, neglecting unity in the denominator, Eq. 60 simplifies to provide an expression for the anodic limiting current density

$$i_{A,L} \equiv \left(\frac{\nu_{Ae^-}}{-\nu_{AH_2}}\right) F P_{H_2,D} c_{H_2,T} \qquad [61]$$

Using Eqs. 57 and 61 in Eq. 60 and rearranging

$$\frac{k_A^*}{\vec{k}_{A,\Phi_0}^*} = \left\{ \frac{i_A / i_{A,0}}{1 - i_A / i_{A,L}} \right\} \qquad [62]$$

Finally use of Eq. 42 in Eq. 62 results in a convenient form for the anodic overpotential

$$\eta_A = \frac{RT}{\vec{\alpha}_A F} \sinh^{-1}\left[\frac{1}{2} \left\{ \frac{i_A / i_{A,0}}{1 - i_A / i_{A,L}} \right\} \right] \qquad [63]$$

A similar derivation for the cathode (layer *C*) leads to an expression the cathodic overpotential

$$-\eta_C = \frac{RT}{\vec{\alpha}_C F} \sinh^{-1}\left[\frac{1}{2} \left\{ \frac{i_C / i_{C,0}}{1 - i_C / i_{C,L}} \right\} \right] \qquad [64]$$

where the cathodic limiting current

$$i_{C,L} \equiv \left(\frac{\nu_{Ce^-}}{-\nu_{C,O_2}} \right) F P_{O_2,E} c_{O_2,S} \qquad [65]$$

Overall Fuel Cell Performance

To obtain the current versus voltage relationship for the overall fuel cell we use, $V = \phi_{M,C} - \phi_{M,A} = (\Phi_{0,C} - \Phi_{0,A}) - \eta_A + \eta_C - (\phi_{S,A} - \phi_{S,C})$. Further, the potential drop in the solution phase due to the passage of current may be broken down further into individual components, i.e., $\phi_{S,A} - \phi_{S,C} = \{\phi_{S,A} - \phi_{S,B}(b)\} + \{\phi_{S,B}(b) - \phi_{S,B}(c)\} + \{\phi_{S,B}(c) - \phi_{S,C}\}$, where the first and the last terms are the interfacial resistance contributions between the two electrodes and the ion-exchange membrane, which may be substantial if poor fabrication techniques are employed or if the MEA becomes partially delaminated with use. Thus using Eqs. 63, 65 and 57 along with $i = i_A = i_C$, in this, there results

$$V = V_0 - \frac{RT}{\vec{\alpha}_A F}\sinh^{-1}\left\{\frac{1}{2}\left(\frac{i/i_{A,0}}{1-i/i_{A,L}}\right)\right\} - \frac{RT}{\vec{\alpha}_C F}\sinh^{-1}\left\{\frac{1}{2}\left(\frac{i/i_{C,0}}{1-i/i_{C,L}}\right)\right\} - i\left(\frac{L_B}{\sigma_B}\right) - i(R_I) \qquad [66]$$

where R_I accounts for any interfacial resistance, and the open circuit potential, $V_0 \equiv \Phi_{0C} - \Phi_{0A}$. The exchange current densities in Eq. 66 are given by Eqs. 44 and 48 for the anode and cathode, respectively, while the limiting current densities are given by Eqs. 61 and 65. Further, the conductivity of the PEM is given by Eq. 15. It is useful to reiterate that the key assumptions in the derivation of Eq. 66 are the neglect of potential drop and diffusional resistance within the catalyst layer. Otherwise, the model is quite complete. It is also noteworthy that for $i \ / i_L \rightarrow 0$, Eq. 66 reduces to a simple addition of the Butler-Volmer type terms arising from kinetics.

The power density is simply obtained from the use of $P = iV$. For example utilizing Eq. 66

$$P = iV_0 - \frac{iRT}{\vec{\alpha}_A F}\sinh^{-1}\left\{\frac{1}{2}\left(\frac{i/i_{A,0}}{1-i/i_{A,L}}\right)\right\} - \frac{iRT}{\vec{\alpha}_C F}\sinh^{-1}\left\{\frac{1}{2}\left(\frac{i/i_{C,0}}{1-i/i_{C,L}}\right)\right\} - i^2\left(\frac{L_B}{\sigma_B}\right) - i^2(R_I) \qquad [67]$$

Reaction-Diffusion Model (Diffusion In The Catalyst Layer Is Considered)

Although we have developed a simple analytical model in the case where catalyst layer diffusion is neglected, with judicious assumptions, a simple reaction-transport model incorporating diffusion can be developed. This model is presented as applied to the cathode catalyst layer as diffusion maybe significant in this region. To consider the case of catalyst layer diffusion limiting cell performance, the O_2 flux into the catalyst layer that provides the current density ($i = 4FN_{3Z}(d)$) must be determined. Thus, the conservation equation Eq. 52 for oxygen can be written as

$$D_{3C}\frac{d^2c_{O_2,C}}{dz^2}-k_{C,eff}c_{O_2}=0 \qquad [68]$$

where $k_{C,eff}=k_Cc_{H^+}$. To obtain an analytical solution to Eq. 68 the ORR rate expression Eq. 46 was made pseudo-1st order in oxygen concentration based on the assumption that there is only a small variation in c_{H^+} if any within the catalyst layer. The validity of this assumption is dependent upon the distribution of the ionomer in the catalyst layer and its subsequent hydration[53], as a completely hydrated ionomer avails the maximum concentration of c_{H^+}.

Eq. 68 is written in dimensionless form by introducing a parameter frequently utilized in heterogeneous catalytic reactions, the Thiele modulus[54] (ϕ_C), defined here as

$$\phi_C=L_C\sqrt{\frac{k_{C,eff}}{D_{O_2C}}}=L_C\sqrt{\left(\frac{i_{0,c,ref}(K_{H^+,C}/K_{H^+B}}{2FL_Cc_{H_2C}c_{O_2,C,ref}}\right)\frac{c_{H^+,B(C)}}{D_{O_2,C}}\sinh\left(\frac{-2F\eta_C}{RT}\right)} \qquad [69]$$

Furthermore utilizing Eq. 69, the cathodic overpotenial can be written as

$$-\eta_C=\frac{RT}{\alpha F}\sinh^{-1}\left(\frac{\phi_C{}^2}{L_C}\frac{D_{O_2,C}2Fc_{O_2,C,ref}(K_{H^+,C}/K_{H^+,B}}{i_{0,C,ref}c_{H^+,B(C)}}\right) \qquad [70]$$

In a similar manner, the anodic overpotential may be written as

$$\eta_A=\frac{RT}{\alpha F}\sinh^{-1}\left(\frac{\phi_A{}^2}{L_A}\frac{D_{H_2,A}Fc_{H_2,ref}(K_{H^+,C}/K_{H^+,B}}{i_{0,A,ref}}\right) \qquad [71]$$

Eq. 68 written with the Thiele modulus becomes

$$\frac{d^2c_{O_2,C}}{dy_C{}^2}-\phi_C^2c_{O_2}=0\,; \qquad y_C\equiv\frac{z-c}{L_C}; \qquad [72]$$

where y_C is the dimensionless length through the catalyst layer.

The solution to Eq. 71 subject to the boundary conditions at $y_C = 0$, and $N_{O_2} = 0$, i.e. the PEM is impermeable to O2, and at $y_C = 1$, $c_{O_2,C} = c_{O_2,C}(d)$

$$c_{O_2,C}(y_C) = c_{O_2,C}(d)\frac{\cosh(\phi_C y_C)}{\cosh(\phi_C)} \qquad [73]$$

To obtain $c_{O_2,C}(d)$, the O2 flux at the cathode chamber /GDB / catalyst layer interface is assumed to be continuous. Thus

$$\frac{F_T}{A}(c_{iT,0} - c_{iT}) = P_{O_2,E}\left(\frac{c_{O_2,C}(d)}{K_{O_2,C}} - c_{O_2,S}\right) = -D_{O_2,C}\frac{dc_{O_2,C}(d)}{dz} \qquad [74]$$

Utilizing Eqs. 72 and 73 it is possible to obtain an expression for $c_{O_2,C}(d)$

$$c_{O_2,C}(d) = \frac{K_{O_2,C}c_{O_2,S}}{\left(1+\Lambda_3\phi_C tanh\left(\phi_C\right)\right)\left(1 - \frac{AP_{O_2,C}\phi_C tanh\left(\phi_C\right)}{F_l\left(1+\Lambda_3\phi_C tanh\left(\phi_C\right)\right)}\right)} \qquad [75]$$

where Λ_3 is $P_{O_2,C}/P_{O_2,E}$. Utilizing Eqs. 74 and 32 the current density can be expressed as

$$i = -4FP_{O_2,E}K_{O_2,C}c_{O_2,S}\left(\frac{\left(\Lambda_3 - P_{O_2,C}\frac{A}{F}\right)\phi_C tanh\left(\phi_C\right)}{1+\left(\Lambda_3 - P_{O_2,C}\frac{A}{F}\right)\phi_C tanh\left(\phi_C\right)}\right) \qquad [76]$$

In the case of a diffusion limited current at high flow rates, ϕ_c >> 3 and $\Lambda_3\phi_c$ >> 1, Eq. 74 becomes

$$i_L = -4FP_{O_2E}K_{O_2,C}c_{O_2S} \qquad [77]$$

Thus, an experimentally observed i_L, can provide an estimate of P_{O_2E}, in addition to theoretical calculations based on the Dusty-Gas Model and solubility data.

Solution Algorithm

When the $\phi_c < 1$, the current is limited by the reaction rate and a higher permeability will not increase the current. Alternatively when the $\phi_c > 1$, the current is diffusion limited and a permeability improvement will enhance the current density.

The solution algorithm is as follows,

1. Specify ϕ_c at a low value ~ 0.1.
2. Calculate i based on Eq. (74).
3. Calculate η_B and η_C and (set η_A at 0.1 V) based on Eqs. 15 and 70 respectively.
4. Utilize $V = V_0 - \eta_A + \eta_C - \eta_B$.
5. Plot V vs. i and iterate with increasing ϕ_c to obtain the complete polarization curve.

A comparison of the theoretical model with experiments is discussed next.

Comparison of Theory and Experiments

A comparison of the theoretical model (Eq. 66) above with PEM fuel cell experimental performance results is shown in Figure III-2 for the set of parameters listed in Table III-1 and $R_I = 0$. E-TEK double-sided electrodes and Nafion® 115 membrane were used to fabricate the MEA for the fuel cell, with platinum and Nafion® loadings of $m_M = 0.4$ mg Pt/cm^2 ($\omega_M = 0.2$ Pt on Vulcan XC 72) and $m_I = 0.7$ mg/cm^2, respectively. The MEA was prepared by sandwiching the Nafion® membrane with electrodes on either side and placing it in a Carver hot press, Model C. The temperature of the hot-press was then raised to 130 ºC and a pressure of 4000 lbs. was applied for about 2 minutes. The resulting MEA was tested in a 5 cm^2 single cell obtained from Electrochem, Inc., along with HP 6060B DC electronic load box and 6651A DC power supply to measure the polarization characteristics of the single cell. The mass flow rates of H_2 and O_2

were controlled with a FC 2900V mass flow controller (Millipore). The feed gases were bubbled through 1 L stainless bottles containing deionized water for the purpose of humidification. The temperature of the humidification bottles was set at 15 ºC and 10 ºC higher than the fuel cell temperature for the anode and cathode side, respectively, as commonly done.

The open circuit potential V_0 in Eq. 66 was calculated from[11]

$$V_0 = 1.23 - 0.9 \times 10^{-3} \left(T - 298\right) + \frac{RT}{4F} \ln p_{H_2,T}^2 p_{O_2,S} \qquad [78]$$

where T is in K, and the partial pressures are in atmospheres. The partial pressures of hydrogen and oxygen were calculated by subtracting from the total pressure the saturation pressure of water as calculated (in atm.) from[55]

$$\ln p_w^o = 11.676 - \frac{3816.44}{T - 16.13} \qquad [79]$$

It is apparent from Figure III-2 that the comparison between theory and experiments is very good except at very high current densities, due likely to the importance of diffusional limitations in the electrocatalyst layers at high current densities (high reaction rates) and large overpotentials. Of course, diffusional limitations in the catalyst layer have been ignored in this analysis in the interest of obtaining a simple analytical solution. Further, figure III-3 shows a plot of the power density versus voltage for the cell along with theoretical predictions. The optimum in power density at the intermediate voltage is noteworthy and important in determining the operating voltage, which is frequently chosen to be higher than the optimum, i.e., in the range of 0.6 - 0.7 V. Thus, the model adequately describes the fuel cell performance except at high current densities. However, the credibility of the model clearly depends upon the reasonableness of the parameters employed, which is discussed next.

The parameters utilized in the PEM conductivity model, i.e., for the BET equation and the proton-exchange membrane, are those given by Thampan et al. (2000)[6], who also provide adequate justification for these values. These parameter values are, therefore, not further discussed here except to observe that no additional fitted parameters were employed in applying their model of PEM conduction to the fuel cell. In addition, for the Nafion® 115 membrane used for the data here, the membrane thickness is 125 μm.

For the catalytic layers, the Pt particle size of $d_M = 2.9$ nm is taken from the particle size versus ω_M data given by Gloaguen et al. (1994)[56] and in the E-TEK catalog. The parameter $\varphi_M = 0.75$ is adopted since it provides values of catalyst dispersion consistent with the formula of Boudart[57]. For the fraction of the available metal surface in contact with ionomer, it is simply assumed that it is related to the volumetric ionomer loading in the catalyst layer q_I through the Bruggeman relation $\varphi_I = q_I^q$, with the Bruggeman exponent $q = 1.5$. The catalyst layer porosity of 0.5 assumed is in the range adopted by others.

For the hydrogen-oxidation reaction (HOR), the effective transfer coefficient is taken as $\vec{\alpha}_A = 1/2$, which is commonly adopted[14], and the exchange-current density $i^*_{A,0,ref} = 1$ mA/cm^2 of Pt catalyst surface at room temperature[58]. The effective activation energy for HOR is assumed to be $E_{A,\Phi_0} = 18$ kJ/mol[59].

As discussed above, it is found for the oxygen reduction reaction (ORR) in acid solutions that the effective transfer coefficient $\vec{\alpha}_C = 1$ at low cds, while below this voltage (high cds), frequently $\vec{\alpha}_C = 1/2$ is observed[64,60]. Since most of the overpotential occurs at low cds, in this analysis we assume $\vec{\alpha}_C = 1$ at all cds. The change of slope may also be explained on the basis of influence of diffusion control at higher cds[65]. Further support for $\vec{\alpha}_C = 1$ is given by

Parthasarathy et al.[62] determined from the Tafel slope of ORR in Nafion® electrolyte. The activation energy of ORR is assumed to be E_{C,Φ_0} = 76 kJ/mol, as given by Mukerjee and Srinivasan[61]. Parthasarathy et al.[64] also provide an activation energy of E_{C,Φ_0} = 73 kJ/mol. The exchange current densities for ORR reported in the literature[65] are in the range of $i^*_{C,0\,ref} = 10^{-9}$ to 10^{-11} A/cm^2. For example, Parthasarathy et al.[62] give $i^*_{C,0} = 2.2\times 10^{-10}$ A/cm^2 for a Pt microelectrode in contact with Nafion® membrane at 298 K and 1 atm oxygen. They[63] later revised this to $i^*_{C,0} = 8.3\times 10^{-10}$ A/cm^2. Other values reported by this group are: $i^*_{C,0} = 3.25\times 10^{-11}$ A/cm^2 at 30 ºC and $i^*_{C,0} = 3.6\times 10^{-9}$ A/cm^2 at 80 ºC[64] Parthasarathy et al. The above studies were with Pt microelectrode, i.e., a Pt wire was used as electrode. Thus, we adopt the value $i^*_{C,0,ref} = 10^{-11}$ at room temperature and 1 atm oxygen.

For the E-TEK gas-diffusion backing, the porosity of the carbon cloth itself is 0.78. After treatment with Teflon and carbon particles, however, its finished porosity is usually around 0.55 - 0.65. We assume a value of 0.65 for the treated, but uncompressed, E-TEK gas-diffusion backing. Further, the GDB thickness given is 350 μm. The final thickness of the compressed GDB in the assembled fuel cell would, however, depend upon the thickness of the gasket used as well as the torque applied. Thus, Springer et al.[23] assume 180 μm, while Bernardi and Verbrugge[14] assume 260 μm. The gasket thickness used by us is 250 μm. Therefore, this is the thickness assumed for the GDB. It should be mentioned that this is relatively unimportant, as the final compressed porosity and thickness are related, one compensating the other to a large extent. Thus, the final compressed porosity would be $1-[(350/250)(1-0.65)] = 0.5$. The corresponding volumetric water loading in the pores, thus, is assumed to be $q_w = 0.2$ to give a final residual gas pore porosity of 0.4 as assumed by Springer et. al.[23]. It should be mentioned, however, that this value likely depends upon the water supersaturation, i.e., the ratio of vapor pressure in fuel cell to that at the humidifier temperature. The residual gas pore diameter in the wetted GDB is assumed to be 2.1 μm, which is actually the only fitted parameter utilized, but is of the appropriate order[65].

The partition coefficients of hydrogen and oxygen are taken from the literature[14]. For gas phase diffusion coefficients, we use the values calculated by Bernardi and Verbrugge[14] for 353 K, i.e., $D^o_{\mathrm{O_2\text{-}N_2}} = pD_{\mathrm{O_2\text{-}N_2}}$ = 0.279 atm.cm^2/s, $D^o_{\mathrm{w\text{-}O_2}} = pD_{\mathrm{w\text{-}O_2}}$ = 0.370 atm.cm^2/s, $D^o_{w\text{-}\mathrm{N_2}} = pD_{w\text{-}\mathrm{N_2}}$ = 0.387 atm.cm^2/s, and $D^o_{\mathrm{w\text{-}H_2}} = pD_{\mathrm{w\text{-}H_2}}$ = 1.2 atm.cm^2/s, with the following temperature correction employed: $(T/353)^{1.823}$.

It is of interest to determine if the expression for effective diffusion coefficient (Eq. 13) obtained from the complete dusty-gas model can be simplified by dropping the viscous flow or the Knudsen diffusion terms, since in the previous models for PEM fuel cells both these transport mechanisms are usually neglected. Thus, for the case shown in Figure III-2, Eq. 13 provides an effective diffusion coefficient of oxygen through the GDB as 0.01 cm^2/s. If the d'Arcy terms are dropped, Eq. 13 yields an effective diffusion coefficient of 0.0012 cm^2/s. If, on the other hand, the Knudsen diffusion terms are dropped, it provides a value of 0.281 cm^2/s. It is, therefore, evident that the complete dusty-gas treatment for flux through the GDB is called for.

Figure III-4 shows the sensitivity of the model to changes in operating pressure. The cell performance only changes slightly when operated at 1 atm. and 2 atm., however the model simulations change dramatically with pressure. This occurs because the limiting current (Eq. 65) is linear with the partial pressure of O_2.

Figure III-5 shows the comparison between experimental measurements and the reaction-diffusion model, *i.e*. when diffusion is considered in the catalyst layer. The parameters utilized were similar to those shown in Table III-1. Thus this model is successful in capturing the significant aspects of the polarization curve. Unfortunately, this first generation reaction-diffusion model also displays the inaccurate oxygen pressure dependence, which must be addressed in subsequent improvements.

In summary, the values of the various parameters utilized in the model are adopted from the literature and, thus, provide confidence in the adequacy of the theoretical model.

Conclusion

The PEM fuel cell, currently a serious contender for power generation for mobile and stationary applications, is in many ways a membrane reactor, involving a composite of several reaction and membrane layers and embodying the functions of simultaneous catalytic reaction and separation. This paper draws attention to this comparison and utilizes it to develop an analytical model incorporating details of the transport and/or reaction in each layer. The transport model utilized in the various layers is the dusty-fluid model, which is well-suited for describing the proton-exchange membrane as well as the gas-diffusion layers. The proton conductivity in the PEM is influenced by its structure, the sulfonic acid group concentration, percolation threshold, water sorption characteristics, and relative humidity. The transport of gases through the gas-diffusion backing, and hence the limiting current, is affected by its pore size, porosity, thickness, and water content. In the catalyst layers, the electrocatalytic kinetics for the hydrogen oxidation and the oxygen reduction reactions are adopted from the literature. Structural details are included such as the catalyst loading, Pt/C mass fraction, catalyst microcrystallite diameter, and ionomer loading. However, it is assumed that there are no diffusional limitations and no potential drop within the catalyst layers owing to their relative thinness. The resulting model, with parameter values adopted from the literature, captures the essential features of the fuel cell performance well except at high current densities. While it is our intention to improve the Reaction-Diffusion model to better account for effect of the operating cathode O_2 pressure, it is noteworthy that in the range of practical interest (0.7 - 0.8 V), the analytical model is adequate. It should also be mentioned that the model here assumes equimolar counter-diffusion of water and hydronium ion in the PEM, which bears further investigation.

Acknowledgement

The financial support for this work provided by the H Power Corp. under Naval Surface Warfare Center (NSWC) Contract No. N00167-99-C-0002 is gratefully acknowledged. Also acknowledged are contributions of Dr. Hao Tang to this work.

Table III-1. Parameter Values Employed in the Fuel Cell Model

	Parameter	Value	Units/Notes
Proton-Exchange Membrane:	L_B	125	μm
	$\overline{V}_M$	537	cm^3/mol
	$\lambda^0_{\mathrm{H}^+,298}$	349.8	S.cm^2/equiv
	E_μ	14	kJ/mol
	$K_{\mathrm{A,C},298}$	6.2	
	ΔH^o	−52.3	kJ/mol
	λ_0	1.9	
	δ	5.5	
	q	1.5	
BET Parameters:	λ_m	1.8	
	C	150	
	n_w	13.5	
Anode/Cathode Catalyst:	$\vec{\alpha}_A$	1/2	
	$i^*_{A,0,ref}$	10^{-3}	A/cm^2 Pt at 298 K
	E_{A,Φ_0}	18	kJ/mol
	$\vec{\alpha}_C$	1	
	$i^*_{C,0,ref}$	10^{-11}	A/cm^2 Pt at 298 K
	E_{C,Φ_0}	76	kJ/mol
	ω_M	0.2	
	d_M	2.9	nm
	ε_{cat}	0.5	
	m_M	0.4	mg/cm^2
	m_I	0.7	mg/cm^2
	ρ_I	2.1	g/cm^3
Gas-Diffusion Backing:	ε_B	0.5	
	$2a$	2.1	μm
	$L_D = L_E$	250	μm
	κ_{H_2}	0.644	
	κ_{O_2}	0.144	
	q_w	0.2	

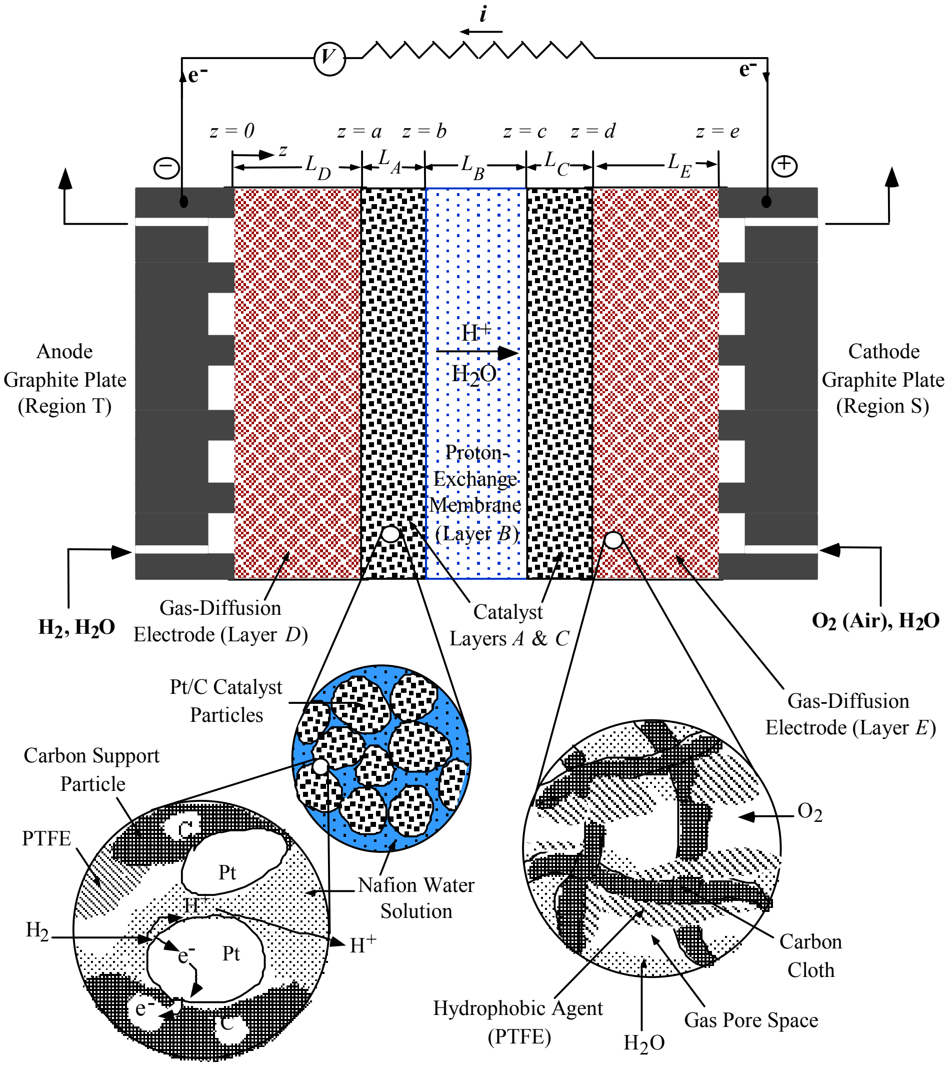

Anode:	$H_2 \rightarrow 2H^+ + 2e^-$
Cathode:	$1/2O_2 + 2H^+ + 2e^- \rightarrow H_2O$
Overall:	$H_2 + 1/2O_2 + \rightarrow H_2O$

Figure III-1. A schematic representation of the PEM fuel cell cross-section consisting of gas-diffusion backing (Layers *D* and *E*), catalyst layers (Layers *A* and *C*), and the proton-exchange membrane (Layer *B*). The gas-diffusion backing fibers are coated with PTFE so as to be not flooded with water, while the catalyst layers comprise ionomer solution among Pt/C particles for proton transport.

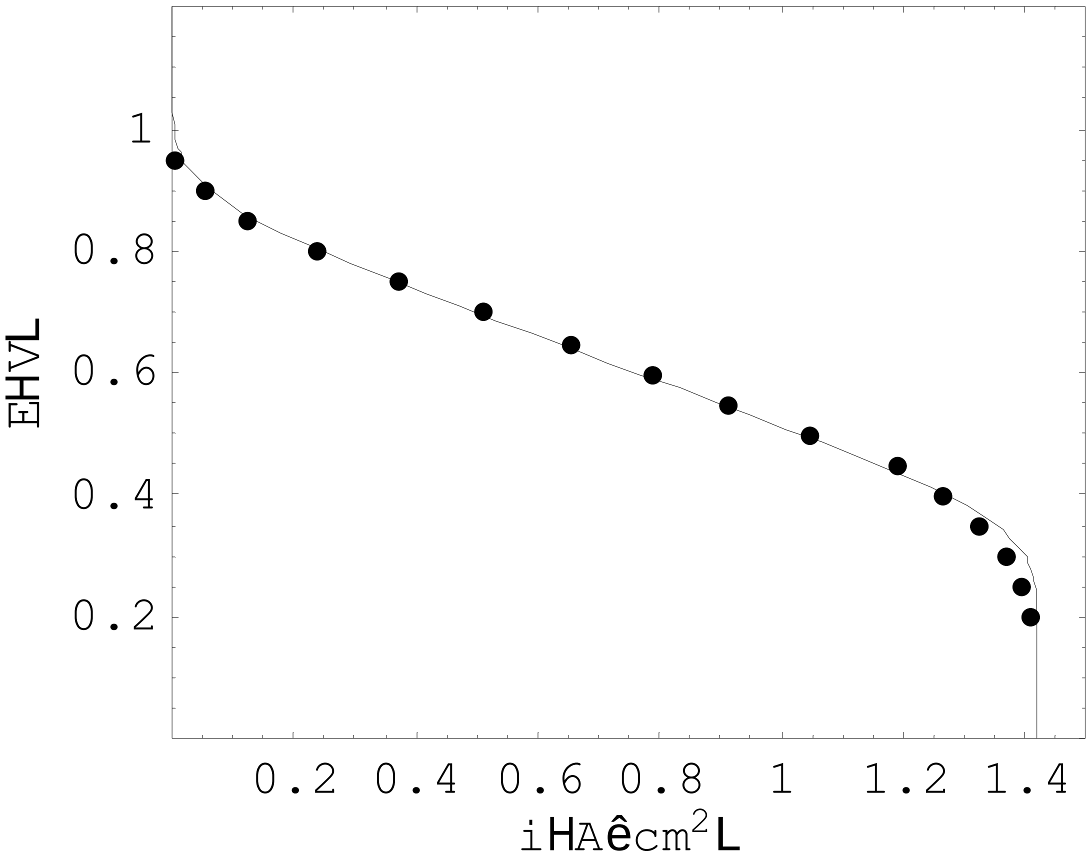

Figure III-2. Comparison of overall fuel cell model (diffusion neglected in catalyst layer) and experimental results. Current density (A/cm^2) versus voltage (V) plot for a 5 cm^2 fuel cell operated at 80 º C with a H_2/O_2 (3/3 atm.) feed; humidifier temperatures of 95 ºC and 90 ºC for anode and cathode, respectively; E-TEK double-sided electrodes with platinum catalyst (ω_M = 0.2 Pt on Vulcan XC-72) loading m_M = 0.4 mg Pt/cm^2 and Nafion® loading m_I = 0.7 mg/cm^2, and with a Nafion® 115 membrane.

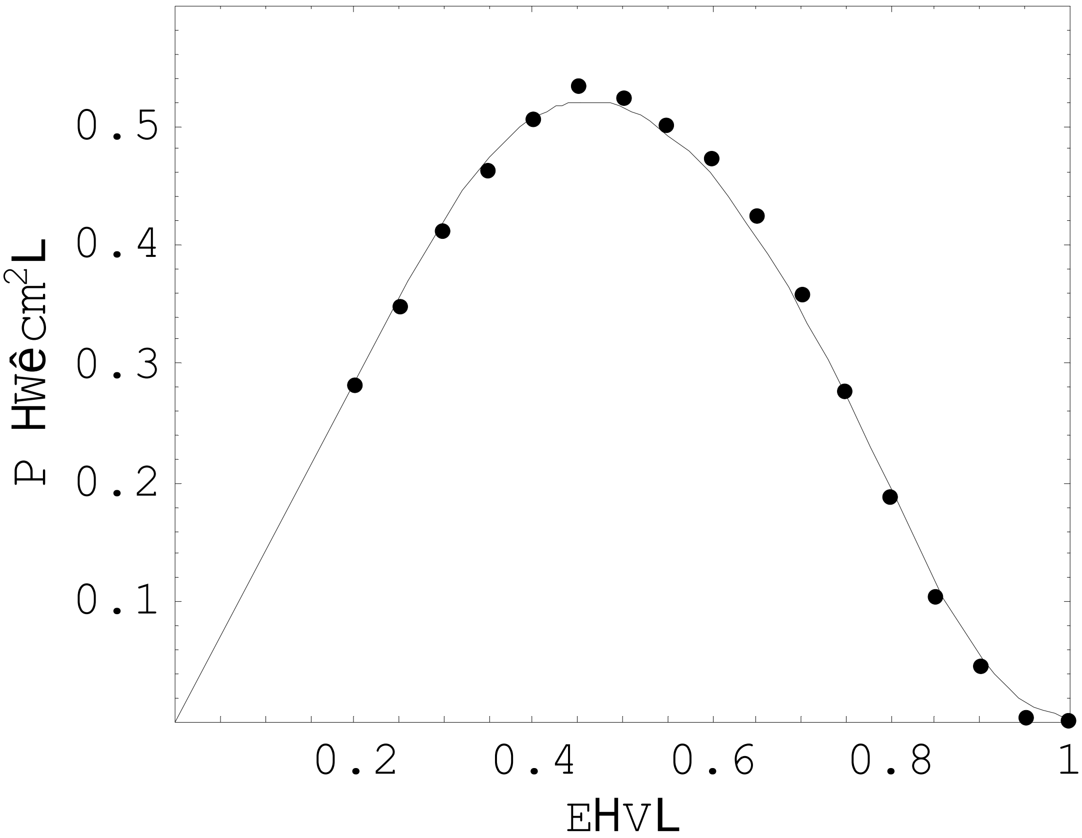

Figure III-3. Comparison of overall fuel cell model (diffusion neglected in catalyst layer) and experimental results. Power density (W/cm^2) versus voltage (V) plot for a 5 cm^2 fuel cell. Conditions are same as those in Figure III-2.

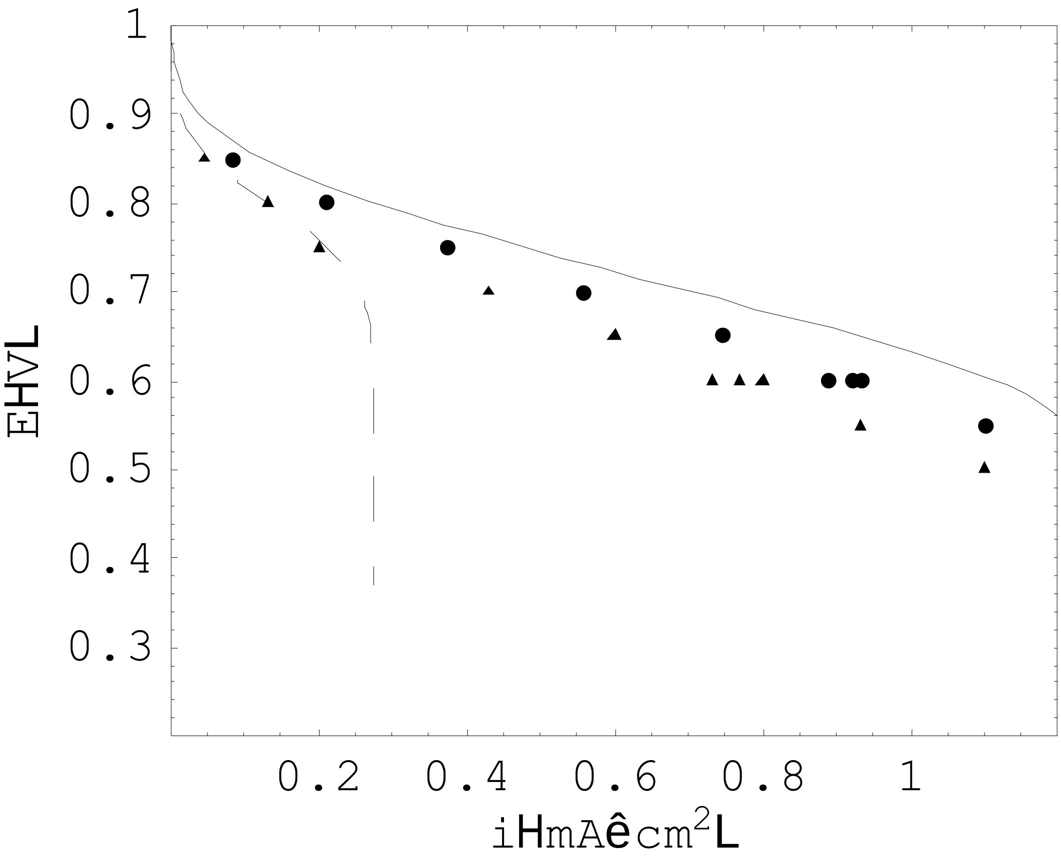

Figure III-4: ● P_{O2} = 1 atm., ▲ P_{O2} = 2 atm.,– – – Sim. at P_{O2} = 1 atm., —— Sim. at P_{O2} = 2 atm. Sensitivity analysis of fuel cell model (diffusion neglected in catalyst layer) model. Current density (A/cm^2) versus voltage (V) plot for a 5 cm^2 fuel cell operated at 70 º C with a H_2/O_2 (2/2 atm) feed and also H_2/O_2 (1/1 atm) feed. Humidifier temperatures of 80 ºC for both anode and cathode, respectively. E-TEK single-sided electrodes with platinum catalyst (ω_M = 0.2 Pt on Vulcan XC-72) loading m_M = 0.4 mg Pt/cm^2 and Nafion® loading m_I = 0.7 mg/cm^2, and with a Nafion® 115 membrane.

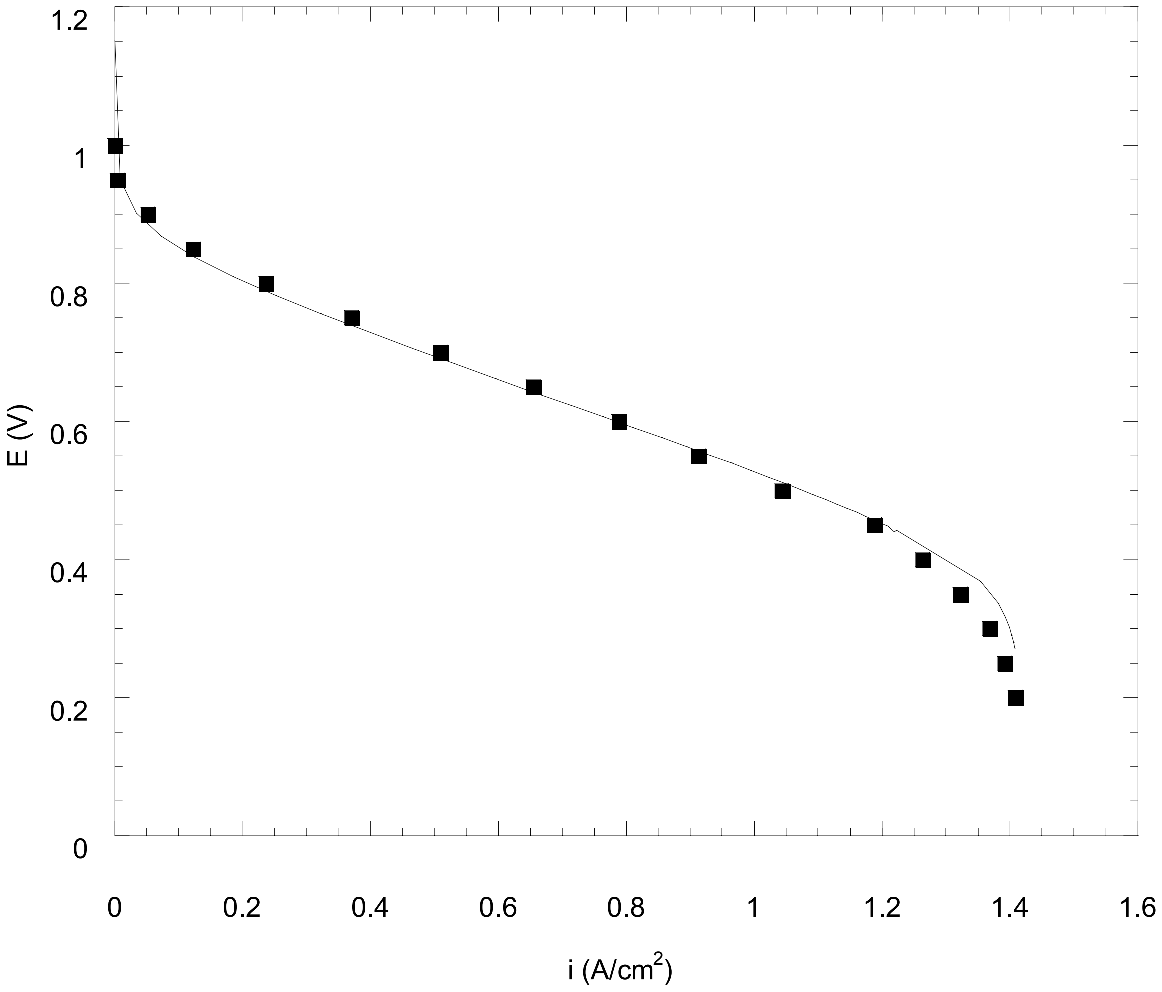

Figure III-5. Comparison of Reaction-Diffusion model (diffusion included in the catalyst layer) vs. experimental results. Current density (A/cm^2) versus voltage (V) plot for a 5 cm^2 fuel cell. Conditions are same as those in Figure III-2.

References

1 M. Jacoby, *C&EN*, p. 31, June 14 (1999).

2 P. Patil and P. Zegers, *J. Power Sources*, **49**, 169 (1994)

3 S. Gottesfeld and T. A Zawodzinski, in R. Alkire, H. Gerischer, D. Kolb, C. Tobias, eds., *Advances in Electrochemical Science and Engineering*, Vol. 5, 197 (1998).

4 L. J. M. Blomen and M. N. Mugerwa, *Fuel Cell Systems*, Plenum, New York (1993).

5 K. V. Kordesh and G. R. Simader, *Fuel Cells and Their Applications*, VCH, Weinheim (1996).

6 T. Thampan, S. Malhotra, H. Tang and R. Datta, *J. Electrochem. Soc.*,**147**, 3242 (2000).

7 S. Gottesfeld and J. Pafford, *J. Electrochem. Soc.*, **135**, 2651 (1988).

8 G. J. K. Acres, J. C. Frost, G. A. Hards, R. J. Potter, T. R. Ralph, D. Thompsett, G. T. Burstein, G. J. Hutchings, *Catal. Today*, **38**, 393 (1997).

9 N. Edwards, S. R. Ellis, J. C. Frost, S. E. Golunski, A. N. J. van Kuelen, N. G. Lindewald, and J. G. Reinkingh, *J. Power Sources*, **71**, 123 (1998).

10 A. G. Dixon, in *Catalysis*, Vol 14, Royal Society of Chemistry, Cambridge, UK (1999)

11 C. Berger, ed., *Handbook of Fuel Cell Technology,* Prentice-Hall, Englewood Cliffs, NJ (1968).

12 T. Erdey-Grúz, *Kinetics of Electrode Processes*, Adam Higler, London, 1972.

13 W. Mitchell, *Fuel Cells*, Academic Press, New York (1963).

14 D. M. Bernardi and M. W. Verbrugge, *AIChE J.*, **37**, 1151 (1991).

15 D. M. Bernardi and M. W. Verbrugge, *J. Electrochem. Soc.*, **139**, 2477 (1992).

16 J. Kim, S. M., Lee, S. Srinivasan, and C. E. Chamberlin, *J. Electrochem. Soc.*, **142**, 2670 (1995).

17 E. R. Gonzalez, *J. Electrochem. Soc.*, **143**, L113 (1996).

18 , J. C. Amphlett, K. A. M. Creber, J. M. Davis, R. F. Mann, B. A. Peppley, and D. M. Stokes, *Int. J. Hydrogen Energy*, **19**, 131 (1994).

19 J. Leddy, and N. E. Vanderborgh, in *Proceedings of the Symposium on Diaphragms, Separators, and Ion-Exchange Membranes*, J. W. Van Zee, R. E. White, K. Kinoshita, and H. S. Burnery, (Eds.), Vol. 86-13, The Electrochemical Society, Pennington, NJ, p. 15 (1986).

20 T. F. Fuller and J. Newman, *J. Electrochem. Soc*., **140**, 1218 (1993).

21 T. V. Nguyen and R. E. White, *J. Electrochem. Soc*., **140**, 2178 (1993).

22 T. E. Springer, M. S. Wilson, and S. Gottesfeld, *J. Electrochem. Soc*., **140**, 3513 (1993).

23 T. E. Springer, T. A. Zawodzinski, M. S. Wilson and S. Gottesfeld, *J. Electrochem. Soc*., **143**, 587 (1996).

24 T. E. Springer, T. Rockward, T. A. Zawodzinski, and S. Gottesfeld, *J. Electrochem. Soc*., **148**, A11-A23 (2001).

25 M. L. Perry, J. Newman and E. J. Cairns, *J. Electrochem. Soc*., **145**, 5 (1998).

26 A. Y. Tonkovich, J. L. Zilka, M. J. LaMont, Y. Wang, and R. S. Wegeng, *Chem. Engng. Sci*., 54, 2947 (1999).

27 V. A. Paganin, E. A. Ticianelli, and E. R. Gonzalez, *J. Appl. Electrochem*., **26**, 297 (1996).

28 D. Raistrick, in *Proceedings of the Symposium on Diaphragms, Separators, and Ion-Exchange Membranes*, J. W. Van Zee, R. E. White, K. Kinoshita, and H. S. Burnery, (Eds.), Vol. 86-13, The Electrochemical Society, Pennington, NJ, p. 172 (1986).

29 M. S. Wilson, and S. Gottesfeld, *J. Electrochem. Soc*., **139**, L28 (1992).

30 W. Grot, in *Encyclopedia of Polymer Science and Engineering*, **16**, 2nd. ed. (1989)

31 T. D. Gierke, G. E. Munn, and F. C, Wilson,.*J. Polym. Sci., Polym. Phys. Ed.* **19,** 1687 (1981).

32 T.D. Gierke, and W.Y. Hsu, *Perfluorinated Ionomer Membrane,* A. Eisenberg, and H. L. Yeager, Editors, American Chemical Society, Washington, DC (1982).

---

33 S. Glasstone, K. J. Laidler, and H. Eyring, *The Theory of Rate Processes*, McGraw-Hill, New York, p. 552, 1941.

34 J. O'M Bockris, and A. K. N. Reddy, *Modern Electrochemistry*, Vol. 2, Plenum, New York, 1970.

35 E. A. Mason, and A. P. Malinauskas, *Gas Transport in Porous Media: The Dusty-Gas Model*, p. 142, Elsevier, Amsterdam (1983).

36 S. J. Ridge, R. E. White, Y. Tsou, R. N. Beaver, and G. A. Eisman, *J. Electrochem. Soc.*, **136**, 1902 (1989).

37 K. R. Weisbrod, S. A. Grot, and N. E. Vanderborgh, in *Proceedings of the First International Symposium on Proton Conducting Membrane Fuel Cells I*, S., Gottesfeld, G. Halpert, and A. Landgrebe, (Eds.), Vol. 95-23, The Electrochemical Society, Pennington, NJ, p. 152 (1995).

38 E. A. Mason, and A. P. Malinauskas., *Gas Transport in Porous Media: The Dusty-Gas Model*, p. 142, Elsevier, Amsterdam (1983).

39. R. Datta, and R. G. Rinker, *J. Catal.*, **95**, 181 (1985).

40 R. Jackson, *Transport in Porous Catalysts*, Elsevier, Amsterdam (1977).

41 A. W. Adamson, and A. P. Gast, *Physical Chemistry of Surfaces*, 6th ed., p.622, Wiley Interscience, New York (1997).

42 K. A. Connors, *Chemical Kinetics: The Study of Reaction Rates in Solution*, VCH Pub., New York (1990).

43 A. Damjanovic, and V. Brusic, *Electrochim. Acta*, 12, 615 (1967).

44 M. Enyo, in *Comprehensive Treatise of Electrochemistry*, B. E. Conway, J. O'M. Bockris, E. Yeager, S. U. M. Khan, and R. E. White, Editors, Plenum, NewYork, p. 241 (1983).

45 T. F. Fuller, *Solid-Polymer-Electrolyte Fuel Cells*, Ph.D. Thesis, University of California, Berkeley (1992).

46 W. Vogel, J. Lundquist, P. Ross and P. Stonehart, *Electrochim. Acta*, **20**, 79 (1975).

47 J. Lipkowski and P. N. Ross, *Electrocatalysis*, Wiley-VCH, New York (1998).

48 P. N. Ross in J. Lipkowski and P. N. Ross, eds., *Electrocatalysis*, Wiley-VCH, New York, p. 43 (1998).

49 E. B. Sepa, M. V. Vojnovic and A. Damjanovic, *Electrochim. Acta*, **26**, 781 (1981).

50 D. B. Sepa, M. V. Vojnovic and Lj. M.Vracar, *Electrochim. Acta*, **32**, 129 (1987).

51 S., Dechapanichkul, *Porous-Walled Tubular Catalytic Reactor Separator*, Ph.D. Thesis, The University of Iowa, Iowa City (1994).

52 J. S. Kim, and R. Datta, *AIChE J*, **37**, 1657 (1991).

53 K. Kanamura, H. Morikawa and T. Umegaki, *J. Electrochem. Soc*., **150(2)**, A193 (2003).

54 H.S. Fogler, *Elements Of Chemical Reaction Engineering*, 3rd Ed., Prentice Hall, Upper Saddle River, N.J., 1999, p. 743.

55 R. C., Reid, J. M., Prausnitz, and T. K., Sherwood, *The Properties of Gases and Liquids*, 3rd. ed., McGraw-Hill, NY (1977).

56 F. Gloaguen, F. Andolfatto, R. Durand, and P. Ozil, *J. Appl. Electrochem*., **24**, 863 (1994).

57. M. Boudart, and G. Djéga-Mariadassou, *Kinetics of Heterogeneous Catalytic Reactions*, Princeton University Press, Princeton, NJ (1984).

58 S. Gottesfeld and J. Pafford, *J. Electrochem. Soc*., **135**, 2651 (1988).

59 N. M. Markovic B. N. Grugr and P. N. Ross, *J. Phys. Chem*., 101, 5405 (1997).

60 E. B. Sepa, M. V. Vojnovic and A. Damjanovic, *Electrochim. Acta*, **26**, 781 (1981).

61 S. Mukerjee and S. Srinivasan, *J. Electroanal. Chem*., **357**, 201 (1993).

62 A. Parthasarathy, C. R. Martin and S. Srinivasan, *J. Electrochem. Soc*., **138**, 916 (1991).

63 A. Parthasarathy, B. Dave, S. Srinivasan, A. J. Appleby, and C. R. Martin, *J. Electrochem. Soc*., **139**, 1634 (1992a).

64 A. Parthasarathy, S. Srinivasan, A. J. Appleby and C. R. Martin, *J. Electrochem. Soc*., **139**, 2530 (1992b).

65 K. Kinoshita, *Electrochemical Oxygen Technology*, John Wiley, New York (1992).

IV. RATIONAL DESIGN OF HIGHER TEMPERATURE COMPOSITE PROTON EXCHANGE MEMBRANES[#]

Abstract

The design of higher temperature proton-exchange membranes (PEMs) with stable performance under low relative humidity (RH) conditions is desirable and considered here based on previous experimental and theoretical work. The design of composite membranes is based on enhancing the acidity and water sorption properties of a conventional PEM by impregnating it with a solid superacid. A systematic investigation of the composite Nafion®/inorganic PEMs comprising experimental results of water uptake, ion-exchange capacity (IEC), conductivity and fuel cell polarization is presented. Particle size, chemical treatment, dopant loading and process operating conditions are investigated. The most promising candidate investigated thus far is the nano-structured ZrO_2/Nafion® PEM which exhibited an increase in the IEC, a 40% increase in water sorbed and a resulting 24% conductivity enhancement vs. unmodified Nafion® 112 at 120°C and 40% RH.

Introduction

The development of a proton-exchange membrane (PEM) that has high proton conductivity at higher temperature and lower relative humidity (RH) conditions than those suited for the standard PEM would aid in the commercialization and large scale deployment of PEM fuel cells, a significant step toward environmentally friendly and sustainable power generation. Operation at higher temperature and lower RH allows a simplification in water management and gas purification systems while simultaneously

---

[#] The Contributions of N. H. Jalani and R. Datta are gratefully acknowledged.

raising power plant efficiency. It is also a very challenging endeavor, as evident by the present lack of suitable higher temperature PEMs despite intensive world-wide research efforts.

This paper presents a rational approach toward the design of higher temperature PEMs based on previous experimental and modeling work. Promising composite PEMs were fabricated based on this approach, although corresponding PEM fuel cell performance has yet to be demonstrated. This work demonstrates the promise of inorganic composite PEMs in order to further enhance PEM conductivity at higher temperatures and low RH.

Before undertaking a discussion of this approach, however it is useful to review previous approaches.

Review of Previous Higher Temperature PEM Development

Perfluorinated PEMs

As there are comprehensive reviews available on the development and properties of perfluorinated ion containing polymers or ionomers[1,2,3], only a brief description is provided here. Although perfluorinated PEMs are costly to produce and potentially difficult to recycle/dispose in an environmentally friendly manner, their resistance to the Pt catalyzed oxidative degradation in H_2-O_2 fuel cells makes them the material of choice for most PEM fuel cell applications. One of the earliest perfluorinated PEMs commercialized was Nafion® (Figure IV-1a) and has demonstrated fuel cell lifetime of over 60 000 hrs at 80°C[4], unfortunately higher temperature lifetime studies are not reported in the literature. This polymer is prepared by the co-polymerization of tetra-fluoro ethylene, or TFE (C_2F_4, MW = 100) and perfluoro 3,6-dioxa-4-methyl-7-octenen sulfonyl fluoride (CF_2=CFO-C_3F_6-O-C_2F_4-SO_2F, MW = 446)[5]. The meltfabricable precursor polymer is then extruded and laminated into the desired shape and thickness, hydrolyzed with NaOH and subsequently protonated by HNO_3. The resulting equivalent weight (EW) is 1100 g/mol. H^+ and the thickness ranges from 50 μm to 170 μm for commercially available Nafion®. The PTFE backbone enhances the mechanical strength of the PEM albeit at the cost of lower water sorption. The PEM can be divided into three different regions: the hydrophobic PTFE backbone, the hydrophilic ionic zone which is composed of the ionic clusters and the intermediate region[6].

A number of other perfluorinated membranes have also been produced commercially. The Dow® membrane has a shorter side chain than Nafion® but has similar structural and morphological properties[7]. Both Aciplex-S® and Flemion®, available from Ashai Chemical and Ashai Glass Company, respectively, are long side chain perfluorosulfonated membranes demonstrating cell performance similar to Nafion®. Other perfluorinated PEMs have been developed by modification of the side chain[8,9,10]. DesMarteau[9,11] replaced the sulfonic acid group ($-SO_3H$) in Nafion® with a sulfonyl imide group ($-SO_2NHSO_2CF_3$), which resulted in an increase in the water uptake while Kotov et al.[10] substituted a phosphonic acid group that has the potential for higher thermal stability.

Furthermore partially fluorinated PEMs such as the sulfonated trifluorostyrene membranes[12] also exist. Ballard Power Systems has developed BAM3G[13] (Figure IV-1b), a novel family of PEMs with equivalent weights 375 to 920, by incorporating a, β, β-trifluorostyrene monomer and a series of substituted- a, β, β-trifluorostyrene comonomers. The high temperature performance of these PEMs is yet unproven.

Alternatively partially fluorinated PEMs may be produced by radiation grafting. This involves irradiating the polymer backbone (e.g. poly(tetrafluoroethylene (PTFE), poly(fluorovinylidene) (PVDF)) with an electron beam to produce reactive radicals. These active sites allow the grafting of monomer units (poly(styrenesulfonic acid) PSA) resulting in a novel polymer, that after sulfation produces a PEM. Brack et al.[14] showed that radiation grafted copolymers from para-sulfonated PSA and poly(ethylene-tetrafluoroethylene) (ETFE) exhibit high conductivity at 60°C, but the high temperature potential of these PEMs is poor due to the degradation of the polystyrene component.

Unfortunately, the conductivities of all the above membranes strongly depend upon the hydration state of the membrane[15]. This occurs because virtually all proton transport in low temperature membranes occurs in the liquid phase via protonation of the solvent by pendant acid followed by conduction via the Grotthus and bulk diffusion mechanisms. When the operating conditions increase above 100°C at atmospheric pressure, the conductivity decreases dramatically due to the lower water content at the lower RH. In fact, virtually all solid proton conductors with adequate conductivity can be separated into two major temperature ranges[8]: (*i*) For temperatures ≤ 100°C, the conventional Solid Polymer Electrolytes (SPE), and (*ii*) For temperatures ≥ 800°C, e.g. oxygen-deficient perovskite such as $Ba_2YSnO_{5.5}$[16,17].

Since the intermediate temperature range between these extremes offers the benefits of quick start up, facile integration with balance of plant equipment and increased CO tolerance, it is important to develop solid state proton conductors in the temperature range of 100°C - 300°C. To overcome the dearth of suitable materials available in this range of temperature, developmental efforts have been focused on three alternate approaches:

1. Use of alternate solvents with lower volatility than water;
2. Development of new class of polymer/solid state protonic materials;
3. Modification of existing SPEs, e.g., composite inorganic/organic PEMs.

A brief description of the first two approaches is given before describing the third approach, which is followed in this work.

Use of alternate solvents with lower volatility

A possible procedure for increasing the operating temperature of the PEM at low relative humidity is to replace water for solvating the protons with a lower volatility solvent. The development of anhydrous PEMs with low electro-osmotic drag would allow higher temperature operation in dry conditions. Savinell et. al.[18] have pioneered this approach. They utilized H_3PO_4 doped Nafion® and were able to develop a PEM with high conductivity at elevated temperatures. However H_3PO_4 is highly corrosive and has a finite volatility at elevated temperatures and due to its solubility would eventually leach out with exhaust liquid water, causing a performance decline and corrosion issues.

Similarly Doyle et. al.[19] demonstrated that Nafion® imbibed with ionic liquids such as the molten salt 1-Butly, 3-methyl imidazolium triflate (BMITf) showed good conductivity at high temperature. Unfortunately, the challenge of complete immobilization of the liquid must first be addressed to ensure stable cell performance over extended periods.

Development of alternate polymer/inorganic protonic materials

The development of alternate proton conductors includes hydrocarbon based polymers and inorganic materials that not only provide the potential for high temperature performance at low RH, but also promise a cost advantage[20,21]. The early research with hydrocarbon PEMs was abandoned due to their unacceptable short life spans in the highly oxidizing PEM fuel cell conditions. However, the development of novel aromatic hydrocarbon polymers has made fuel cell application appear more promising[22]. Some of the hydrocarbon based polymers being investigated are poly(oxy-1,4-phenyleneoxy-1,4-phenylenecarbonyl-1,4-pheneylene) or polyether ether ketone (PEEK), poly(4-benzoyl-1,4-phenylene) (PPBP), sulfonated poly(phenylene sulfide), alkylsulfonated polybenzimidazol (AS-PBI) and sulfoarylated PBI[20].

McGrath et. al. have presented high performance MEA results utilizing poly(arylene ether sulfone) (Figure IV-1c) PEMs[23]. They cast films that showed high water uptake and conductivity and are also modifying the copolymer for higher temperature operation by blending it with highly conductive inorganic materials[24].

Among the more promising membranes, Savinell et. al.[25] fabricated a PBI/H_3PO_4 acid complex membrane that showed conductivity of 0.04 S/cm at 190°C at a RH of 10%, and an electro-osmotic drag of almost zero, indicating only small amounts of water are necessary for conduction. However, it is not clear whether H_3PO_4 is fully immobilized in the polymer.

Zaidi et. al.[26] embedded heteropolyacids to different extents in sulfonated polyether ether ketone (S-PEEK). The highest performing composite was a tungstophosphoric acid doped, 80% sulfated PEEK PEM. It showed conductivity similar to that of Nafion® with no degradation in conductivity.

Inorganic Membranes

Although some inorganic materials show conductivity comparable to the state of the art PEMs, such as the water soluble heteropoly acids $H_3PW_{12}O_{40}\cdot 29H_2O$ and $H_3PMo_{12}O_{40}\cdot 29H_2O$ (which have room temperature conductivities of 0.18 S/cm[27]), the majority of these solid state materials have conductivity substantially lower than the polymeric materials. One method to overcome the low conductivity is to fabricate ultra thin membranes. Thus Vichi et. al.[28] have reported the synthesis of nanopore metal oxide membranes via a sol-gel process with a thickness of about 500 nm. However for MEA durability purposes overcoming the brittle nature of these ceramic membranes may be a challenge.

Modification of existing PEMs

It has been previously reported that the incorporation of solid superacids (e.g., heteropolyacids, or oxides) in the conventional polymeric ion-exchange membranes such as Nafion® enhances their protonic conductivity at higher temperatures and at lower humidity levels[29]. In an early study, Malhotra and Datta[29] doped Nafion® membranes with heteropolyacids, e.g. phosphotungstic acid (PTA), and were able to maintain high cell performance at low RH and elevated temperature (120°C). The improved performance was ascribed to the presence of PTA that provides high proton concentrations and improved water retention, but without the associated volatility constraint. Unfortunately, due to the high water solubility of PTA, the PTA eventually leaches from the PEM[30], leading finally to performance similar to un-modified Nafion®.

To decrease the humidification requirements of PEMs, Watanabe et al.[31,32,33] modified Nafion® PEMs by the incorporation of nano-sized particles of SiO_2, TiO_2, Pt, Pt-SiO_2 and Pt-TiO_2. These modified PEMs showed a much higher water uptake, almost 3 times as much as the untreated PEM at 60°C in 100% RH[32]. Although high temperature performance was not reported, when operated at 80°C in a low humidification PEMFC, the modified PEMs showed a decrease in resistance of almost 2 orders of magnitude vs. Nafion®. This improvement was attributed to the suppression of H_2 cross over by Pt and to the subsequent sorption of the water produced on the oxides.

Based on the above pioneering studies, there is now a great deal of effort along the lines of development of organic-inorganic composites[34,35,36,37]. Adjemian et. al.[38,39] introduced nanosized SiO_2 into Nafion® pores[40] and tested various thickness and EW membranes. The benefit of these composite membranes appears to be in significantly longer operation versus conventional Nafion® at a cell temperature of 130°C, humidifier temperature of 130°C and 3 atm. The investigators also noted that the unmodified PEMs showed thermal degradation, while the SiO_2 modified PEMs did not show such irreversible damage. Costamagna et al.[34] incorporated zirconium phosphate into a Nafion 115 membrane[41] and the results obtained are similar to those with the SiO_2.

According to the work described above, the reasons for the improvement in performance are:

1.) Lower gas cross over: The presence of a dopant in the pores increases the diffusional resistance to gas transport through the membrane. The cross over current measured with the modified membrane is an order of magnitude lower than that of the unmodified PEMs. Further by incorporating Pt in the PEM any cross-over gas maybe reacted to produce water *insitu*.
2.) Higher water retention in the PEM: The presence of a hygroscopic additive binds a larger amount of water in the membrane, lowering the partial pressure above the membrane for a given water content.
3.) Improved electrode kinetics: Due to the increased water retention in the modified PEM, the catalyst layer in the electrode is also better hydrated. Thus, an extended reaction zone maybe available when the catalyst layer is appropriately humidified,[42] resulting in better electrode performance at high temperature. Additionally, if the additive does not reduce the catalyst activity, it can be incorporated within the catalyst layer to further extend the reaction zone.

Theoretical Basis of Design of Higher Temperature Composite PEMs

To understand the various factors involved in the design of a high temperature composite Nafion® based PEM, it is beneficial to develop a quantitative model to describe the conductivity of composite PEMs. Thus a theoretical model was developed based on our previous work[43] that simulated the transport of protons through a Nafion® membrane at different temperatures and RHs. This transport model is based on the dusty fluid model (DFM)[44], where the obstruction presented by the polymer matrix to proton diffusion is simply viewed as an additional diffusional interaction with another species, namely, large immobile “dust” particles. In this framework it is appropriate to include the additive as an additional dust species immobilized within the polymer matrix. This viewpoint is depicted in Figure IV-2. The space filling and tortuosity variation of the thus modified matrix are included in the structural constants of the DFM model.

The final form of the expression that describes the proton conductivity of a composite PEM (σ) is

$$\sigma = \left(\varepsilon - \varepsilon_0\right)^q \left(\frac{\lambda_1^0}{1+\delta_{AH}+\delta_{ZH}}\right)\left(c_{AH,0}\alpha_{AH} + c_{ZH,0}\alpha_{ZH}\right) \qquad (1)$$

with

$$\delta_{AH} = \frac{D_{12}}{D_{1M}}\text{; and } \delta_{ZH} = \frac{D_{12}}{D_{1Z}}$$

where D_{12}, D_{1M} and D_{1Z} are the diffusion coefficients for the charge carrier assumed (H_3O^+)/solvent (H_2O), H_3O^+/PEM matrix and H_3O^+/additive particle, respectively. ε and ε_0 are the volume fraction of water in the membrane and the percolation threshold respectively. ε is a function of the water uptake of the PEM (λ) and the partial molar volume of the PEM ($\bar{V}_M \approx \frac{\text{EW}}{\rho_{M,Dry}}$)

$$\varepsilon = \frac{\lambda}{\frac{\bar{V}_M}{\bar{V}_{\mathrm{H_2O}}} + \lambda} \qquad (2)$$

ε_0 is defined in a similar manner, based on the water uptake at monolayer coverage. The Bruggeman or critical exponent q=1.5, and λ_1^0 is the equivalent conductance of a proton in water[43]. The solvent uptake can be predicted with either the finite layer BET isotherm provided by Thampan et. al[43] or by the more sophisticated approaches developed by Choi and Datta recently[45]. Thus at low RH, the water uptake of the PEM is low and the resulting low ε results in poor conductivity. The water uptake and the conductivity rise quickly above RH 70% or so.

The concentration of acid sites available within the PEM is the sum of the polymeric acid sites $c_{AH,0}$ and the dopant acid sites $c_{ZH,0}$. Of course these sites only contribute to the conductivity when the protons are dissociated in the presence of water. The extent of dissociation depends upon the level of hydration and the strength of the acid groups, and is denoted as α_{AH} and α_{ZH} for the polymer and the additive, respectively[43].

Thus, in the design of composite PEMs, the objective of increased PEM conductivity at low RH can be achieved by the presence of hygroscopic additives with high acidity since:

1. The presence of a hydrophilic dopant will increase the water uptake of the PEM at low RH, as shown in Figure IV-3. The equilibrium content of water in the membrane is shifted to higher values at the same vapor activity, because water is bound more strongly to the dopant, and
2. The presence of acidity on the dopants will increase the total number of acid sites available within the PEM. This will enhance the conductivity because the number of charge carriers available will also increase (Eq. 1).

Additionally the additive must be selected so that can be immobilized within the polymer matrix, is compatible with the electro-catalyst, and can maintain/increase the thermo-mechanical properties of the polymer at higher temperature. Thus materials that may leach or poison the membrane or electro-catalyst are not useful. Another factor affecting performance is that since the acid dissociation constants decline with temperature, the degree of dissociation and hence the number of charge carriers decline at higher temperatures[43]. It must also be noted that the particle size of the additive particles ('dust') is important as they form an additional diffusional barrier to the transport of protons (Eq. 1).

Potential Inorganic Additives

Although there exist numerous liquid superacids such as the magic acids (mixtures of HSO_3F and SbF_5; H_0 = -20) which can enhance conductivity, they are unsuitable for fuel cell applications as it is a challenge to permanently immobolize them in the PEM. Thus, the primary interest is in solid superacids. The heteropolyacids are an example of a class worth investigating as they demonstrate high acidity and are extremely hydrophilic, unfortunately they have high solubility in water. Their properties could be utilised if they could be anchored within the polymer matrix.

The sulfated metal oxides, such as TiO_2, ZrO_2, and Fe_2O_3, have become subjects of intensive catalytic studies because these strong superacids are thermally more stable than other solid superacids[46]. Currently, sulfated Zirconia (SO_4^{2-}/ZrO_2) is the strongest superacid among all known solids ($H_0 < -16$) [47]. It retains the sulfonic acid groups, responsible for proton conduction, till about 500°C. As SO_4^{2-}/ZrO_2 exhibits the highest acidity of all the solid superacids[48], the additives selected in the study were based on Zirconia.

Experimental

The experimental methods involved additive synthesis, composite membrane fabrication, and PEM characterization.

Zirconia Particle Preparation

The SO_4^{2-}/ZrO_2 particles were synthesized based on Arata's work on metal oxides[49]. ZrOH powder (MEI Chemicals, Flemington, NJ) was stirred in 0.5M H_2SO_4 for 15 minutes at room temperature. The acid was decanted and the remaining powder dried at 100°C overnight. The dried powder was then calcined in air at 600°C for 2 hrs and the resulting particles were crushed with a mortar and pestle. These particles are denoted as "SO_4/ZrO_2".

Particles were also prepared from a colloidal solution of 20 wt. % ZrO_2/Acetic Acid (Nyacol Nano. Technologies, Ashland MA). The solution was evaporated and the ZrO_2 precipitate was obtained. This precipitate is denoted as "ZrO_2". The precipitate was heated in 6M H_2SO_4, in order to sulfate, then dried at 120°C for 2 hrs and finally calcined in air at 600°C for an additional 2 hrs. The resulting particles were crushed with a mortar and pestle, and are denoted as "ZrO_2 (A)". Additionally a sample of the ZrO_2 (A) was pulverized with a Jet Mill (Laboratory Jet Mill, Clifton NJ) to obtain a reduction in the particle size. This sample is denoted as "ZrO_2 (AP)".

Cast Membranes

Based on experimental procedures described in literature[50], the protocol described below was established to produce uniform and reproducible cast PEMs. To obtain the desired weight loading of additive in the PEM, selected additive particles were dispersed in a 23 wt% Nafion®/ethanol solution with a magnetic stirrer. After stirring for 8 hours, the solution was cast as a PEM on a glass dish utilizing a doctor blade. The cast membrane was placed in a convection oven at 100°C for 15 minutes, which was sufficient to produce a solid membrane. The PEM was removed from the glass dish with DI water, dried and then annealed in a teflon sleeve at 170°C at 10 Tons for 15 minutes in a mechanical press (Carver Model C, Wabash IN). This processing step was necessary to produce pliant, insoluble PEMs with mechanical properties similar to commercially available Nafion® films. The resulting cast PEM has thickness of ~ 50 μm.

Sol-gel ZrO_2/Nafion® Composite PEMs

The final method of preparation of a ZrO_2 composite PEM was via *insitu* sol-gel chemistry based on methods developed by Mauritz's group for the synthesis of asymmetric ZrO_2/Nafion® composites[51]. The host PEM serves as a template that directs the morphology and particle size of the oxide in the PEM matrix, resulting in nano-sized particles[52].

As received Nafion® membranes (Sigma-Aldrich Corp., St. Louis MO) were purified as the hydrolysis and condensation reactions of zirconium alkoxides occur rapidly[53]. The membranes were boiled in 3 wt % H_2O_2 for 1 hr. and then rinsed in water. They were then immersed in 50 % vol. HNO_3/H_2O and heated for 6 hrs, rinsed in water, and then heated in 50 % vol. H_2SO4/H_2O for an additional 6 hrs. The PEMs are boiled in water for 1 hour and then rinsed and washed in water several times to ensure complete removal of any residual acid.

The purified membranes were then placed in a vacuum oven and heat treated at 110°C for 12 hours. The membranes were then boiled in H_2O for 1 hour and then dried at 50°C for 4 hours. The membrane was then immersed in 10:1 ethanol/H_2O solution for an additional hour. The ethanol/ H_2O mixture served to further swell the pores of the PEM to maximize the adsorption of the zirconium alkoxide solution. The membrane was then removed, immersed into a 20:1 (v/v) ethanol:zirconium tert butoxide solution for 10 minutes and then rinsed in ethanol in an attempt to remove surface bound ZrO_2.

The membranes were then removed and heated at 110°C in vacuum for 24hrs to complete the condensation reactions. This composite PEM is denoted as "Nafion® ZrO_2 sol-gel".

Water Uptake Measurements

To measure the water uptake of the composite PEMs a Tapered Element Osscilating Microbalance (TEOM® Series 1500 PMA Reaction Kinetics Analyzer, Rupprecht & Patashnick Co., Inc. Albany, NY) was utilized which has been described elsewhere[54]. The mass change was measured as the frequency change in the tapered element oscillation. The instrument has measurement sensitivity of 1 µg upto a temperature range of 700°C while the sensitivity required for water uptake mass measurements is 1mg. Thus, this instrument is very well suited for water uptake at various temperatures. The RH is controlled by mixing metered flows of wet gas (saturated with H_2O) and a dry gas. This was calibrated with a RH meter (FH A646-R, ALMEMO, Ahlborn, Munich, Germany).

PEMs were cut into thin strips (1.5 mm by 1.5 mm) and packed with quartz wool into the oscillating glass chamber of the TEOM®. The water uptake was measured at 25°C and 90°C from 0 % to 90 % RH, and at 120°C from 0% RH to 40% RH. After the sample was loaded, it was exposed to a stream containing the desired RH, and the real time mass change was observed to determine when the equilibrium amount of water had been adsorbed onto the membrane.

Ion-Exchange Capacity Measurements[55]

A 0.2 g sample of the PEM was exchanged with NH_4^+ by immersing the sample in 1M ammonium acetate for 24 hrs and then in ammonium chloride for an additional hour. The PEM was then washed with DI water to remove any excess NH_4^+ ions. To ensure excess NH_4^+ had been removed, a drop of 1M silver nitrate was added to the wash. If NH_4^+ are present, a white precipitate will form. The PEM was then stored in 50 ml DI water. Adding 2ml of 5M NaOH solution to the sample, forced the subsequent exchange of NH_4^+. Utilizing a calibrated ammonia electrode (Model 95-12 ORION, Boston MA), the amount of ammonia can be accurately quantified thus providing a measure of the ion-exchange capacity based on the amount of NH_4^+ measured.

Conductivity Testing

A membrane sample was clamped in a conductivity cell[24] and then placed in a humidity controlled chamber. The humidity of the chamber was monitored utilizing a dewpoint/temperature probe (HMP 238, Vaisala, Woburn, MA). An air stream was saturated with water by bubbling the dry gas through a humidifier, this wet stream was heat traced to the chamber to avoid condensation. The chamber and the humidifier were both heated to 90°C and 120°C respectively to obtain the necessary partial pressures of water. By metering the flows of the wet and dry stream into the chamber, the RH was controlled. The conductivity of the PEM was measured at 90°C in the RH range from 10% to 90%, while at 120°C the RH range was from 10% to 40%.

The conductivity measurements were made with a perturbation voltage of 10mV in the frequency range 0.01 Hz to 10^6 Hz using a Solartron SI 1260 FRA (Solartron, Hampshire, U.K.) in the X-Y plane. Both real and imaginary components of the impedance were measured and the real Z axis intercept was closely approximated to provide an estimate of the membrane resistance, and hence, conductivity[15]. Additionally samples were sent to an independent evaluator to measure conductivity in the Z-plane which is the orientation of interest.

MEA Testing

The electrodes utilized are commercially available from E-TEK (Somerset, NJ). The type selected was the single sided ELAT® gas-diffusion electrode (20% Pt-on-C, 0.35~0.4 mg Pt/cm^2). The active layer of electrode was brushed with 5% Nafion® solution (0.6 ~0.8mg/cm^2). This electrode was placed on either side of the PEM and the resulting membrane-electrode assembly (MEA) placed in a hot press. The temperature of the hot press was then raised to 130°C and a pressure of 272 atm applied for 120s. The MEA thus prepared was mounted in a 5 cm^2 fuel cell test fixture, obtained from Fuel Cell Technolgies (Los Alamos, NM). The cell was fed with humidified H_2 and O_2 or air supplied at pressure 1 ~3 atm utilizing electronic mass flow controllers (MKS Model No. 1179A22CS1BV-S, Andover, MA) and as controlled by the electronic load (Series 890B

Fuel Cell Test System, Scribner Associates Inc. Southern Pines, NC). Utilizing software (Fuel Cell Test Software Version 2.0, Scribner Associates, Inc.) the mass flow rate of the feed gas was set to stoichiometry dependent flow rates. The load has the inbuilt feature to measure *insitu* MEA ohmic resistance utilizing a current interrupt method.

The pressure of the reactant gases was monitored using pressure gages (Matheson, Model No. 63-5612). Back pressure regulators (Tescom Model No. 44-2300) were used at the outlet of both the anode and the cathode to control the gas pressure. Humidification of the cell was accomplished by bubbling the feeds through stainless steel cylinders containing DI water, with a sight glass to indicate the level of water. Heating tape was wrapped around the feed lines to prevent any condensation in the lines, and water traps were added to facilitate removal of water. The temperature of the humidifiers as well as that of the fuel cell was controlled using individual temperature controllers (Omega CN9100A).

The following MEA test protocol was utilized[56]. The start up involved bringing the humidifier temperature up to a set value of 80°C, then increasing the test fixture to 70°C and operating the fixture on 1 atm H_2 and Air at current controlled mass flow rates, being 1.3 x (anode stoichiometric flow) for H_2 and 2.0 x (cathode stoichiometric flow) for air. The load was cycled for additional 6 hours and then a constant voltage polarization curve was taken. Thereupon another 12 hours of break-in period was utilized and then a final polarization curve was obtained. The electrochemical surface area (ECA) and the crossover were then measured utilizing the potentiostat.

The polarization curve was done in the following manner: 0.6V set for 10 min then data taken every 6 seconds for 3 minutes. The measurement is initially held for 3 minute, before the 1st data point is collected, and then data is collected every 6 seconds for 3 minutes for each voltage set-point. This continues in the following voltage sequence, 0.55V, 0.5V, 0.45V, 0.4V, 0.6V, 1(for 1 minute), 0.65V, 0.7V, 0.75V, 0.8V, 0.85V and 0.6V.

Potentiostats often allow the choice of 2,3, or 4 terminal connections to the cell depending on the particular application. The two terminal connections are usually used when it is difficult to position the reference electrodes inside the cell itself. Although there is a reference electrode machined in the test fixture, it is assumed that the H_2 anode behaves as a reference electrode. The ECA or H_2 electrochemical stripping is a measure of the amount of Pt that takes part in the reaction. While the crossover measurement is a measure of the H_2 that diffuses through the PEM and is oxidized at the cathode. The ECA and the cross over current were measured in the following manner:

1. The cathode is purged with N_2 and the anode with H_2, both set at 50 sccm and 1 atm.
2. After the OCV is < 0.14V (as some H_2 diffuses through the PEM to cause a concentration cell OCV), the ECA is measured by utilizing the 1287 potentiostat (Solartron, Hampshire, U.K.). The counter electrode (CE) and reference electrode 1 (RE 1) are connected to the anode, while the working electrode (WE) and the reference electrode 2 (RE2) are connected to the cathode.
3. To measure the ECA of the MEA, the potential was swept from 0.0V to 0.6V for 4 cycles at 100 mV/s, while the cross over was measured at 0.0 V to 1.0 V at 2 mV/s for 3 cycles.
4. The total charge between 0.0V and 0.6V is integrated and after correcting for the double layer (assuming it is the baseline), the total charge produced by the reaction is calculated. The ECA can be calculated as assuming a stoichiometry of 1 e^- / Pt. Site[57]. The crossover is simply the plateau in current observed.

The pressure of the cell was increased to 1.5 atm on both the H_2 and air feeds, and a polarization curve was obtained. The temperatures of the fuel cell and the humidifers were then increased to 90°C. After utilizing the break in protocol for 1~2 hrs, to ensure steady-state performance has been reached, a polarization curve was obtained. Finally the ECA and crossover current were measured again.

In a similar fashion, the polarization curves, ECA and crossover current were measured at increasing temperatures. The temperatures of the humidifiers were maintained at 90°C and the cell temperature was returned to 70°C at the end of the experiment. Thus the temperature test protocol was: (a) Cell = 70°C, Hum. = 80°C, Beginning Of Life (BOL), (b) Cell = 90°C, Hum. = 90°C, (c) Cell = 100°C, Hum. = 90°C, (d) Cell = 110°C, Hum. = 90°C, (e) Cell = 120°C, Hum. = 90°C (f) Cell = 130°C, Hum = 130°C and P = 3 atm O_2 and (g) Cell = 70°C, Hum. = 80°C, end of life (EOL).

Results/Discussion

The results include the effects on water sorption as a function of RH and temperature of the: (*i*) additive particle size; (*ii*) the various forms of the additive; and the (*iii*) composite membranes. Additionally also discussed are the results on conductivity as a function of RH and temperature of the: (*i*) composites; and (*ii*) various wt.% loadings of ZrO_2 (A) composites. The higher temperature/lower RH MEA performance and IEC of Nafion 112 and composites are also discussed.

Water Uptake Measurements

Figure IV-4 shows the effect of particle size of the additive on the water uptake at 90°C and 120°C. The particle sizes of the ZrO_2 (A) and ZrO_2 (AP) samples were 10 μm and 8 μm respectively as measured with an SEM (AMR 1610). Even this small difference in particle size resulted in sorption effect. The smaller particles with their larger surface areas (based on the SEM particle size measurement) demonstrate higher water uptake at all temperatures. When the water uptake was normalized to the particle surface area, it was almost identical for both samples. Thus, we conclude that the additive will exhibit higher water uptake as the particle size becomes smaller resulting in an increase in surface area and a larger number of sites available for water adsorption.

Figure IV-5 shows the water uptake of all the powder samples at 120°C. Of all the additives investigated the most promising appears to be the ZrO_2 (sample with no acid treatment) as it demonstrates the highest water uptake of all the samples.

Figures IV-6 a-c show the water uptake of the Zirconia/Nafion® composites as well as Nafion® only. Figure IV-6a shows the water uptake of the composites and Nafion® 112 at 25°C. The Nafion® 112 sample is observed to have a higher water uptake than the composites from 30% RH to 60% RH, but outside this range the water uptake of all the PEM are similar. Thus, the presence of these dopants does not significantly alter the water uptake of Nafion® at room temperature.

Figure IV-6b shows the water uptake of membrane samples at 90°C. The Nafion® 112 and the Nafion® ZrO_2 sol-gel PEMs demonstrate higher water uptake than the 5 wt.% SO_4/ZrO_2 and the 5 wt.% ZrO_2 (A) composites.

The water uptake of all membranes at 90°C is seen to have increased versus the uptake at 25°C. The Nafion® 112 PEM shows a 40% increase and the Nafion® ZrO_2 sol-gel composite shows an increase of 66% at 40% RH. This increase in water uptake with temperature may occur due to a softening of the PEM at higher temperature, thus increasing the pore size allowing more water to adsorb.

Figure IV-6c shows the water uptake of the composites measured at 120°C. The water uptake of the composites has decreased compared to 90°C and is similar to the amounts measured at 25°C. The Nafion® 112 shows a water uptake at 120°C that is only about half of the uptake at 25°C. This reduction in the water uptake at 120°C at low RHs may result from a pore network collapse of the Nafion® component, as the glass transition point of Nafion® ~110°C[2].

It is important to note that all the composites show an enhanced water uptake when compared to Nafion®. The Nafion® ZrO_2 sol-gel composite shows the highest water uptake of all the samples tested and is almost 45% higher than Nafion® 112 at 40% RH. The 5 wt. % SO_4/ZrO_2 and the 5 wt. % ZrO_2 (A) both show water uptake that is 20% higher than the Nafion® 112 sample at 40% RH. Thus, the behavior of the composite PEMs reflects the trend observed in the powder samples, in that the Nafion® ZrO_2 sol-gel composite with the smallest particle size and composed of ZrO_2, has the highest water uptake of all the composites.

To further understand the interaction between the additive and Nafion®, a comparison of loaded composites is shown in figure IV-7. The plot shows the observed water uptake of a 5 wt. % and 10 wt. % ZrO_2 (A) loaded PEM. As the additive loading increased, the water uptake also increased. The additive has a higher water uptake than Nafion® 112, thus, as the additive fraction of composite increases, the water uptake of the resulting composite PEM also increases. The figure also shows the theoretically expected water uptake of the composites, assuming the water uptake of the additive is summative. As can be observed from the figure, the measured uptake of loaded composites was higher than theoretically expected. This likely occurs because the dispersion of the particles within Nafion® resulted in a larger surface area than available in the unsupported powder. Apparently the presence of the Nafion® film does not restrict the sorption properties of the additive.

Ion-Exchange Measurements

Table IV-1 shows the equivalent weights of the Nafion® composites, Nafion® 112 and the solvent cast Nafion®.

The solvent cast Nafion® has a higher EW indicating a lower number of acid sites in comparison to the Nafion® 112 sample. The processing of the solvent cast Nafion® may alter the morphology of the PEM leading to a smaller number of accessible acid sites vs. commercial Nafion® 112. The Nafion® ZrO_2 sol-gel composite has the highest number of acid sites available of the membranes investigated. The ZrO_2 (A) loaded composites showed a similar number of acid sites as that found in the Nafion® solvent cast, with the number of acid sites decreasing with an increase in the additive content.

It is unusual that only the Nafion® ZrO_2 sol-gel composite has higher acidity than unmodified Nafion® while the other composites exhibited lower acidity. Based on the reported Hammett acidity of these materials, it was expected that the IEC would increase. The increased loading of the additive may have caused agglomeration of the particles, thus reducing the number of available acid sites. Based on gravimetric and preliminary ash analysis, there is a low loading of particles in the Nafion® ZrO_2 sol-gel composite ranges from 1~ 3 wt. %, thus a large number of acid sites are available, as there is assumed to be negligible agglomeration.

Conductivity Measurements

Figure IV-8a shows the Z-plane conductivity of the Nafion® 112, solvent cast Nafion® and the composite PEMs measured at 10% RH and 40% RH at a temperature of 90°C. The Nafion® ZrO_2 sol-gel composite has the highest conductivity of all the composites investigated. This composite also exhibits a 15% increase in conductivity over Nafion® 112. The 5% ZrO_2 (AP) composite exhibits the highest conductivity of all the composites except the Nafion® ZrO_2 sol-gel composite and has a conductivity that is similar to Nafion® 112, while the 5% ZrO_2 composite showed dramatically lower conductivity than the other composite membranes. The composite was prepared by precipitation of Zirconia from the 20 wt.% ZrO_2/Acetic acid colloidal solution, and then directly added, with no acid treatment, to the Nafion® solution to cast a membrane. The conductivity at 40% is almost 2 orders of magnitude lower than that of the cast Nafion®. The particles of ZrO_2 are very large (85 μm,) and segregate during membrane fabrication form an asymmetric film on Nafion®. This non-acid treated ZrO_2 film would have low conductivity and resulted in poor conductivity of the composite.

Figure IV-8b presents the Z-Plane conductivity of the PEMs measured at 120°C. The largest conductivity is exhibited by the Nafion® ZrO_2 sol-gel composite with a 24% enhancement over Nafion® 112 at 40%. All the other composites have a conductivity smaller than that of Nafion®.

The conductivity of the Nafion® ZrO_2 sol-gel composite is higher than Nafion® resulting from the enhanced water uptake and acidity. Although the other composites show an enhanced water uptake at 120°C, the acidity as well as conductivity of these PEMs is similar or less than that of Nafion®. It is important to note that an enhancement in the water sorption properties of the PEM will not necessarily translate into a conductivity benefit[58]. Additionally if the additive does not remain dispersed homogenously within the PEM matrix, the benefits of the additives increase in acidity and water sorption will be localized to the nearby regions, thus the conductivity of the remainder of the PEM will remain unchanged.

The X-Y plane conductivity of 5%, 10% and 20% ZrO_2 (A) loaded composites is shown in figures IV-9a and IV-9b at 90°C and 120°C respectively. It is observed that the optimum conductivity in both cases is with the 10% loaded PEM. A small increase in conductivity is observed when the loading is increased from 5% to 10%, while a dramatic decline is observed when the loading is increased to 20%.

Although the water uptake of the composites increases with loading of the additive, the IEC measurements show that an increase in the loading causes an EW decrease. The combination of the enhanced water sorption but the subsequent lower acidity of the composites results in an optimum conductivity of 10% additive loading (Eq. 1).

MEA Performance Characteristics

Figure IV-10 shows the measurements obtained with a Nafion® 112 MEA that was tested at 70°C, 90°C, 100°C, 110°C, 120°C, 130°C and then returned to 70°C, following the measurement procedure described.

The electrochemical surface area measurements are shown in Table IV-2. As the temperature increases, the ECSA decreases indicating a reduced active area. The temperature increase should increase the rate of reaction, producing a larger total charge measured, however, the data indicate a decrease in the total charge as well. This is probably due to a decrease in the area available for the three-phase reaction zone. Kanamura et. al[42] investigated the Nafion®/Pt interface with *insitu* spectroscopic techniques (FTIR, AFM and surface potential measurements). The interface was observed to have a dynamic nature, in the dry state the interface is very small while in the humidified state the interface was extremely extended. Additionally, the conductivity of the Nafion® ionomer present within the catalyst layer will also drop at higher temperatures and low RH. Thus, the electrochemical reaction occurring and the current maybe limited by the lower rate of proton transport in the ionomer at lower RH or decrease in the reaction zone, or both.

From Figure IV-10 it is also observed that there is a decline in performance not only as the cell temperature increases (and as RH decreases), but also between BOL and EOL polarization, ~ 300 mA/cm^2 at 0.6V for the Nafion® only MEA. It is also noted that the ECSA measurements at 70°C BOL and 70°C EOL are 41 mC/cm^2 and 29.2 mC/cm^2 respectively, while the cell resistance measurements are 20.3 mΩ and 21.5 mΩ at 70°C BOL and 70°C EOL respectively. Thus the performance loss is likely as a result of electrode overpotential, as the ohmic resistance measured at the BOL and EOL is similar. At the higher temperatures and dry conditions the peroxide catalyzed degradation of the ionomer adjacent to the active catalyst sites and rearrangement of ionomer morphology in the catalyst layer may significantly diminish protonic conductivity, leading to a decrease in the three-phase reaction zone area.

The final observation is that although operating at low RH and high temperature, none of the MEAs fabricated failed catastrophically. The crossover current measurements also demonstrated very low current (0.5mA/cm^2) generated by H_2

crossover at high temperature (120°C), while performance at 130°C (Humidifiers at 130°C, P= 3 atm) shows no degradation over several hours. At these conditions the PEM is swelled by saturated steam placing severe stress on the MEA. It is critical that higher temperature material issues are addressed in the assembly of the MEA to lower the probability of catastrophic MEA, e.g. pinhole formation leading to large H_2 crossover.

A Nafion®/ZrO_2 sol-gel composite was fabricated as an MEA and tested at conditions similar to Nafion® 112. The resulting performance is shown in Figure IV-11 where the composite and Nafion® 112 MEA performance are compared. Although no performance improvement is observed, it is noted that the *insitu* MEA ohmic measurements show an improvement of the composite vs. the Nafion® 112, providing further evidence that the composite conductivity is higher than unmodified Nafion®. Based on our fuel cell model[59] simulations the drop in conductivity from 0.05 S/cm at 80°C to 0.005 S/cm at 120°C with Nafion® 112 causes the cell performance to drop[29]. Thus, a tenfold conductivity enhancement would maintain high cell performance for a composite MEA. The most promising composite, Nafion®/ ZrO_2 sol-gel composite, demonstrates a 24% conductivity improvement over Nafion® 112, and it may be necessary to further increase the conductivity to observe an MEA performance benefit at higher temperatures and low RH. Additionally, at lower RH and higher temperature the dehydration of a Nafion® catalyst layer may limit fuel cell performance, thus the incorporation of ZrO_2 in the catalyst layer should result in improved performance.

Conclusions

Based on a rational design, the synthesis of composite PEMs for higher temperature/lower RH operation has been accomplished. The promising potential of these PEMs has been demonstrated with improved conductivity. In our literature survey, no PEMs have been reported that demonstrate improved conductivity over Nafion® at higher temperature/lower RH conditions, and thus these PEMs are a significant milestone. Although none of our composites have demonstrated the considerable conductivity improvement necessary to recover high performance at higher temperatures/lower RH, the increase in rates of reactions, improved CO tolerance[60] and water management may provide useful power densities even with a smaller enhancement.

Present work is ongoing to further improve the conductivity of Nafion®/ ZrO_2 sol-gel composite. The subsequent PEM synthesis and characterization is progressing, along with MEA optimization and evaluation. It has also been recently reported that the metallic oxides maybe unstable in Nafion®, which is also being addressed[33]. Utilizing additional characterization tools, the conductivity benefits of the dispersion, stabilization and loading of nano-structured Zirconia in a polymeric PEM can be optimized further.

Additionally, Nafion® is composed of hydrophobic/hydrophilic regions, the hydrophobic backbone is necessary as it maintains structural stability albeit lower water sorption. The incorporation of SO_4^{2-}/ZrO_2 nano-particles in a PEM that lacks this hydrophobic backbone should serve the dual purpose of enhancing conductivity at higher temperatures/lower RH and maintaining the PEM's thermo-mechanical stability for fuel cell applications. Additionally the incorporation of the Zirconia additives in the catalyst layer to minimize electrode overpotential, and the long-term evaluation of these MEAs by fuel cell testing is also being undertaken.

Although significant challenges have been identified, it is expected that continued development will eventually result in high performance PEMs at higher temperature/ lower RHs based on this design.

Table IV-1: The EW of the composite membranes, Nafion® 112 and solvent cast Nafion® at 25°C.

Samples	EW (g/mol. H^+)
Nafion 112	1106±15
Nafion Solvent Cast	1173±15
Nafion ZrO_2 Sol-gel.	1006±15
5% ZrO_2 (A)	1084±15
10% ZrO_2 (A)	1121±15
20% ZrO_2 (A)	1159±15

Table IV-2: The ECSA of a Nafion® 112 MEA at different fuel cell temperatures, when the temperature of the humidifers remains constant at 90°C.

Nafion 112	ECSA (mC/cm^2)
70°C (EOL)	40.8
90°C	43.8
110°C	21
120°C	15
70°C (BOL)	29.2

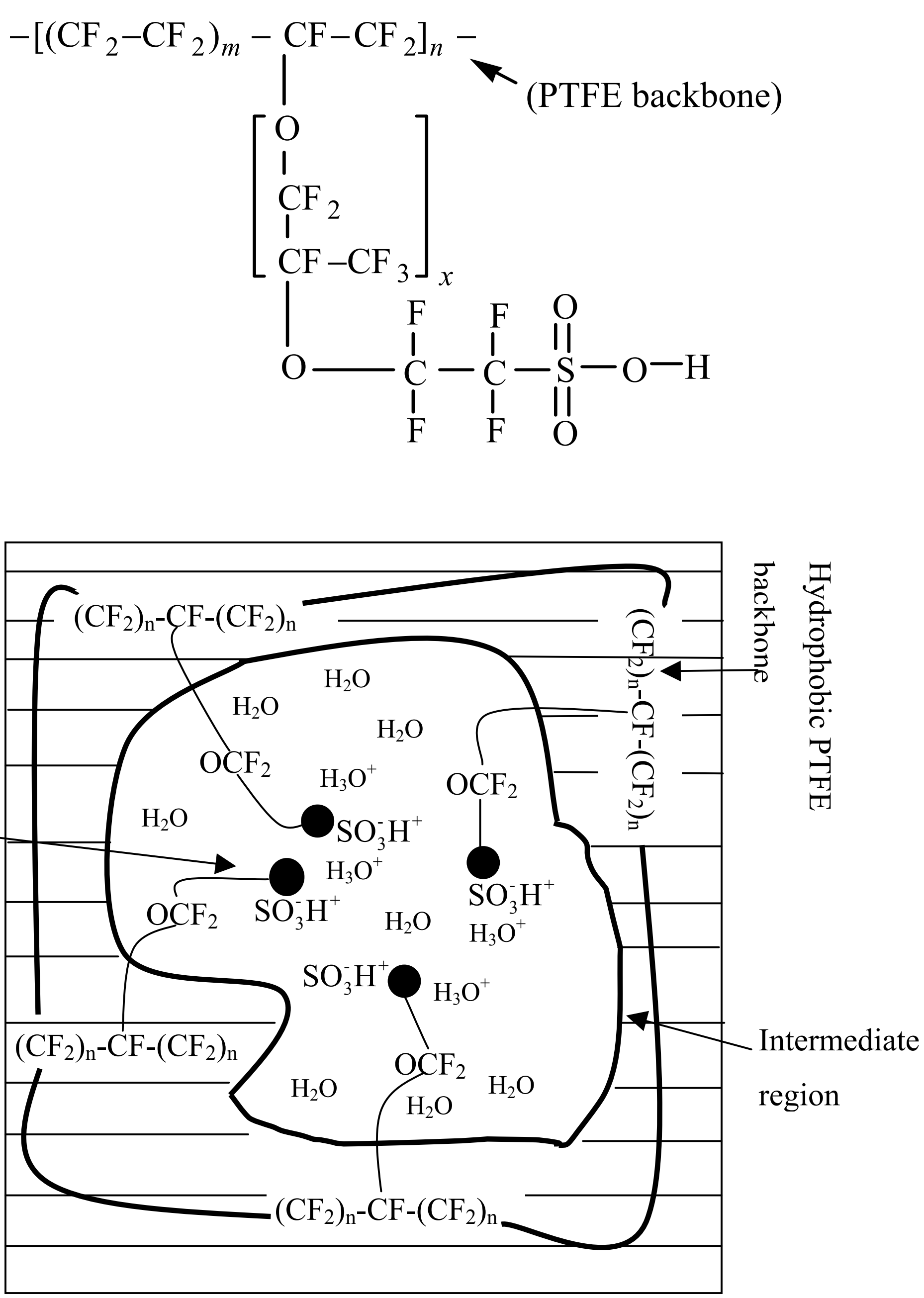

Figure IV-1a: Structure of Nafion®. The values of n and x can be varied to produce materials with different equivalent weights (EW). The PTFE backbone enhances the mechanical strength of the PEM albeit at the cost of lower water sorption. The PEM can be divided into three different regions: the hydrophobic PTFE backbone, the hydrophilic ionic zone and the intermediate region[6].

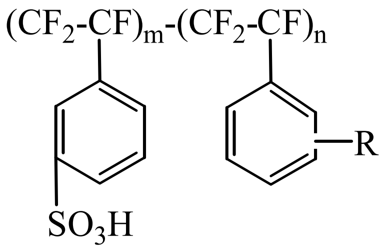

Figure IV-1b: Structure of Ballard Advanced Materials Third Generation (BAM3G) membrane. The PEM has shown significant lifetime performance but remains exclusive to Ballard.

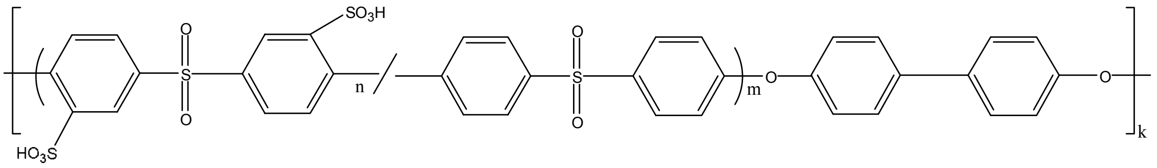

Figure IV-1c: Random sulfonated poly(arylene ether sulfone)s (PBPSH-XX). (n+m)/k = 1.01 (in mole); XX = 100n/(n+m)[24]. The hydrocarbon based PEM shows performance similar to Nafion®.

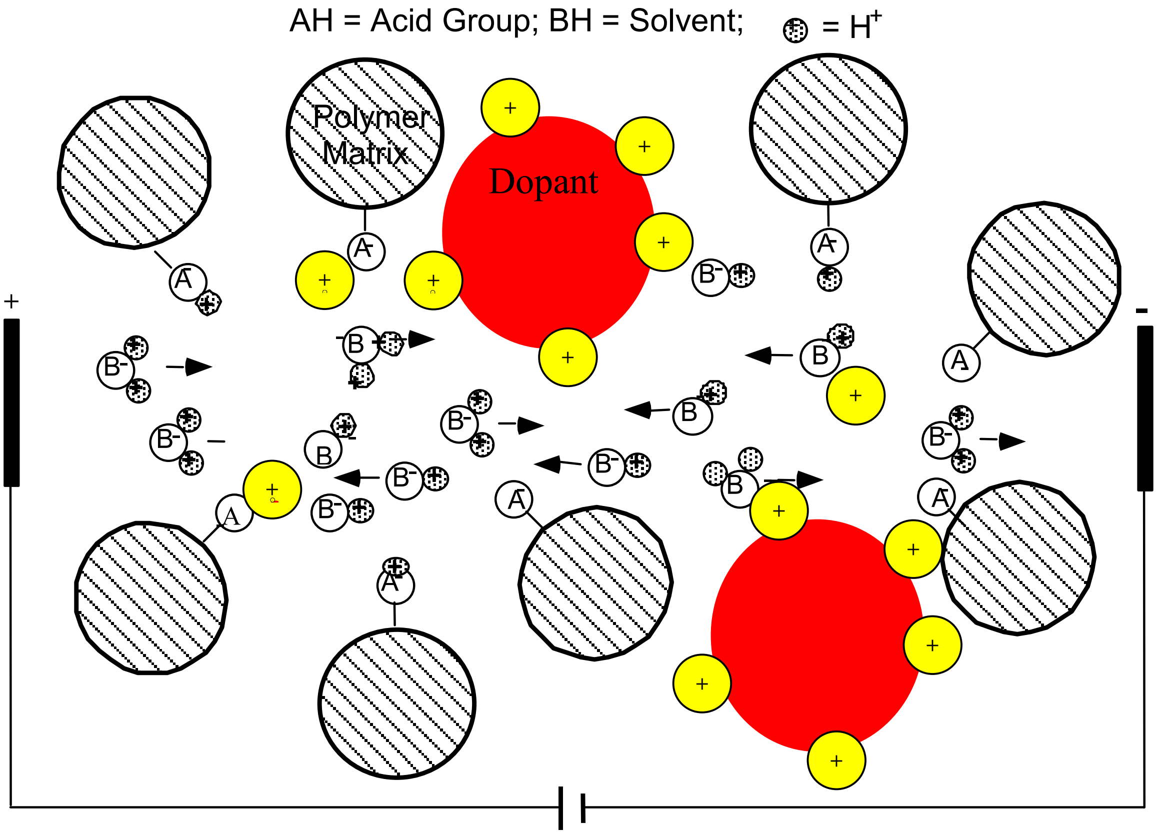

Figure IV-2: A Dusty-Fluid formalism was utilized to describe proton conductivity through the Nafion® polymer matrix and the superacidic dopant. The framework treats the Nafion® matrix as large dust particles through which the current carrying ions must traverse.

.

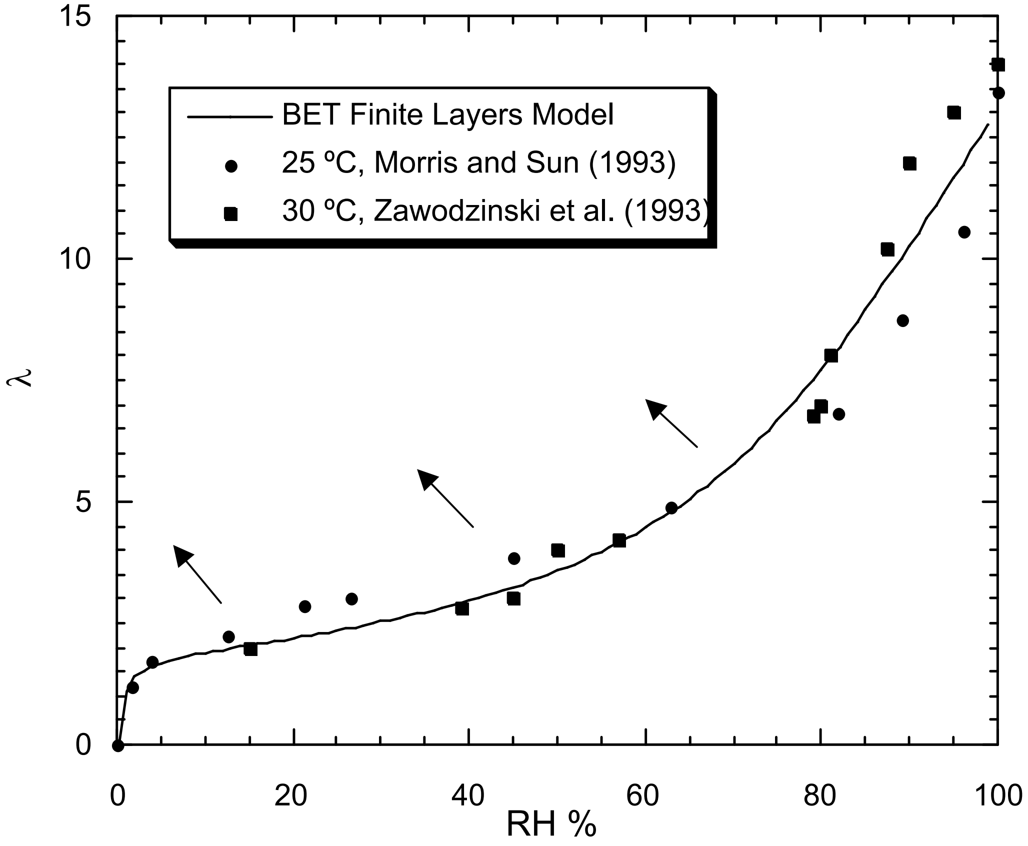

Figure IV-3: The design objective of increasing the sorption isotherm of Nafion®, thus the composite will adsorb more water at a fixed R.H. vs. unmodified Nafion® resulting in higher conductivity at low RH.

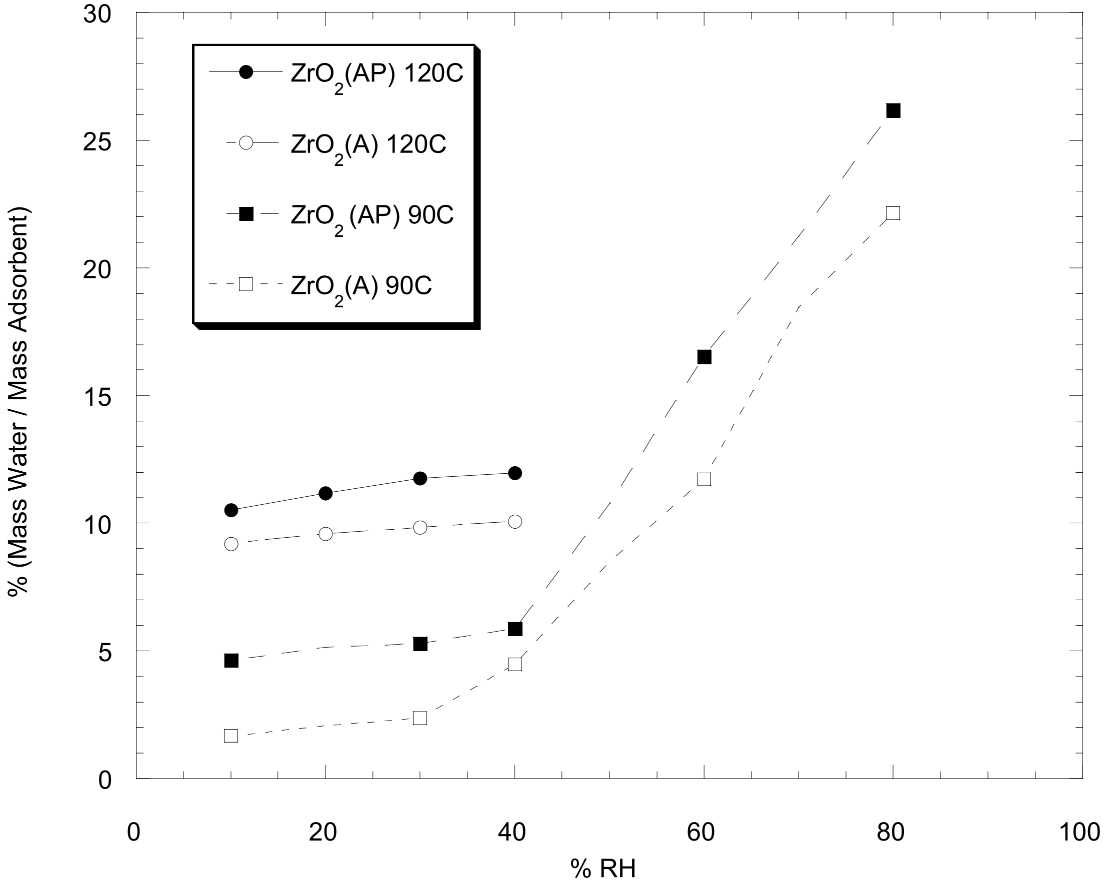

Figure IV-4: The effect of particle size is shown. The ZrO_2 (A) particle size is 10 µm, while the jet milled sample ZrO_2 (AP) is 8 µm. The smaller particle size sample has a larger surface area, resulting in higher water uptake at all temperatures.

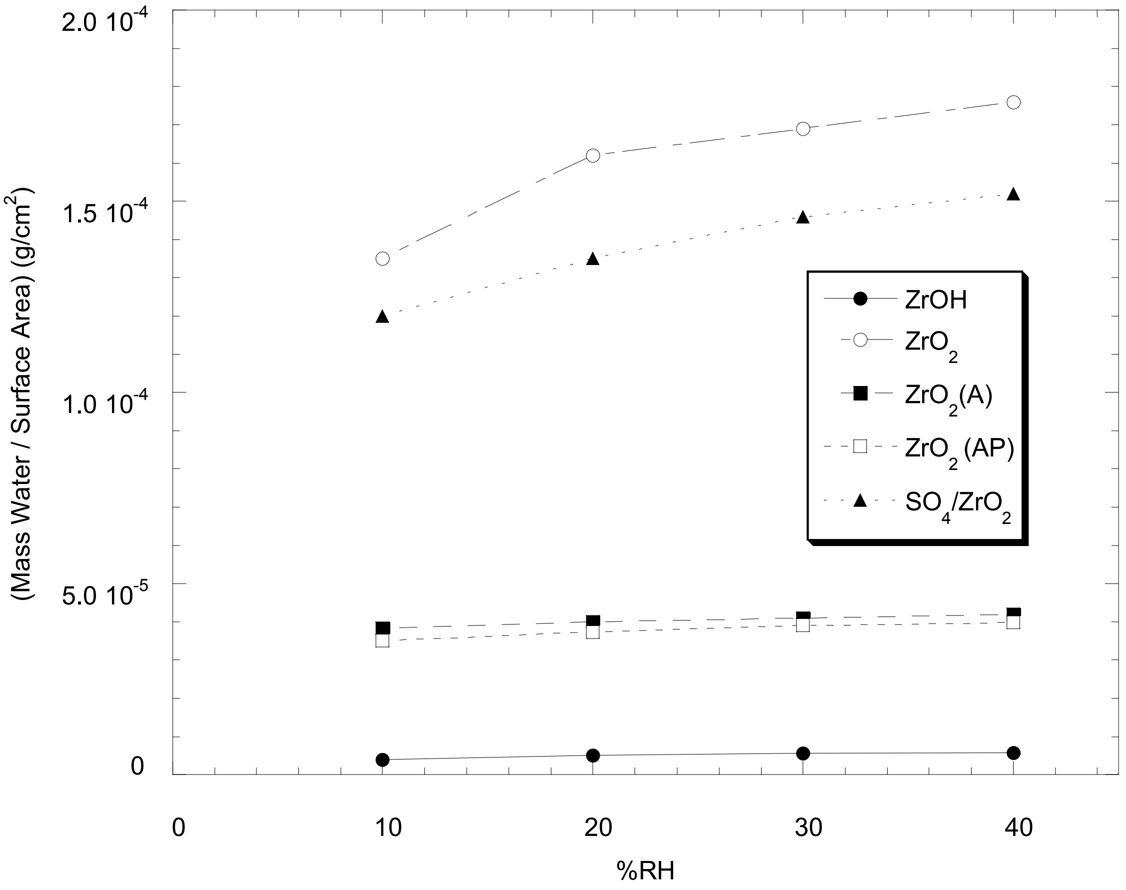

Figure IV-5: The surface area normalized water uptake of the powder at 120°C vs. RH. The most promising candidates are the ZrO_2 and the SO_4/ZrO_2 samples.

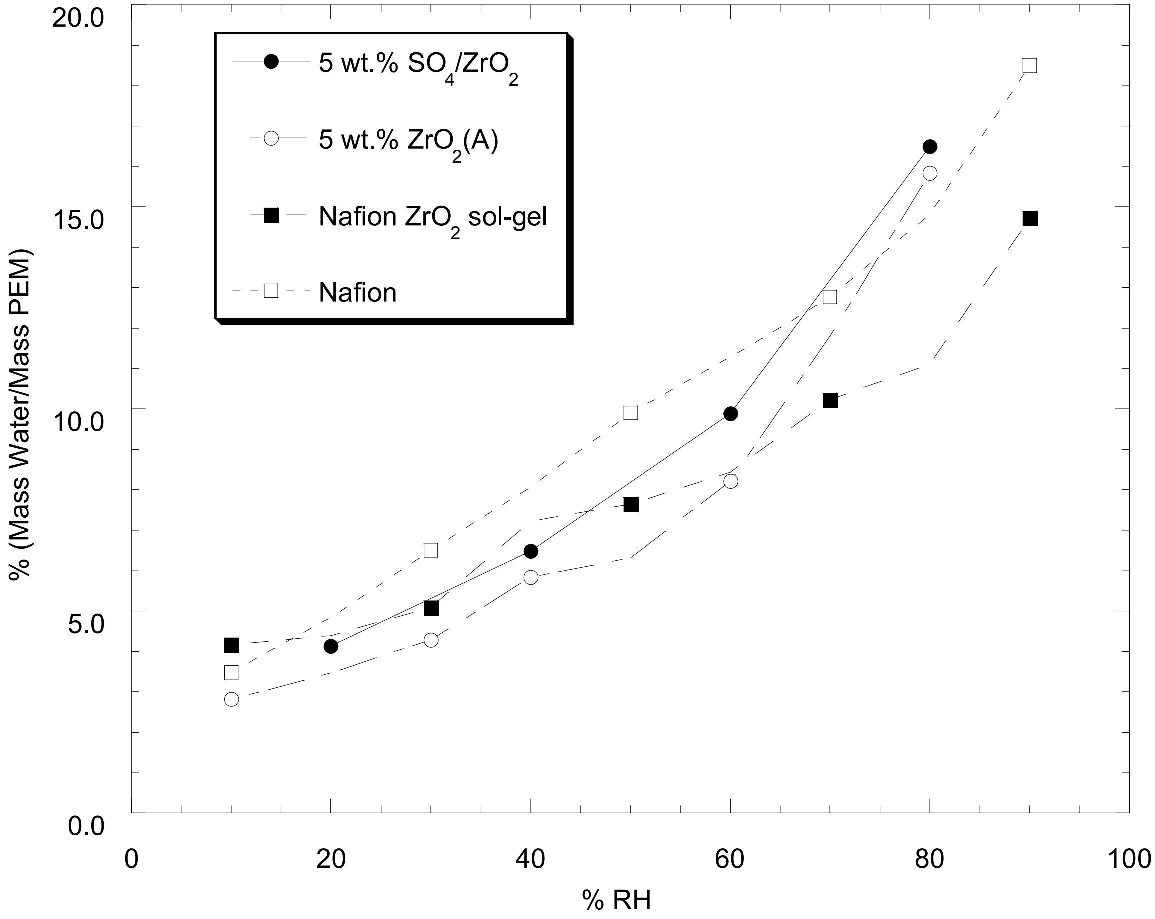

Figure IV-6a: The water uptake of composite membranes and Nafion® 112 at 25°C vs. RH. The water uptake of all the PEM samples is similar.

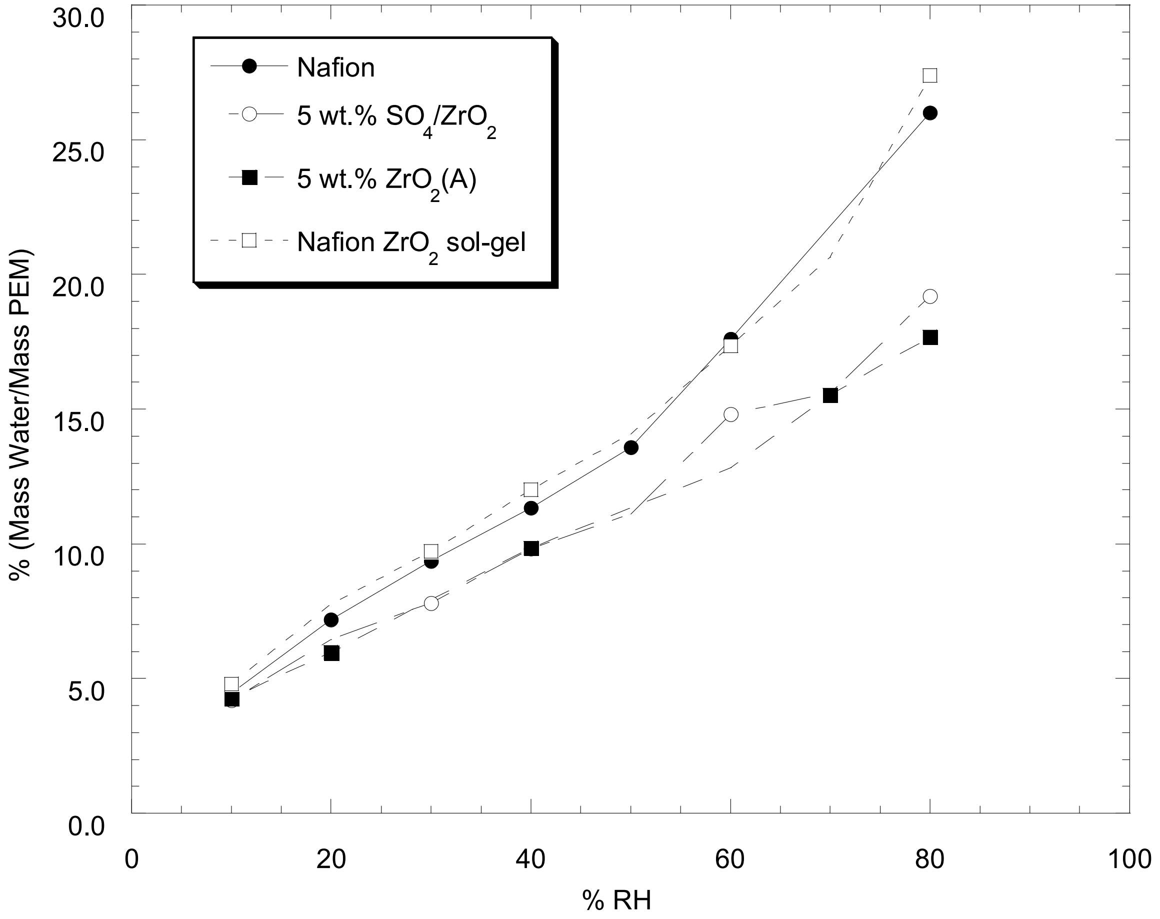

Figure IV-6b: The water uptake of composite membranes and Nafion® 112 at 90°C vs. RH. The water uptake of the Nafion and Nafion sol-gel PEM are similar and higher than the other composites.

.

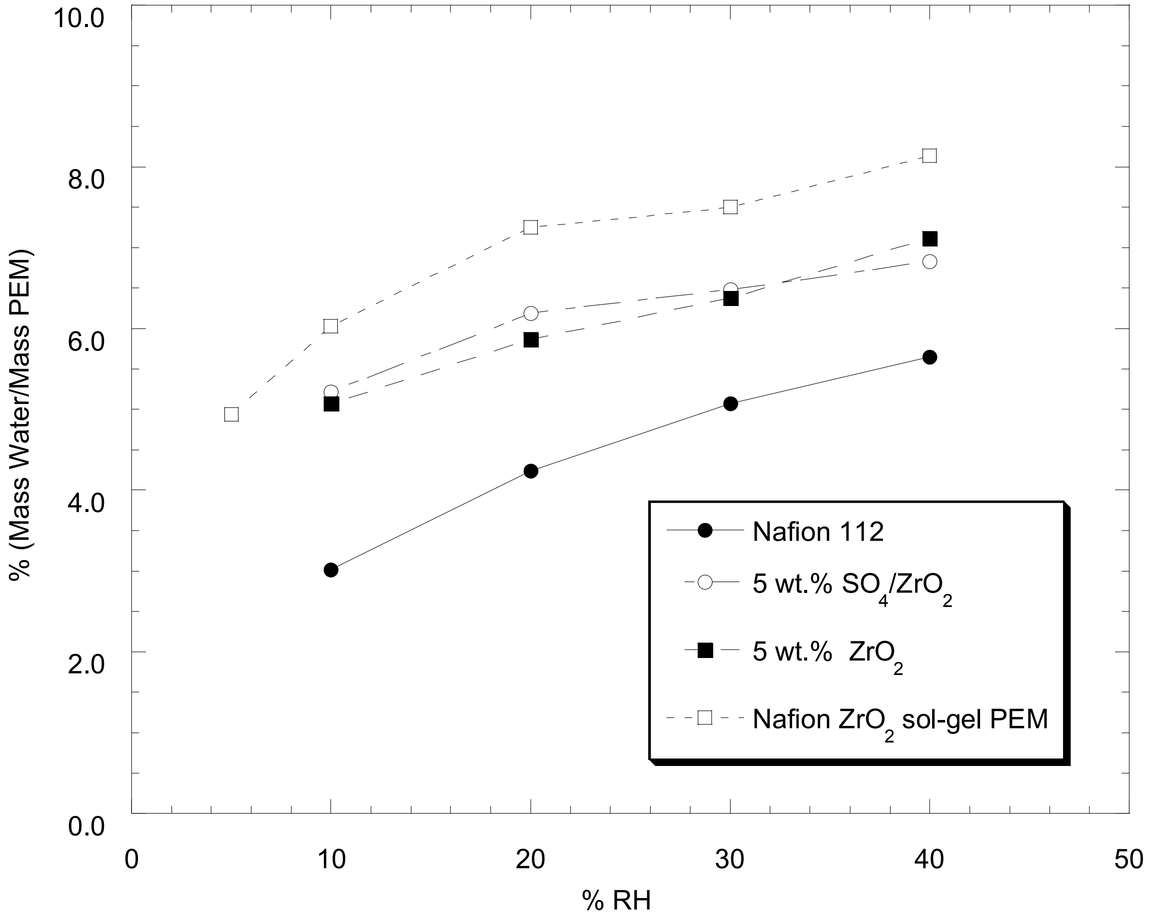

Figure IV-6c: The water uptake of composite membranes and Nafion® 112 at 120°C vs. RH. The Nafion ZrO_2 sol-gel PEM demonstrates the highest water uptake.

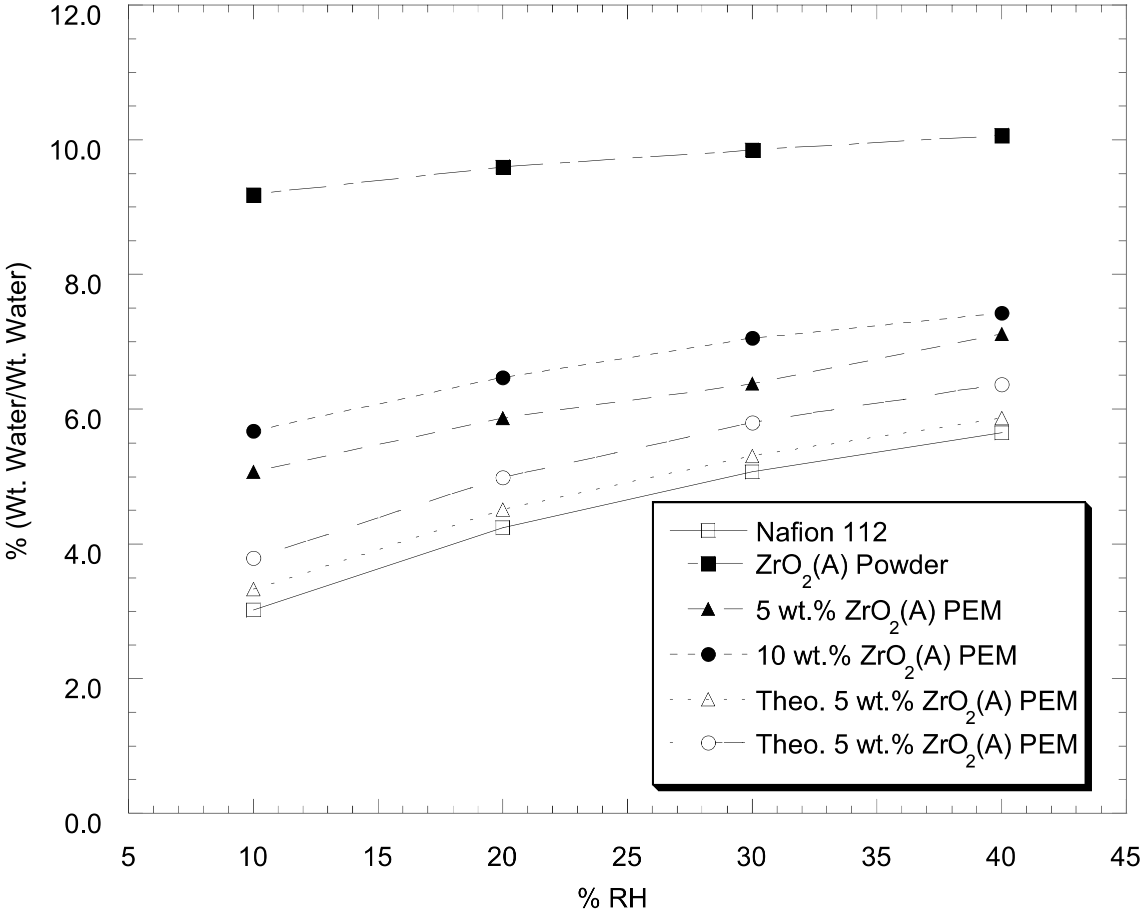

Figure IV-7: The measured and theoretical water uptake of composite PEMs at 120°C vs. RH. The theoretical amount is the expected water uptake amount if the particle water uptake is added to the un-modified PEM.

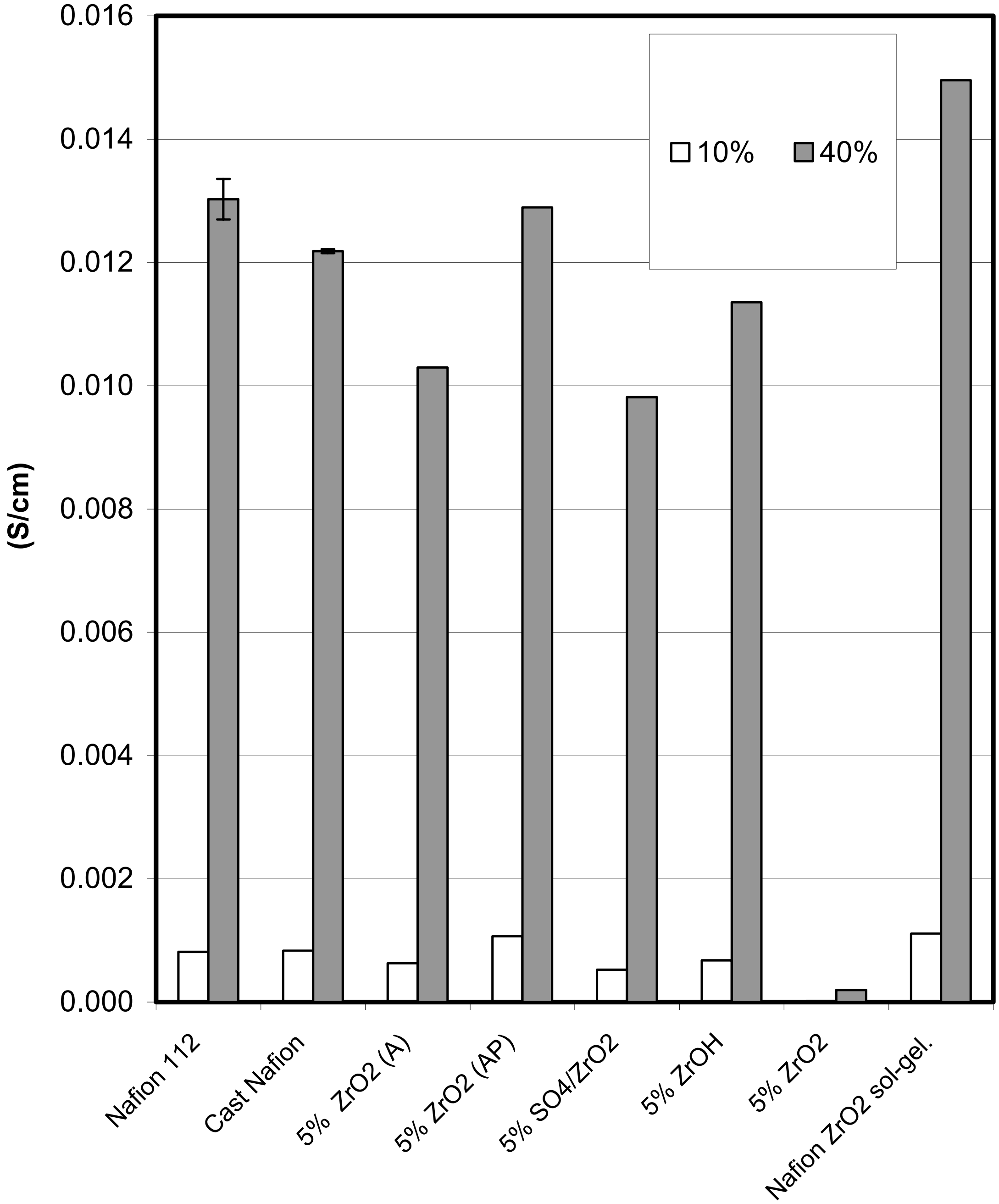

Figure IV-8a: The conductivity of the PEMs at 10% RH and 40% RH at 90°C. The Nafion ZrO2 sol-gel PEM shows the highest conductivity of the samples.

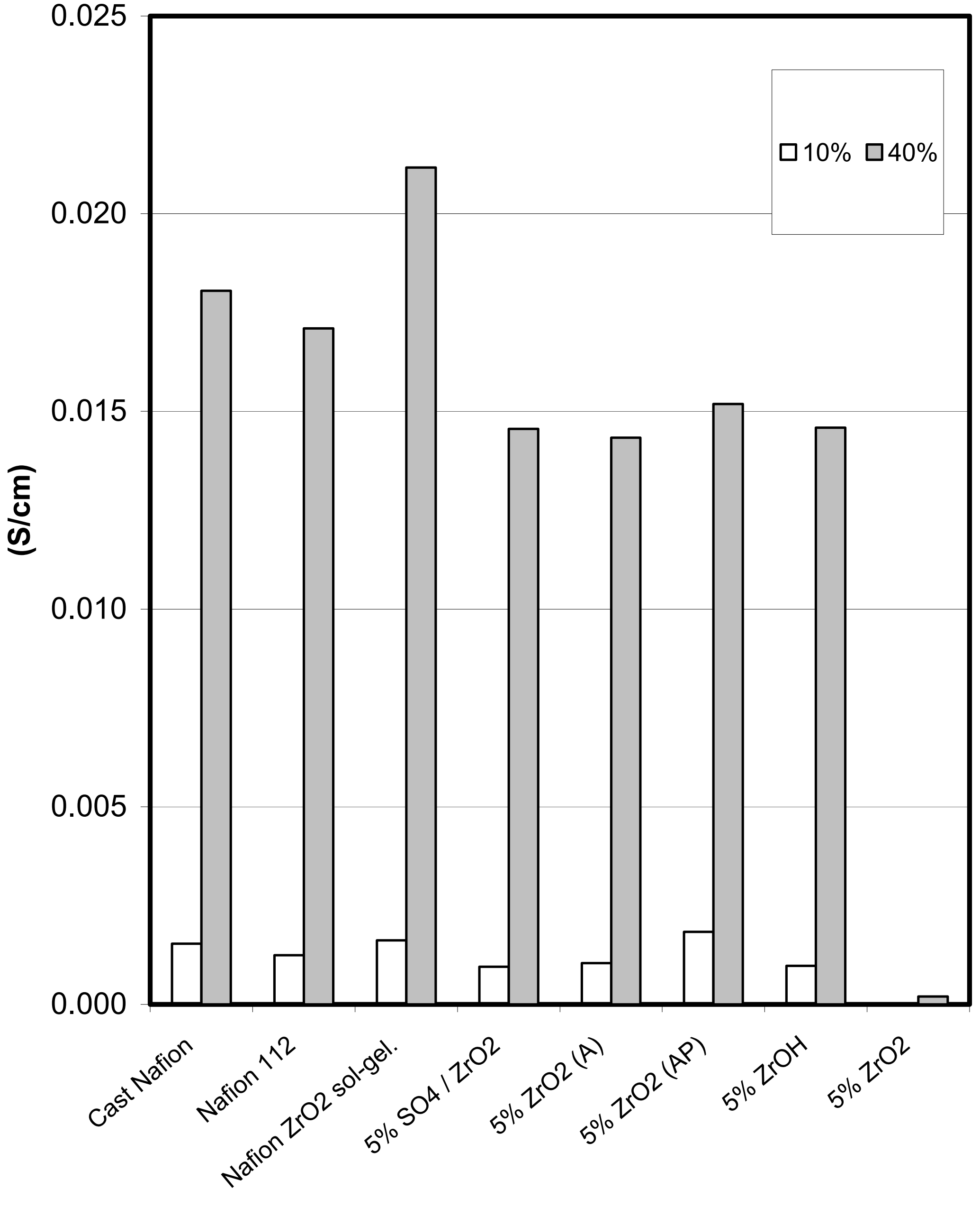

Figure IV-8b: The conductivity of the PEMs at 10% and 40% RH at 120°C. The Nafion ZrO2 sol-gel PEM shows the highest conductivity of the samples.

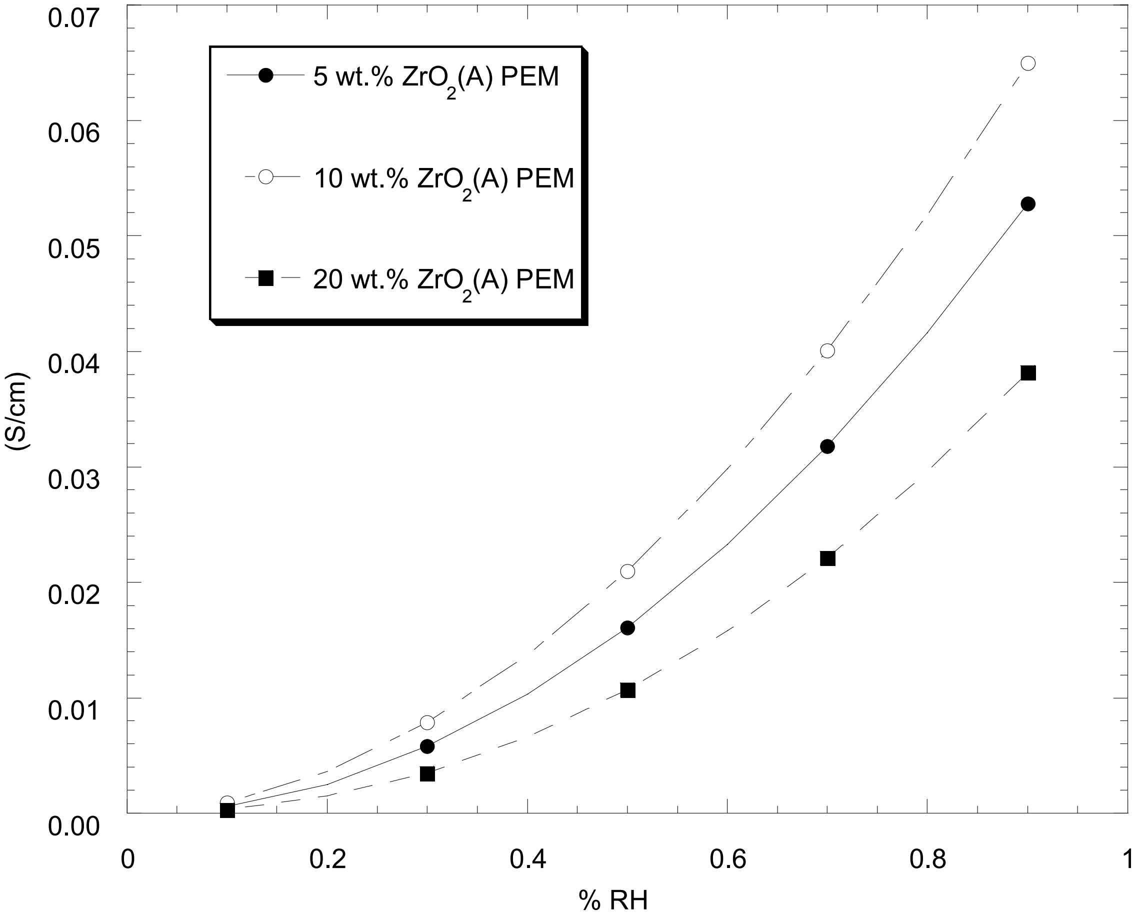

Figure IV-9a: The conductivity of loaded composites PEMs at 90°C vs. RH. The optimum conductivity is observed with the 10 wt.% PEM.

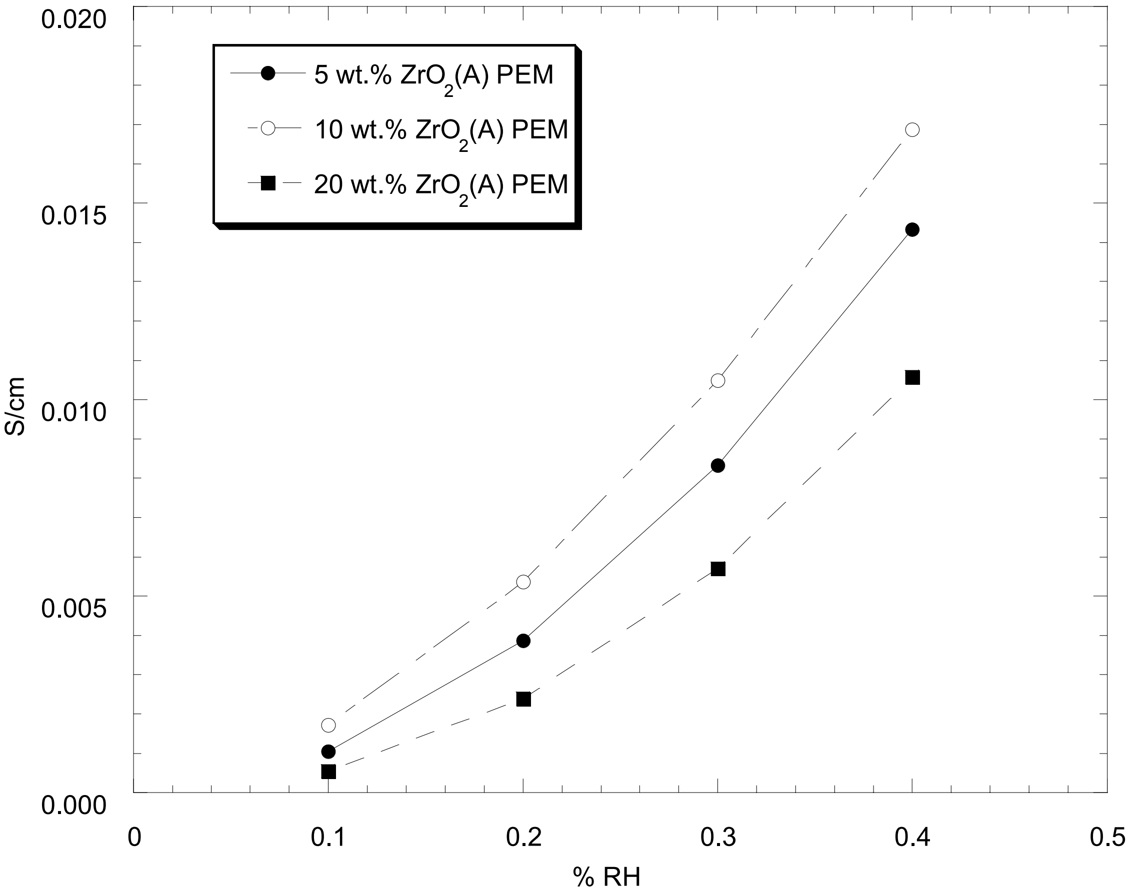

Figure IV-9b: The conductivity of loaded composite PEMs at 120°C. The optimum conductivity is observed with the 10 wt.% PEM.

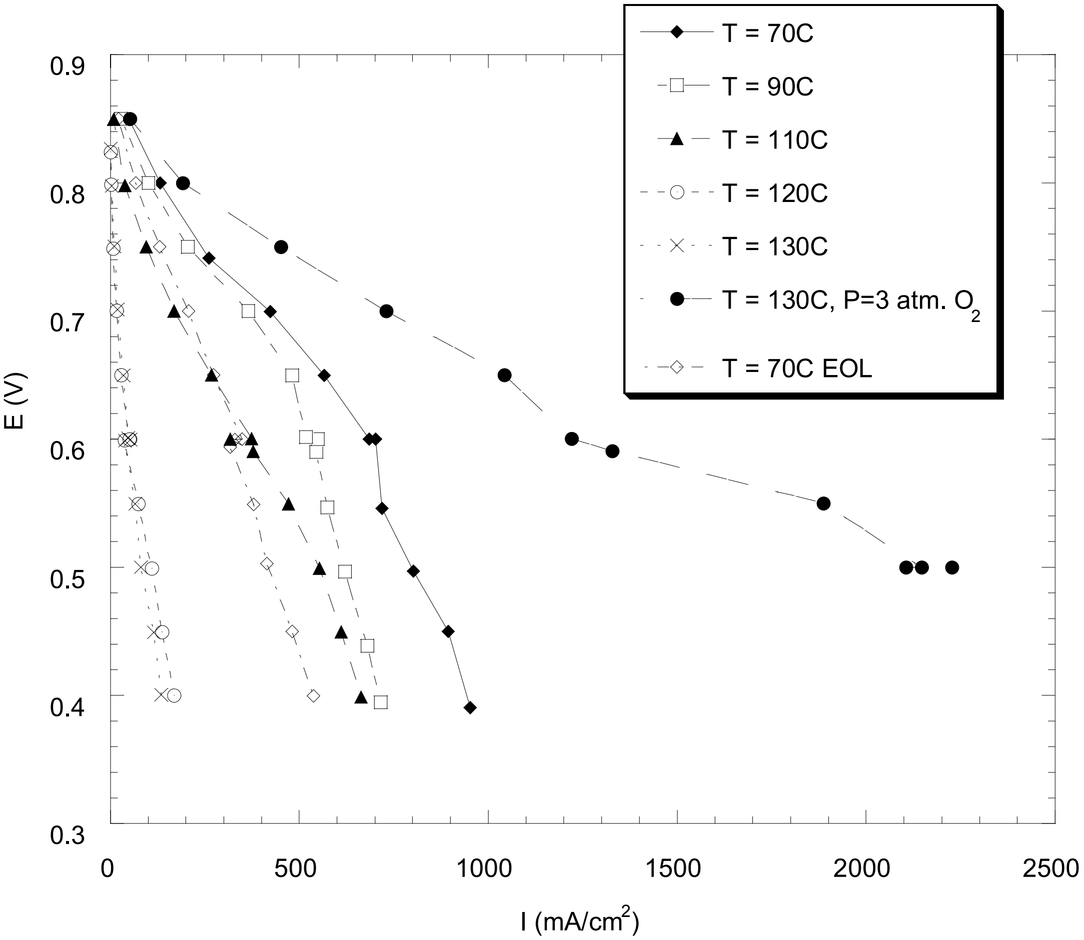

Figure IV-10: The cell performance of Nafion 112 MEA with conditions operated with 7 psig Air /H_2, humidifiers set at 90°C. The exception was when the cell was at 130°C, 3 atm. O_2 and the humidifiers set at 130°C.

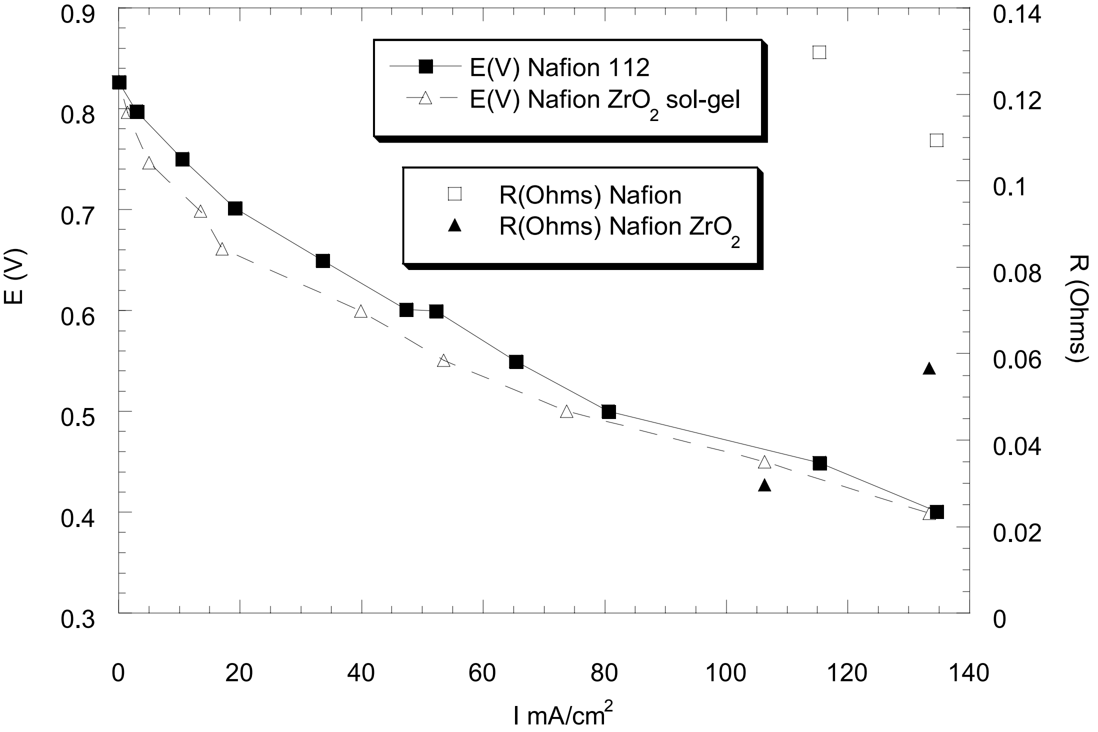

Figure IV-11: The cell performance of Nafion 112 MEA vs. Nafion ZrO_2 sol-gel composite MEA. Air and H_2 at 2.0 and 1.3 stoich. flows respectively, P = 1.5 atm., $T_{HUMIDIFIER}$= 80°C, T_{CELL} = 110°C.

References

1 A. Eisenberg and J.S. Kim, *Introduction to Ionomers,* John Wiley & Sons, New York (1998).

2 S. C. Yeo, A. Eisenberg, *J. App. Polym Sci.,* **21**, 875 (1977).

3 R.M. Ikeda, Ed, *Polymer Preprints*, *ACS, Div. of Poly. Chem., Amer. Chem. Soc.* **19 (2)**, 215 (1978).

4 A. Steck*, Procedings of the First International Symposium on New Materials for Fuel Cell Systems*, (O. Savagodo, P.R. Roberge, T.N. Veziroglu Eds.) Montreal, Canada, July 9-13, 74 (1995).

5 W. Grot, *Encyclopedia of Polym. Sci. and Eng.*, **16**, 642 (1989).

6 H.L. Yeager and A. Steck, *J. Electrochem. Soc.,* **128**, 1880 (1981).

7 D.S. Watkins, *Abstracts* 33rd *Int Power Sources Symp.,* The Electrochemical Society, Pennington, N.J. 782 (1988).

8 M. Hogarth and X. Glipa, *High Temperature Membranes For Solid Polymer Fuel Cells* ETSU F/02/00189/REP DTI/Pub URN 01/893 (2001).

9 D.D. DesMarteau, *J. Fluorine Chem.*, **72**, 203 (1995).

10 S.V. Kotov, S.D. Pederesen, W. Z-M Qui and D.J. Burton, *J Fluorine Chem.*, **82**, 13 (1997).

11 S.C. Savett, J.R. Atkins, C.R. Sides, J.L. Harris, B.H. Thomas, S.E. Creager, W.T. Pennington and D.D. DesMarteau, *J. Electrochem. Soc.,* **149**(12), A1527 (2002).

12 R.B. Hogdon, *J. Polymer Sci.*, **6**, 171 (1968).

13 A.E. Steck and C. Stone*, Procedings of the 2nd International Symposium on New Materials for Fuel Cell and Modern Battery Systems*, (O. Savagodo, P.R. Roberge, T.N. Eds.) Montreal, Canada, July 6-10, 792 (1997).

14 H.P. Brack, F.N. Buchi, J. Huslag and G.G. Scherer, *Proton Conducting Membrane Fuel Cells II* (Eds S Gottesfeld, T.F. Fuller) PV 98-27, ECS, Pennington, N.J. 52 (1999).

15 Y Sone, P Ekdunge and D Simonsson, *J. Electrochem. Soc.*, **143**, 1254 (1996).

16 P.Murugaraj, K.-D.Kreuer, T. He, T. Schober and J. Maier, *Solid State Ionics*, **98**, 1 (1997).

17 T. Norby, *Solid State Ionics*, **125**, 1 (1999).

18 R. Savinell, E. Yeager, D. Tryk, U. Landau, J. Wainright, D. Weng, K. Lux, M. Litt and C. Rogers*, J. Electrochem. Soc.,* **141**, L46 (1994).

19 M. Doyle, S. K. Choi, and G. Proulex, *J. Electrochem. Soc.,* **147**, 34 (2000).

20 M. Rikukawa and K. Sanui, *Prog. Polym. Sci.* **25**, 1463 (2000).

21 O. Savagodo, J. New Mater. Electrochem. Syst., **1**, 66 (1998).

22 J. Kerres, A. Ullrich, F. Meier and T. Haring, *Solid Sate Ionics,* **125**, 243 (1999).

23 J.E. McGrath, *Proton Exchange Membrane Nanocomposites for Fuel Cells*, Advances in Materials for Proton Exchange Membrane Fuel Cell Systems, ACS, Pacific Grove, CA (2003) Feb. 23-27.

24 F. Wang, M. Hickner, Y. S. Kim, T.A. Zawodzinski and J.E. McGrath, *J. Membr. Sci.*, **197**, 231 (2002).

25 R.F. Savinell, J.S. Wainright and M. Litt, *Proton Conducting Membrane Fuel Cells II* (Eds S. Gottesfeld, T.F. Fuller) PV 98-27, ECS, Pennington, NJ 81 (1999).

26 S.M.J. Zaidi, S.D. Mikhailenko, G.P. Robertson, M.D. Guiver and S. Kaliaguine, *J. Membr. Sci*, **173**, 17 (2000).

27 S. Chandra, *Superionic Solids And Solid Electrolytes Recent Trends*, (Eds A.L. Laskar, S. Chandra), Material Science Series, Academic Press, Inc 190 (1989).

28 F.M. Vichi, M.T. Colomer and M.A. Anderson, *Electrochem. and Solid State Letts,* **2**(7), 313 (1999).

29 S. Malhotra and R. Datta, *J. Electrochem. Soc.* **144,** L23 (1997).

30 P. Costamagna, C. Yang, A.B. Bocarsly and S. Srinivasan, *Electrochimica Acta.*, **47,** 1023 (2002).

31 M. Watanabe, H. Uchida, Y. Seki, M. Emori and P. Stonehart, *J. Electrochem. Soc.,* **143**(12), 3847 (1996).

32 M. Watanabe, H. Uchida, Y. Seki, M. Emori, *J. Phys. Chem. B.,* **102,** 3129 (1998).

33 H. Uchida, Y. Ueno, H. Hagihara and M. Watanabe, *J. Electrochem. Soc.,* **150**(1), A57 (2003).

34 C. Yang, P. Costamagna, S. Srinivasa, J. Benziger and A.B. Bocarsly, *J. Power Sources,* **103**, 1 (2001).

35 Y. Si, J.M. Fenton and H.R. Kunz, *Preparation of MEAs for PEM Fuel Cells Operating At Above 100*°C, 199th ECS, Washington DC 2001, March 25-29.

36 Y-I Park, J-D Kim and M. Nagai, *J. Mat. Sci. Letts.*, **19,** 1621 (2000).

37 M. A. Harmer and Q. Sun, *U.S. Patent 6,515,190*, (2003).

38 K.T. Adjemian, S.J. Lee, S. Srinivasan, J. Benziger and A.B. Bocarsly, *J. Electrochem. Soc.,* **149**(3), A256 (2002).

39 K.T. Adjemian, S. Srinivasan, J. Benziger and A.B. Bocarsly, *J. Power Sources ,* **109**, 356 (2002).

40 K.A. Mauritz, I.D. Stefanithis, S.V. Davis, R.W. Scheez, R. K. Pope, G.L. Wilkes and H –H Huang, *J. Appl. Polym. Sci.,* **55**, 181 (1995).

41 W.G. Grot and G. Rajendran, U.S. Patent # 5,919,583, 1999.

42 K. Kanamura, H. Morikawa and T. Umegaki, *J. Electrochem. Soc.*, **150**(2), A193 (2003).

43 T. Thampan, S. Malhotra, H. Tang and R. Datta, *J. Electrochem. Soc.*, **147**(1), 3242 (2000).

44 E.A. Mason and A.P. Malinauskas, *Gas Transport in Porous Media: The Dusty Gas Model,* p142, Elsevier Amsterdam (1983).

45 P. Choi and R. Datta, *in press J. Electrochem. Soc.* (2003).

46 F. Lonyi, J. Valyon, J. Engelhardt and F. Mizukami, *J. Catal.* **160**, 279 (1996).

47 M. Misono and T. Okuhara, *CHEMTECH*, **23**, (Nov 1993) & M. Misono, T. Okuhara and N. Mizuno, *Succesful Design of Catalysts*, Ed. T Inui, p267 Elsevier, Amsterdam (1988).

48 G. A. Olah, G. K. Surya Prakash and J. Sommer, *Superacids*, Wiley, New York (1985).

49 K. Arata, *Applied Catalysis A: General,* **146**, 3 (1996).

50 R.B. Moore and C.R. Martin, *Anal Chem*, **58**, 2570 (1986).

51 W. Apichatachutapan, R.B. Moore and K.A. Mauritz, *J. Appl. Polym. Sci.,* **62**, 417 (1996).

---

52 P. Liu, J. Bandara, Y. Lin, D. Elgin, L. F. Allard, Ya-P. Sun, *Langmuir* **18(26)**, 10398 (2002).

53 J. Brinker and G. Scherer, *Sol-Gel Science*, Academic Press, New York, 42 (1989).

54 J.E. Resoke and M.A. Barteu, *J. Phys. Chem. B*, **101,** 1113 (1997).

55 E. Busenberg and C.V. Clemency, *Clays and Clay Materials,* **21**, 213 (1973).

56 B. Bahar, C. Cavalca, S. Cleghorn, J. Kolde, D. Lane, M. Murthy, G. Rusch, *J. New Mater. Electrochem. Syst.*, **2(3)**, 179 (1999).

57 T.J. Schmidt, H.A. Gasteiger, G.D. Stäb, P.M. Urban, D.M. Kolb and R.J. Behm, *J. Electrochem. Soc.*, **145**(7), 2534 (1998).

58 N. Miyake, J.S. Wainright and R.F. Savinell, *J. Electrochem. Soc.*, **148**(8), A898 (2003).

59 T. Thampan, S. Malhotra, J. Zhang and R. Datta, *Catalysis Today*, **67**, 15 (2001).

60 S.J. Lee, S. Mukerjee, E.A. Ticianelli, and J. McBreen, *Electrochimica Acta* **44**, 3283 (1999).

V. CONCLUSIONS AND RECOMMENDATIONS

Introduction

The research has led to number of important developments that will significantly contribute to the scientific body of knowledge in higher temperature PEMs for fuel cell applications. These are:

i. Synthesis and evaluation of composite PEMs, and

ii. Design and simulation of higher temperature PEMFCs.

Synthesis and Evaluation of Composite PEMs

Promising composite PEMs that show increased water uptake and conductivity at higher temperature and lower RH have been developed. Among the various candidates investigated, the ZrO_2 composites prepared by the sol-gel method demonstrate the most promising enhancements in water uptake and conductivity.

However, the expected improved MEA performance is yet to be observed in fuel cell testing. Thus, it is recommended to continue to further develop and analyze the composite PEMs in an attempt to improve fuel cell performance at higher temperature/lower RH.

Characterization and Analysis of composite PEMs

In this work, the composites were characterized water uptake, conductivity, IEC and MEA performance. The Nafion ZrO_2 sol-gel PEMs remain to be characterized by ash analysis (preliminary ash analysis[1] indicate an additive loading of 3~4 wt. %), glass transition point (T_g) determination (preliminary measurements indicate a T_g of $120^{\circ}C$ ~$130^{\circ}C$) and Young's modulus measurement. Additionally the composite PEMs must be characterized to measure the additive particle size. Mechanical testing of the composite PEMs must also be undertaken, as it is known that an optimum oxide loading exits[2]. It should also be noted that a portion of the conductivity measurements were done in the X-Y plane as is conventionally done, it is important to test the PEMs in the Z-plane as that is the direction of proton transport in the MEA orientation. If the composite membranes are anisotropic, different values of conductivity would result.

Since the composite PEMs prepared by the sol-gel method demonstrate the highest conductivity, it is reasonable to focus future efforts utilizing this procedure.

The synthesis goal is a composite PEM with nano-structured ZrO_2 distributed homogenously through the PEM. It is, therefore, useful to examine the chemistry of the sol-gel synthesis of metallic oxides.

Sol-Gel Synthesis of Metallic Oxides

Sol-gel technology provides a relatively simply way to produce polymeric metallic oxides or ceramics via the hydrolysis and condensation of suitable metallic oxides[3]. It is also known from reported work on the deposition of metallic oxides in Nafion® for the photo-catalytic production of H_2[4], that the host PEM serves as a template that directs the morphology of the precipitated oxide in the PEM matrix[5].

The hydrolysis reaction (Eq. 1.) and the subsequent condensation reactions (Eqs. 2, 3) are shown below,

$$\text{M-(OR)}_n + m\,\text{H}_2\text{O} \rightarrow \text{M-(OR)}_{n-m}(\text{OH})_m + m\,\text{ROH} \qquad (\mathbf{1})$$

$$\sim\text{M-OH} + \text{HO-M}\sim \rightarrow \sim\text{M-O-M}\sim + \text{H}_2\text{O} \qquad (\mathbf{2})$$

$$\sim\text{M-OR} + \text{HO-M}\sim \rightarrow \sim\text{M-O-M}\sim + \text{ROH} \qquad (\mathbf{3})$$

where M-(OR)_n denotes a metallic alkoxide. An acid catalyst is included to protonate the alkoxide to produce a good leaving group.

As a first step, an alcohol is utilized to swell the PEM to facilitate the alkoxide penetration into the interior of the PEM, ensuring the oxide is not limited to the PEM subsurface. It is assumed that the alkoxide solution then occupies the alcohol clusters formed within the membrane. These clusters with the surrounding PTFE backbone serve as a template to direct the morphology and constrain the oxides formed to the nano-particle range.

The transition metals (Zr and Ti) exhibit high chemical reactivity due to their low electro-negativity and ability to form several coordination states. Thus, condensation and hydrolysis occur spontaneously upon reaction with water[3].

The modification of synthesis procedures may also result in higher conductivity. The synthesis parameters include[3]:

1. Alkoxide/H_2O ratio. A low water content will limit the condensation reaction[3].
2. Polarity and pH of the solvent. The degree of PEM swelling constrains the oxide formation.
3. Alkoxide type. Precursor alkoxide was observed to have only a small impact on the composite properties[5].
4. Temperature of the reaction. The sol-gel reactions will occur more rapidly at higher temperatures[3].
5. Concentration of alkoxide. The alkoxide concentration an dthe degree of pre-swelling can control the additive loading[5].

The sol-gel modified PEMs were fabricated by imbibing the alkoxide/solvent into a preformed PEM. Alternatively it maybe fabricated by precipitating the oxide in the PEM as it is being cast, which offers another method for isotropic particle distribution.

Figures V-1 and V-2 demonstrate the effects of alkoxide concentration and different solvent on PEM conductivity. It is observed that the solvent and alkoxide concentration can significantly enhance the PEM conductivity, and future work may include the synthesis parameters and their effects on conductivity.

Additionally, the polymer electrolyte used as the base membrane can be modified. Thin PEMs are available, such as the Gore-Select® membrane, a Teflon reinforced Nafion® membrane with a thickness of 25 μm. Coupled with the additive, this thinner should be investigated.

Similarly lower EW PEMs with less mechanical stability but higher acid concentration are available. Since inclusion of particles seems to improve the thermo-mechanical stability of PEMs, these membranes should be investigated.

The presence of a PTFE backbone in Nafion® provides the mechanical integrity albeit at the cost of lower water sorption. If the backbone of a PEM were modified in structure or hydrophilicity, this PEM combined with the additives would have even higher conductivity than the modified composites in this study.

Finally, after the development of a suitable conductivity enhanced PEM, the corresponding PEM gel must be incorporated into the catalyst layer to allow the benefits of the improved PEM to translate into a high performing fuel cell.

Thus, there are a number of future directions that should be pursued to eventually result in a higher temperature, lower RH PEMs with high conductivity.

Design and Simulation of Higher Temperature PEMs

Based on the modeling, useful insights into the design of the composite PEM has been gained. Utilizing the PEM transport model, a rational design of the higher temperature composites was initiated.

The development of the composite PEMs provides an opportunity to further extend the model in an attempt to simulate the water uptake and conductivity of the composites and differing EW PEMs. Figure V-3 shows the model-based simulation of increased water and increased acidity effects on PEM conductivity. It appears from these that the increase of water sorption is more important than an increase in acidity. In reality, of course, these two parameters are inextricable linked. A higher acidity PEM is also more hydrophilic. These simulations should be extended and experimentally validated.

Furthermore a fuel cell model was developed that captured the controlling overpotential losses. This model is useful for design insights and for optimizing the operating conditions for higher temperature PEM fuel cells.

However, it is important to further develop and test the sensitivity and accuracy of the model to ensure its robustness. Figures V-4 toV-11 experimentally show the effect of air and oxygen pressure at 70°C and 90°C, on Nafion 115 and Nafion 112 MEAs.

This data set provides an experimental database against which to develop and test a next generation fuel cell model. Although it is a challenging endeavor, the final result would be a predictive model with a minimum number of fitted parameters that not only provides design insights, but can also be utilized as a diagnostic tool in analyzing fuel cell performance.

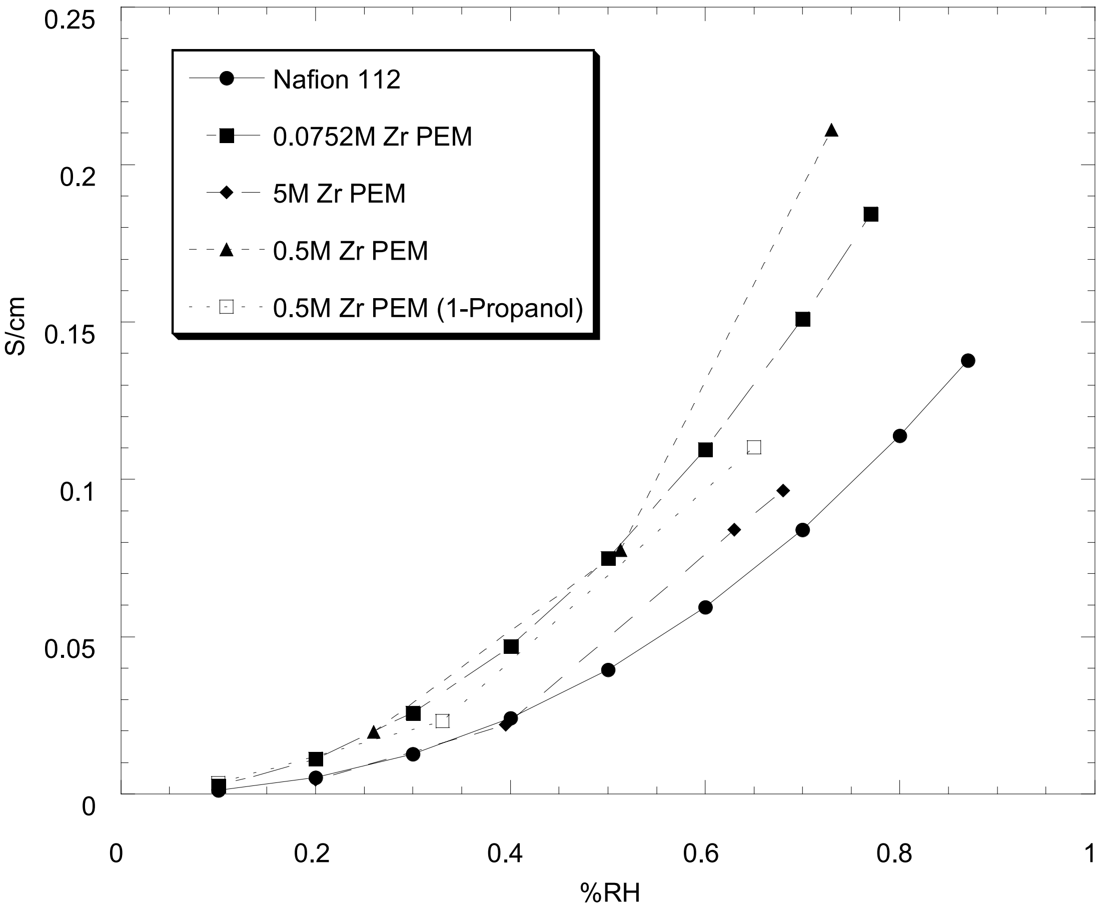

Figure V-1 The effects of alkoxide concentration and solvent on the conductivity of the composite PEMs at 90°C. Except where noted, the solvent utilized was 2-propanol.

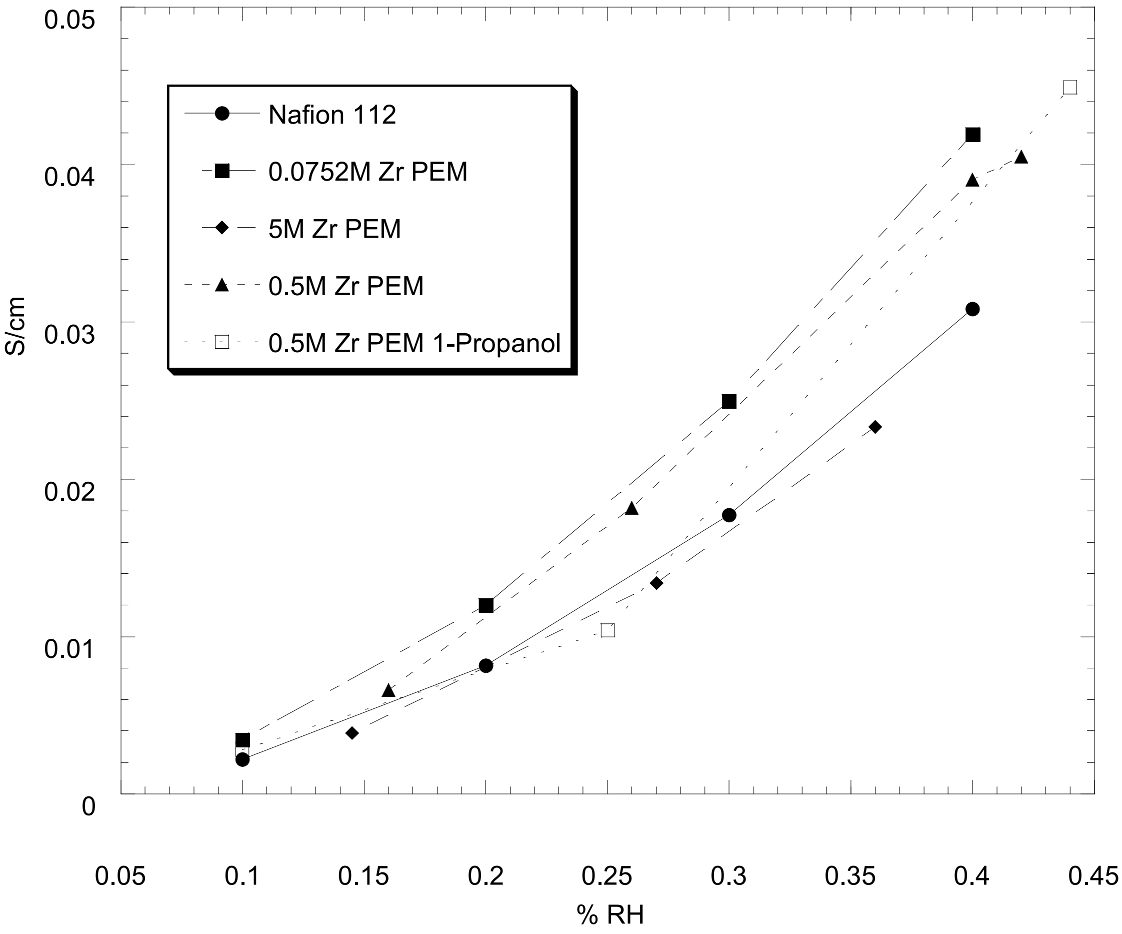

Figure V-2 The effects of alkoxide concentration and solvent on the conductivity of the composite PEMs at 120°C. Except where noted, the solvent utilized was 2-propanol.

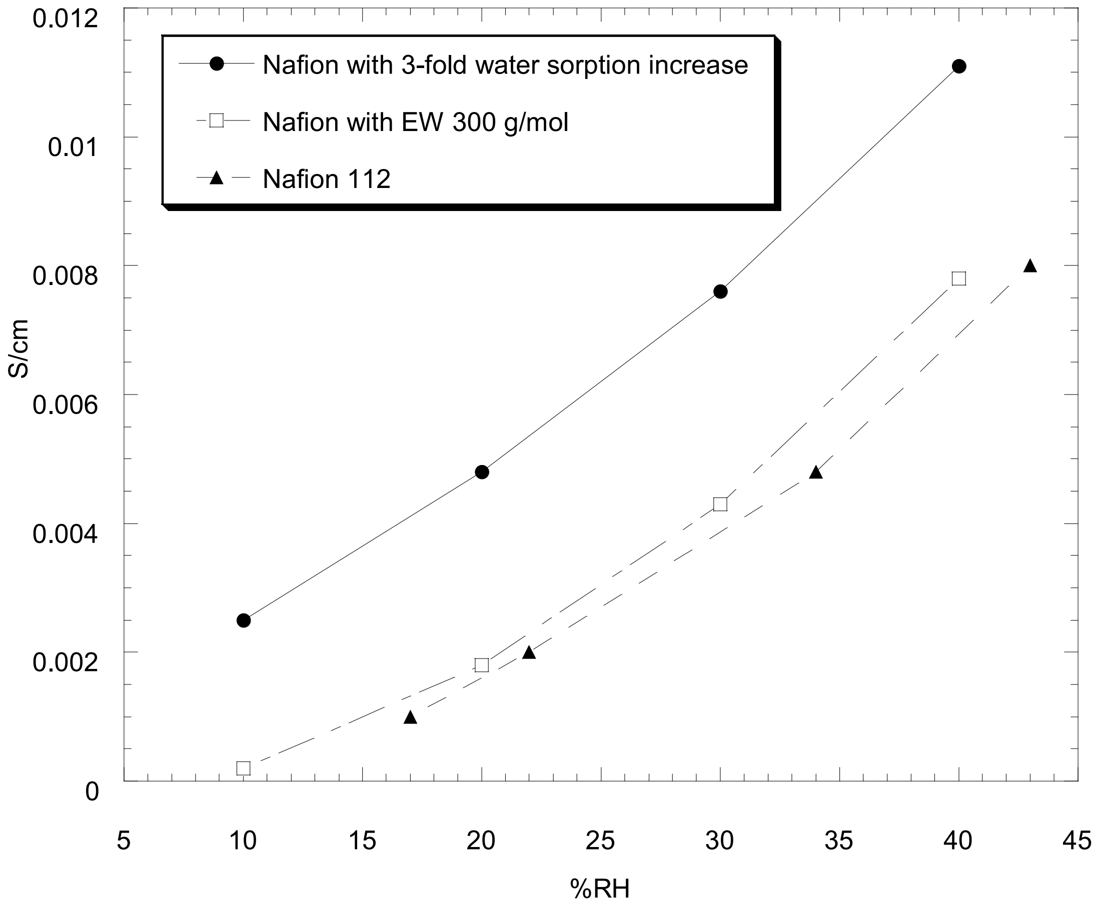

Figure V-3 Model-based simulation of the effects of increased water sorption and increased acidity on PEM conductivity. The water sorption was increased by a factor of 3, while the acidity was increased from 1100 EW to 300 EW. PEMs with similar properties to the simulations exist but do not show the mechanical integrity of Nafion 1100 EW series.

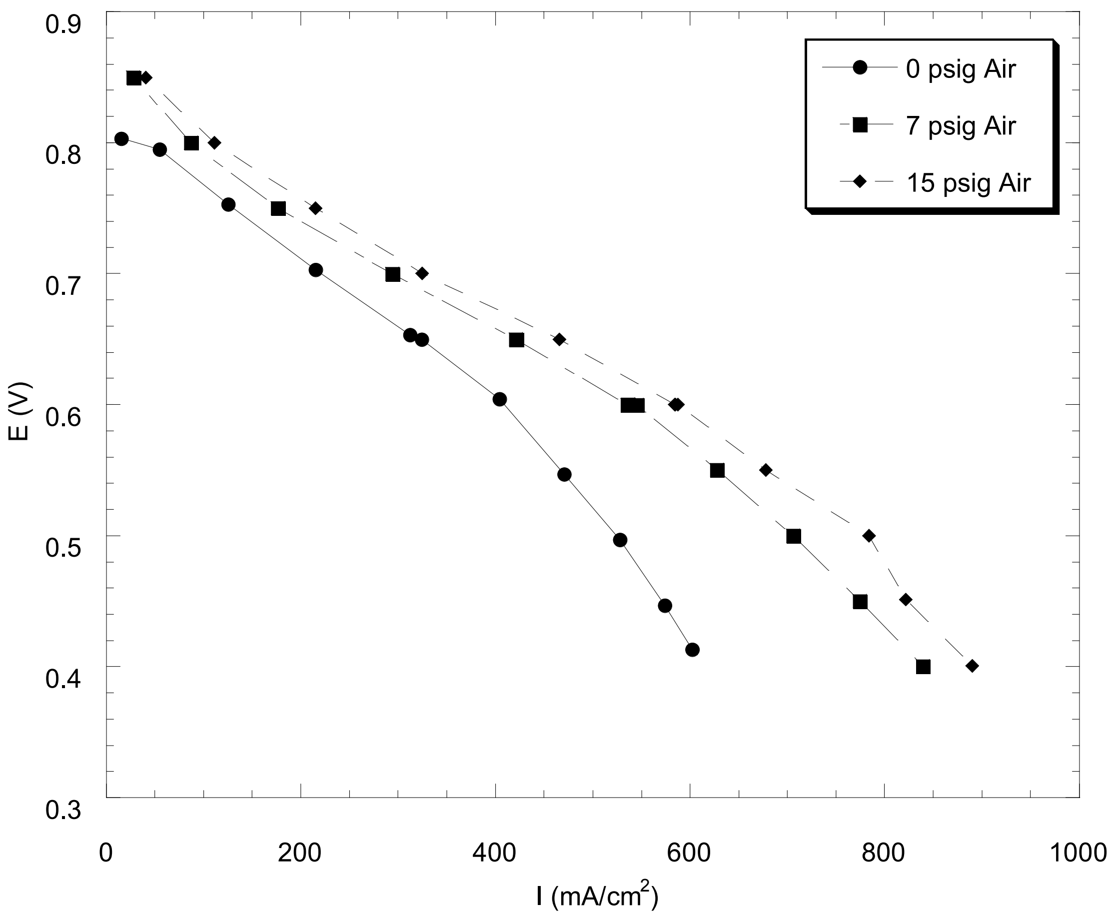

Figure V-4 Nafion 115 experimental results. Current density (A/cm^2) versus voltage (V) plot for a 5 cm^2 fuel cell operated at 70°C with a H_2/Air feed; humidifier temperatures of 80°C and 80°C for anode and cathode, respectively; E-TEK single-sided electrodes with platinum catalyst ($\omega_M = 0.2$ Pt on Vulcan XC-72) loading $m_M = 0.4$ mg Pt/cm^2 and Nafion® loading $m_I = 0.7$ mg/cm^2, and with a Nafion® 115 membrane.

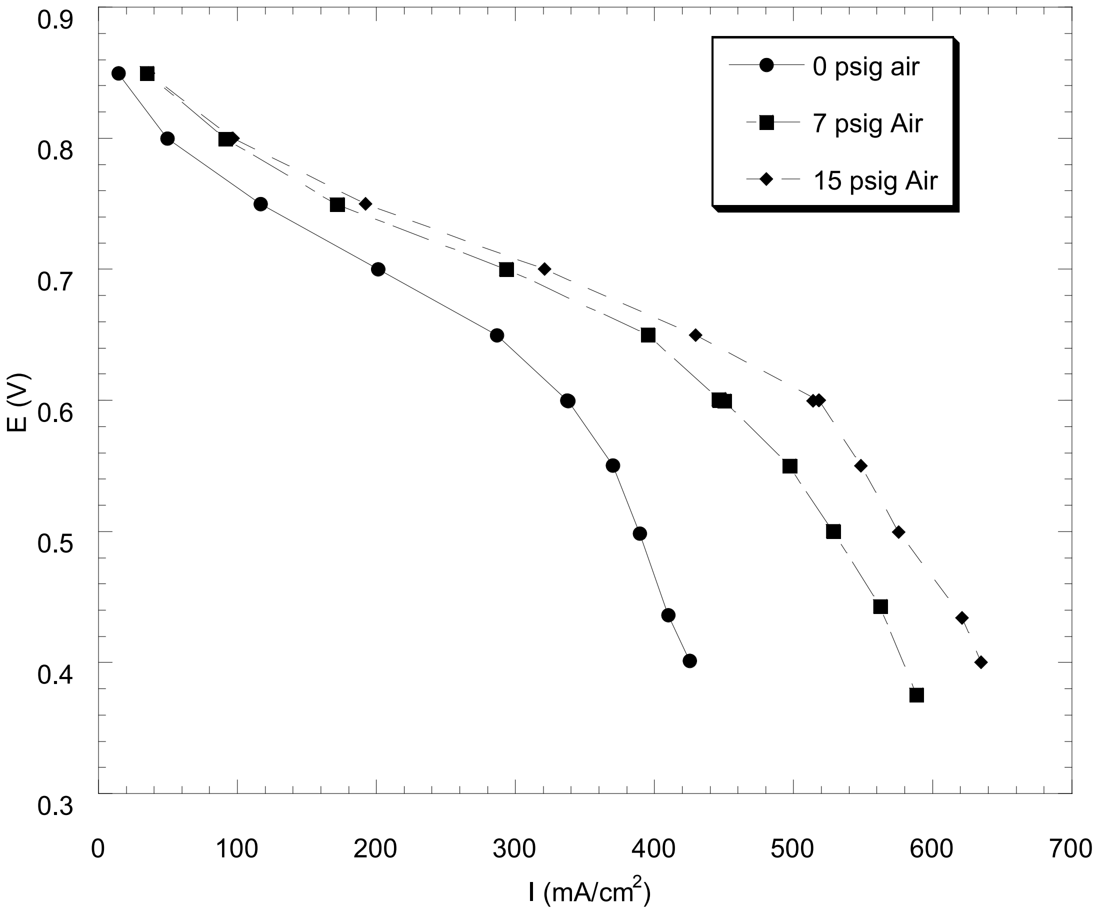

Figure V-5 Nafion 115 experimental results. Current density (A/cm^2) versus voltage (V) plot for a 5 cm^2 fuel cell operated at 90°C with a H_2/Air feed; humidifier temperatures of 90°C and 90°C for anode and cathode, respectively; E-TEK single-sided electrodes with platinum catalyst (ω_M = 0.2 Pt on Vulcan XC-72) loading m_M = 0.4 mg Pt/cm^2 and Nafion® loading m_I = 0.7 mg/cm^2, and with a Nafion® 115 membrane.

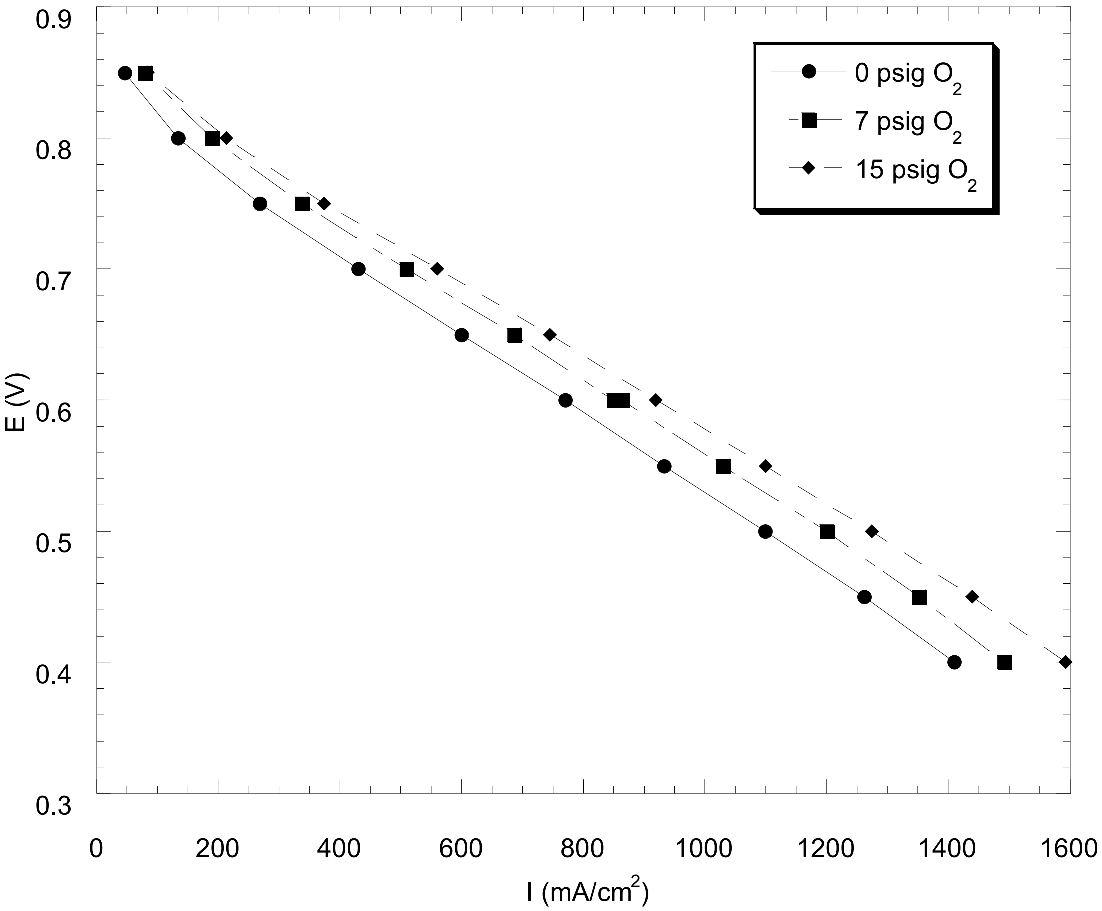

Figure V-6 Nafion 115 experimental results. Current density (A/cm^2) versus voltage (V) plot for a 5 cm^2 fuel cell operated at 70°C with a H_2/O_2 feed; humidifier temperatures of 80°C and 80°C for anode and cathode, respectively; E-TEK single-sided electrodes with platinum catalyst (ω_M = 0.2 Pt on Vulcan XC-72) loading m_M = 0.4 mg Pt/cm^2 and Nafion® loading m_I = 0.7 mg/cm^2, and with a Nafion® 115 membrane.

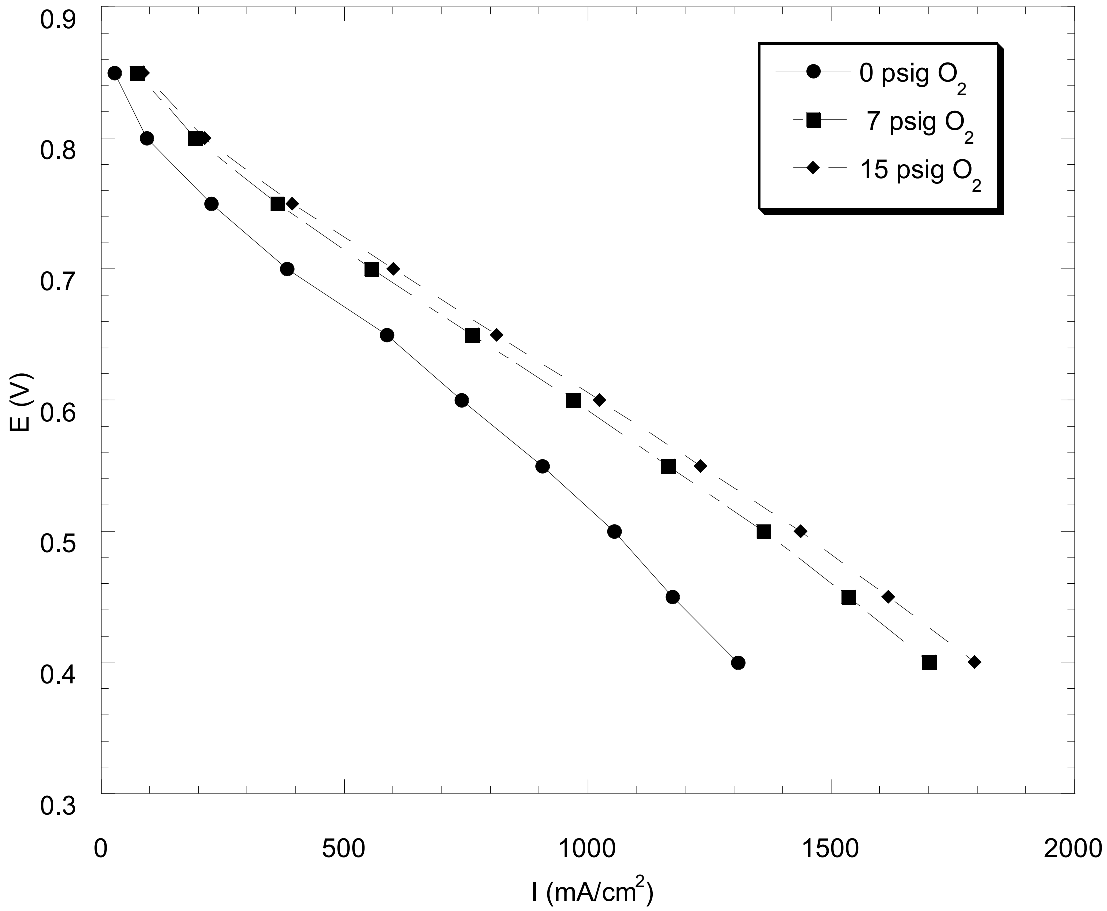

Figure V-7 Nafion 115 experimental results. Current density (A/cm^2) versus voltage (V) plot for a 5 cm^2 fuel cell operated at 90°C with a H_2/O_2 feed; humidifier temperatures of 90°C and 90°C for anode and cathode, respectively; E-TEK single-sided electrodes with platinum catalyst (ω_M = 0.2 Pt on Vulcan XC-72) loading m_M = 0.4 mg Pt/cm^2 and Nafion® loading m_I = 0.7 mg/cm^2, and with a Nafion® 115 membrane.

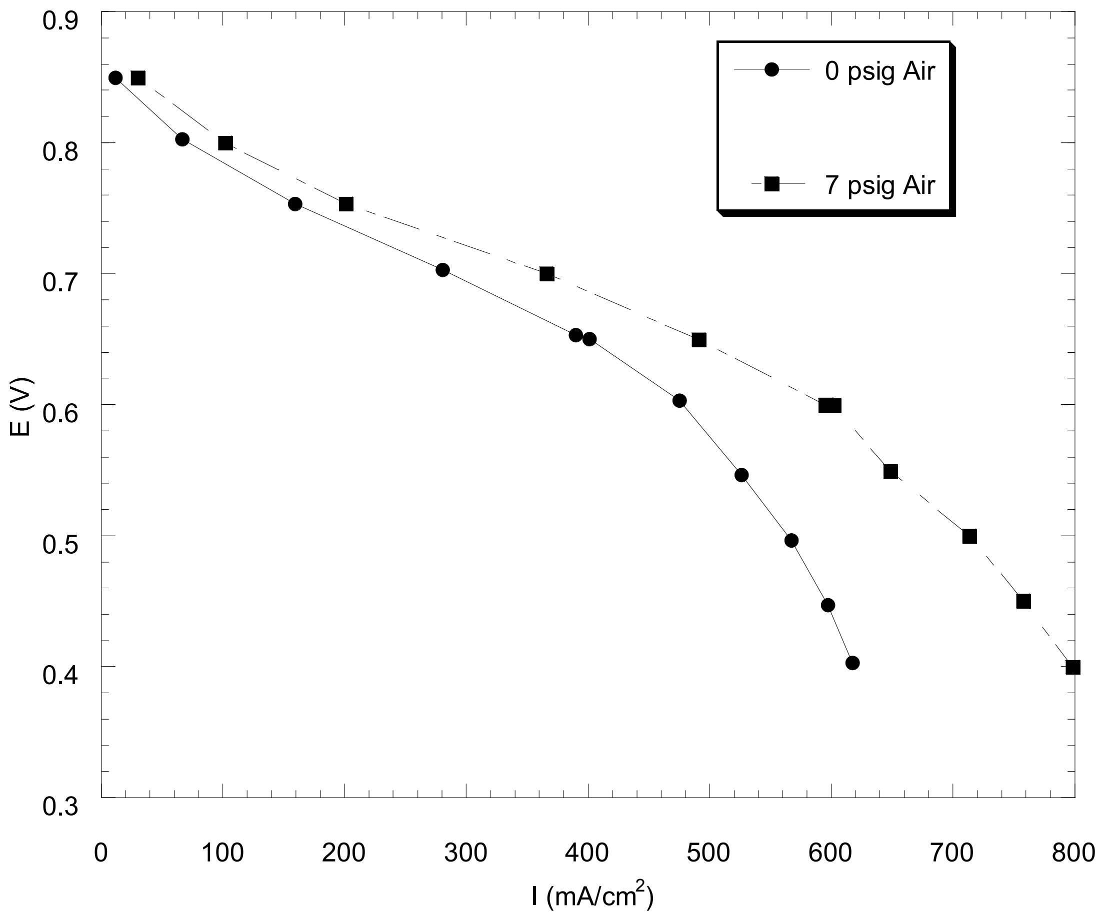

Figure V-8 Nafion 112 experimental results. Current density (A/cm^2) versus voltage (V) plot for a 5 cm^2 fuel cell operated at 70°C with a H_2/Air feed; humidifier temperatures of 80°C and 80°C for anode and cathode, respectively; E-TEK single-sided electrodes with platinum catalyst (ω_M = 0.2 Pt on Vulcan XC-72) loading m_M = 0.4 mg Pt/cm^2 and Nafion® loading m_I = 0.7 mg/cm^2, and with a Nafion® 112 membrane.

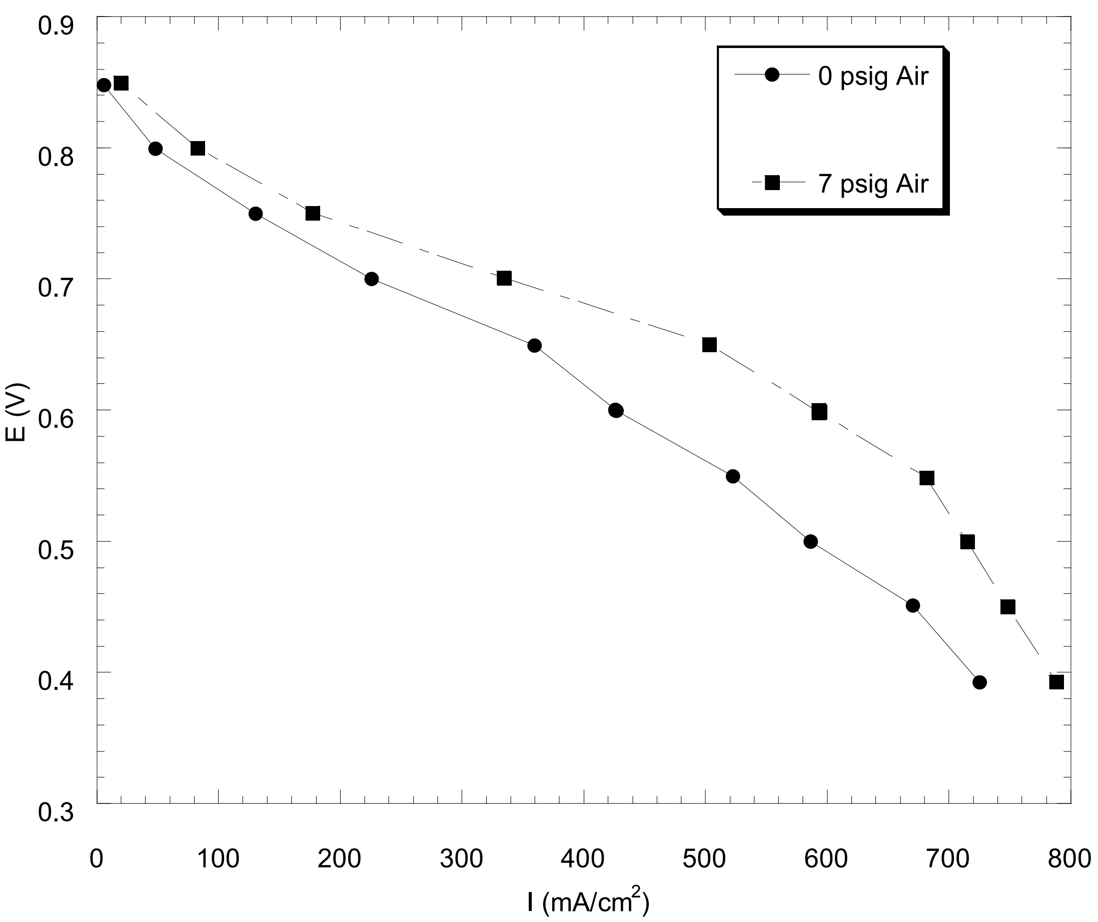

Figure V-9 Nafion 112 experimental results. Current density (A/cm^2) versus voltage (V) plot for a 5 cm^2 fuel cell operated at 90°C with a H_2/Air feed; humidifier temperatures of 90°C and 90°C for anode and cathode, respectively; E-TEK single-sided electrodes with platinum catalyst (ω_M = 0.2 Pt on Vulcan XC-72) loading m_M = 0.4 mg Pt/cm^2 and Nafion® loading m_I = 0.7 mg/cm^2, and with a Nafion® 112 membrane.

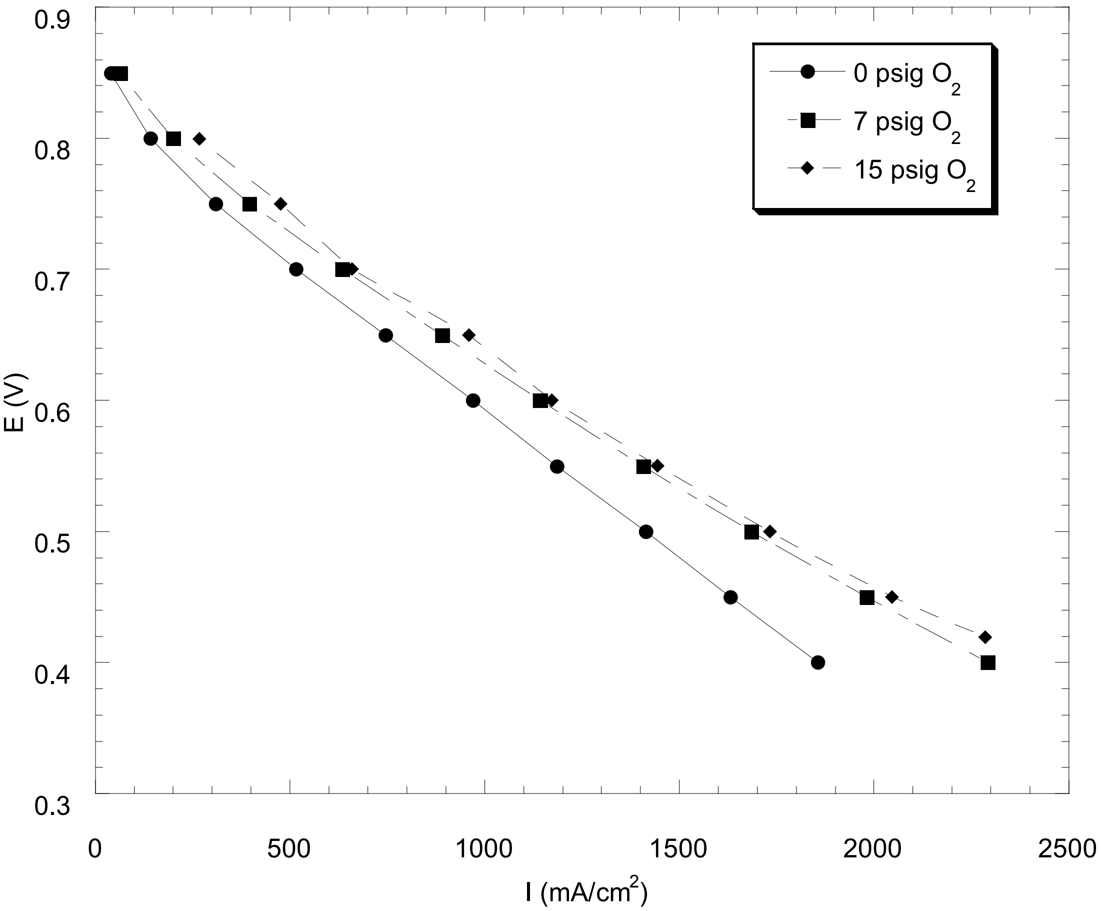

Figure V-10 Nafion 112 experimental results. Current density (A/cm^2) versus voltage (V) plot for a 5 cm^2 fuel cell operated at 70°C with a H_2/O_2 feed; humidifier temperatures of 80°C and 80°C for anode and cathode, respectively; E-TEK single-sided electrodes with platinum catalyst (ω_M = 0.2 Pt on Vulcan XC-72) loading m_M = 0.4 mg Pt/cm^2 and Nafion® loading m_I = 0.7 mg/cm^2, and with a Nafion® 112 membrane.

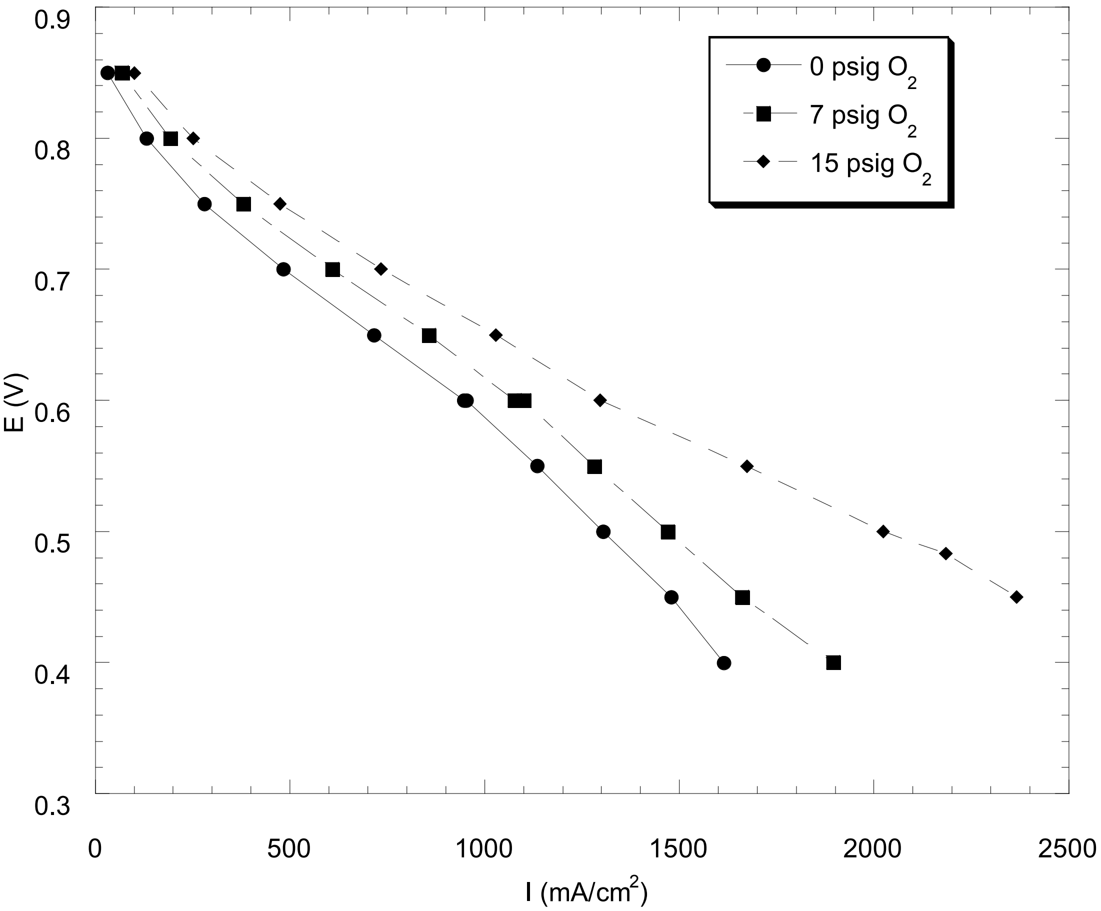

Figure V-11 Nafion 112 experimental results. Current density (A/cm^2) versus voltage (V) plot for a 5 cm^2 fuel cell operated at 90°C with a H_2/O_2 feed; humidifier temperatures of 90°C and 90°C for anode and cathode, respectively; E-TEK single-sided electrodes with platinum catalyst (ω_M = 0.2 Pt on Vulcan XC-72) loading m_M = 0.4 mg Pt/cm^2 and Nafion® loading m_I = 0.7 mg/cm^2, and with a Nafion® 112 membrane.

References

1 Private communication with S. Enache, *W.L. Gore & Assoc., Inc*.

2 K. A. Mauritz, Materials Science and Engineering C, **6** (1998) 121.

3 J. Brinker and G. Scherer, *Sol-Gel Science*, Academic Press, New York, 1989.

4 H. W. Rollins, F. Lin, J. Johnsonson, J. Ma, J. Liu, M. Tu, D. D. DesMarteau and Y, Sun, *Langmuir*, **16** 2000, 8031.

5 Ping Liu, J. Bandra, Y Lin, D. Elgin, L.F. Allard and Y. Sun, *In Press*.